UNIVERSITY OF EXETER

DOCTORAL THESIS

Light in scattering media: active control and the exploration of intensity correlations

---

Author:

Alba M. PANIAGUA-DIAZ

Supervisors:

Prof. William L. BARNES

Dr. Jacopo BERTOLOTTI

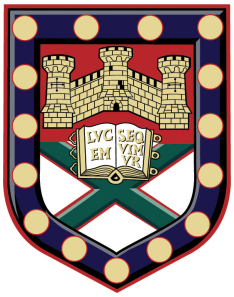

A thesis submitted in fulfilment of the requirements
for the degree of Doctor of Philosophy
in March 2018

Signed:

Light in scattering media: active control and the exploration of intensity correlations

Submitted by Alba Maria Paniagua Diaz to the University of Exeter as a thesis for the degree of Doctor of Philosophy in Physics in March 2018

I certify that all material in this thesis which is not my own work has been identified and that no material has previously been submitted and approved for the award of a degree by this or any other University.

All data created during this research is available from the University of Exeter's institutional repository at https://doi.org/10.24378/exe.443. The point of contact for any queries on the thesis/data and relevant code/software is Dr. Jacopo Bertolotti, email address: j.bertolotti@exeter.ac.uk.

“*Caminante no hay camino, se hace camino al andar*”...

“Wayfarer there is no path, the path is done when walking”...

Antonio Machado - Spanish poet

UNIVERSITY OF EXETER

Abstract

Physics and Astronomy
College of Engineering, Mathematics and Physical Sciences

Doctor of Philosophy

Light in scattering media: active control and the exploration of intensity correlations

by Alba M. PANIAGUA-DIAZ

When light encounters scattering materials such as biological tissue, white paint or clouds, it gets randomly scattered in all directions, which traditionally has been seen as a barrier for imaging techniques (reducing their resolution) or sensing, due to the reduction of the penetration depth of light. However, in recent years it has been shown that scattering might not necessarily be an impediment, and that the knowledge of the properties of multiple scattering can be indeed useful for imaging, sensing and other applications.

In the first part of this thesis (Chapters 2 to 5) we study the implications of manipulating the light incident on a multiply scattering material. We experimentally show how by actively controlling the output light of a bad quality laser we manage to not only improve its beam quality, but also in an energy-efficient way, in comparison with traditional methods. In a different experiment presented in this thesis, we show how the active control of the light incident on a scattering material can be useful to improve sensing through scattering media, by means of increasing the transmission and energy deposited inside (Chapter 5).

In the final part of the thesis we present the first experimental observation of intensity correlations between transmitted and reflected patterns from a scattering material (Chapter 6), exploring how it depends on the parameters of the scattering medium. In the last part of the thesis (Chapter 7) we present a new imaging technique based on the use of the intensity correlations described in the previous chapter, opening new possibilities to non-invasive imaging through highly scattering materials.

Contents

To my partner, my parents and my brother

Introduction

Understanding the nature of light has been a matter of study for centuries. The first written attempt to explain the nature of light and human vision is due to the Greek philosopher Euclid (*c.*300 BC).[1] In *Optica* Euclid postulated that light travelled in straight lines, describing mathematically the laws of reflection and refraction. Although they originally thought light rays were originated from the eyes and to subsequently reach the objects, that geometrical approach is equally valid to explain how light travels from the objects to our eyes.[2,3] Geometrical optics has been successfully employed during the last centuries as an extremely useful tool to control light or to design imaging elements, among other applications.[4,5]

However, even though geometrical optics can easily explain how light propagates in an homogeneous medium, e.g. in air or in a tank of water, explaining how light propagates through highly inhomogeneous media, e.g. clouds or fog, becomes very challenging, although such media are just small drops of water in air. This is because when light encounters such small drops of different refractive index, it is scattered in different directions and multiple times, which makes ray tracing very hard to implement. This lack of directionality prevents light from reaching far distances on a foggy day, and scrambles the light before it reaches our eyes. This is the same phenomenon that occurs when light travels through biological tissue, clouds or most white substances.

FIGURE 1: Picture of my dad in a field of olive trees where the fog blurs the more distant details.

Light scattering has been considered as an impediment for many years, degrading the resolution of imaging techniques and limiting light penetration in scattering media.[6–9] However multiple

scattering is not as random as it seems and it was shown that it is possible to take advantage of its deterministic nature to, for instance, obtain a diffraction limited image behind a completely opaque layer[10,11] by means of the optical memory effect.[12] However, despite the importance of this breakthrough, the optical memory effect needs the scattering material to be thin and at a distance apart from the object to image, which limits the potential applications of the technique.

Another milestone in exploiting the properties of scattering media is based on the control of light propagation through such media. The group of Mathias Fink[13] was the first to show the possibility to manipulate a scattered acoustic wave and focus it back to the source point, by making use of the time-reversal invariance. It was not until 2007 that light control through scattering media was demonstrated by Vellekoop and Mosk,[14] focusing light through an opaque scattering material.This was initially achieved by modifying the phase of the wavefront of the beam in different regions, using a liquid crystal spatial light modulator. Shortly after that, different applications of wavefront control were developed, showing different possibilities of focusing light through scattering materials,[15,16] imaging improvement,[17–22] spectral control of broadband light,[23] or cryptography[24,25] among others.

In addition to these applications, it was shown that wavefront shaping techniques are also capable improving one of the major limitations of light in scattering media: reduced penetration depth. As I discuss in more detail in Chapter 1, wavefront shaping is capable of substantially change the amount of light that is being transmitted or reflected by the scattering material.[26–28] This property is of particular importance for optical sensing in biomedical applications, which are limited to work near the illumination surface due to the attenuation of the multiple scattering in biological tissue.[9] However the potential of wavefront shaping to increase the penetration depth in this field has not been completely explored, only for weakly scattering materials.[17]

Despite the usefulness of wavefront shaping for light control in scattering media, in order to properly design the wavefront it is necessary to have access to both sides of the material, either to characterize the transmission or reflection matrix or to use a guide-star or feedback element for the design of the wavefront. This limits the applications of wavefront shaping to systems in which generally both sides of the material are accessible.

Aim and outline of this thesis

The work presented in this thesis addresses the current challenges of light in scattering media from two perspectives: applications of active wavefront control (Chapters 2 to 5) and intensity correlations in scattering media (Chapters 6 to 7). In the first part of the thesis we revisit and partially extend the theory of optical wavefront control, to fully cover the experimental situations detailed in Chapters 4 and 5. One of the experiments on wavefront control addresses the problem

of poor beam quality at the output of optical fibers, and the second and main experiment is based on increasing of the penetration depth for optical sensing in medical applications.

In the second part we present the first experimental observation of intensity correlations between the reflected and transmitted intensity patterns produced by a scattering medium. The existence of these correlations not only open new possibilities to imaging through strongly scattering media as we show in Chapter 7, but open new possibilities for non-invasive wavefront control.

The structure of the thesis is:

In Chapter 1 we present the framework of multiple scattering of light and the theory used to describe light propagation. We show the usefulness of diffusion theory to describe the propagation of average intensity through scattering media, when the wavefront has not been modified. We present the scattering matrix formalism to study the fields that propagate through complex media, and how this knowledge can be used to modify the wavefront to a desired output. In the final part we present Random Matrix Theory and the Uncorrelated Transmission Coefficients model, highlighting their importance in estimating the transmission through a scattering material, very useful to implement wavefront shaping.

In Chapter 2 we introduce optical wavefront control and all the elements needed to understand the wavefront optimization process, such as wavefront modulators, feedback components or the algorithm used. Given that we use a Digital Micromirror Device in the experiments described in Chapters 4 and 5, we make particular emphasis on how the wavefront can be modulated both in amplitude and phase using these devices.

In Chapter 3 we present the concept of ideal wavefront control, and the effects of imperfect wavefront modulation. We detail the processes of focusing light through a scattering medium, and increasing the total transmitted light through it. In this chapter we also introduce the details about focusing and maximal transmission enhancements such as the maximal expectations under experimental situations as well as the statistical distribution of the optimal enhancements.

In Chapter 4 we investigate and extend the theory of wavefront control, so far well studied for plane wave manipulation. We explore the consequences of manipulating a speckle pattern as illumination beam. In addition we present an experiment in which we manipulate a speckled beam coming out of a multimode fiber and convert it to a diffraction limited Gaussian spot, showing very good agreement between theory and experimental results.

In Chapter 5 we present an experiment in which we increase the generated Raman signal of an element embedded inside a scattering medium by almost 50%. This is achieved by increasing the total transmitted light through the medium, using wavefront shaping techniques. We show that the increase in total transmission through the medium is linear with the increase of the Raman signal from inner depths. In addition, we study the energy distribution inside the sample assuming

ideal wavefront control, and total transmission through the sample, and how that would affect the collection of Raman signal from different depths.

In Chapter 6 we introduce the intensity correlations between reflected and transmitted speckle patterns, for scattering media of different thicknesses and mean free paths. We first introduce the well studied speckle correlations in transmission to then present the terms that contribute in the reflection-transmission configuration. We present the first experimental observation of such correlations and study the properties and features of the correlation in different scattering regimes.

In Chapter 7 we present a new imaging technique: Blind Ghost Imaging, that exploits the correlations between reflected and transmitted speckle patterns described in the previous chapter. Given that this imaging approach is based on Ghost Imaging Techniques, we first introduce these techniques and then present our approach, showing the main differences between the two and the potential of this new approach.

Chapter 1

Light propagation in scattering media

1.1 Light scattering and diffusion of light

When a beam of light impinges onto a scattering material two fundamental things can happen: light passes through without being scattered by the medium, or it encounters an inhomogeneity and it is scattered by it. The light that is not scattered by the medium is called ballistic light. The more inhomogeneities that are present in the medium, the more likely it is that light interact with it, and therefore less ballistic light will come out, as one might expect. A good estimate for the ballistic light leaving the scattering medium is given by the Lambert-Beer law.[29,30] When there is a defined direction of propagation, e.g. the beam of light propagates along the z direction, assuming an absorption-free medium[†], the Lambert-Beer law reads:

$$I(z) = I_0 e^{-z/\ell_s}, \tag{1.1}$$

where I_0 is the incident intensity in the medium and ℓ_s the scattering mean free path of the sample. The scattering mean free path is defined as the average distance the beam travels before it suffers a scattering event.[29–31] At the macroscopic scale, the scattering mean free path ℓ_s is the distance at which the incident intensity is reduced by a factor $1/e \approx 37\%$.[32]

The scattering mean free path represents also the average distance after which the incident beam is randomized, assuming the scattering is isotropic. When the scattering is not isotropic, meaning that the scattered waves have a preferred direction of scattering, the distance needed to randomize the beam is different and it is given by the transport mean free path ℓ_t:

$$\ell_t = \frac{\ell_s}{1 - \langle cos(\theta) \rangle}, \tag{1.2}$$

[†]In this thesis we consider all the scattering media to be absorption-free (as in our experiments to a very good approximation), which means that the only attenuation of light comes from scattering. If absorption was present, in eq. 1.1 the intensity would decay as $e^{-z/(\ell_s+\ell_a)}$ with ℓ_a the absorption mean free path.

where θ is the angle between the incident beam and the scattered one, and the brackets $\langle ... \rangle$ indicate averaging over the angles θ, taking into account the dependence of the scattering cross section σ with the angle, i.e. $\langle cos(\theta) \rangle = \int_0^{2\pi} \sigma(\theta) cos(\theta) d\theta$. Biological tissues are a good example of anisotropic scattering media, resulting in $\langle cos(\theta) \rangle$ between 0.7 - 0.95 in the optical regime.[32–34] For isotropic scattering $\langle cos(\theta) \rangle = 0$ and consequently $\ell_t = \ell_s$.

Knowing the distance at which the beam starts to get randomized (ℓ_t) and the total distance travelled (L), that allows us to classify the system into three different scattering regimes: quasi-ballistic, moderate scattering and diffusive regime. In the quasi-ballistic regime $\ell_t > L$, therefore the randomization of the beam is very small, given that the average distance for being randomized (ℓ_t) is larger than the distance travelled (L). In the moderate scattering regime $\ell_t \sim L$, therefore there will be a non-negligible fraction of light that will be randomized after propagation. In the diffusive regime $\ell_t \ll L$ and consequently most of the light will be randomized. Most of the work presented in this thesis is done in the diffusive regime, so the main part of this section is focused on establishing the background knowledge about diffusion.

In the diffusive regime, light is scattered multiple times in random directions before leaving the medium[§]. By averaging the effect of interference, the propagation of the average intensity follows a diffusion process and can therefore be well described by diffusion theory.[29,30,35,36] The diffusion equation of the averaged intensity reads:

$$\frac{\partial I(\vec{r},t)}{\partial t} = D\nabla^2 I(\vec{r},t) + S(\vec{r},t), \tag{1.3}$$

where $\vec{r}$ are the spatial coordinates, t is the time, D the diffusion coefficient and $S(\vec{r},t)$ the intensity source dependent on space and time. The solution to the diffusion equation depends on the geometry of the medium (providing the boundary conditions) and gives us the intensity distribution inside the medium in space and time. In our experiments we use the slab geometry (Fig. 1.1a), where the only variation in intensity we are interested in is along one dimension, z[‡]. When the system is in the steady state, the diffusion equation simplifies to:

$$D\nabla^2 I(z) + S(z) = 0, \tag{1.4}$$

where $S(z)$ is the steady state intensity source. There are generally two sources used in the literature: a simplified point source, so $S(z) = I_0\delta(z - z_{inj})$ that would represent very well the diffusion process originated at the position z_{inj} (such as an excited fluorophore inside a medium) and a decaying exponential source $S(z) = I_0 e^{-z/z_{inj}}$, that considers the exponential decay of the ballistic intensity travelling through a medium (given that it is scattered before leaving the

[§]As a general rule, every time we mention scattering, we refer to isotropic scattering, unless stated otherwise.

[‡]The slab geometry can be well approximated by a flat medium with a finite thickness and infinite lateral dimensions, as shown in Fig. 1.1a. When studying the light transmitted or reflected by the scattering slab, only the finite dimension (z) is of relevance.

medium). The injection depth z_{inj} is the depth at which the light starts diffusing, or the effective diffusive source. This distance is: $z_{inj} = \ell_t \cos\alpha$, where α is the angle of incidence of the beam with respect to the normal to the sample.[37,38]

Aside from the source, in order to solve eq. 1.4 it is necessary to set the boundary conditions given by the sample. Following the approach developed by Zhu, Pine and Weitz[35,39] it is possible to determine the effect of the boundaries of the medium by imposing the conservation of energy fluxes in it. In this way we have that the intensity is non-zero at the edges, and zero at a distance from it, defined as the extrapolation length, z_e. The resulting extrapolation length is dependent on the effective reflection coefficient $\overline{R}$ of the interfaces of the sample and the transport mean free path:

$$z_e = \ell_t \frac{2(1+\overline{R})}{3(1-\overline{R})}, \tag{1.5}$$

where $\overline{R}$ is the Fresnel coefficient averaged over all angles and polarizations.[3,35] It might happen that the scattering slab is in contact with two different media, e.g. a glass holding the sample and air, in this case the extrapolation length will be different in each side of the sample (z_{e1}, z_{e2}), given that the reflection coefficient $\overline{R}$ is different. Taking all these conditions into account, the solution to the diffusion equation depending on the sources considered are:

$$I(z) = \frac{I_0}{D}\left(\frac{(z+z_{e1})(L+z_{e2}-z_{e1})}{L+z_{e2}+z_{e1}} + (z_{inj}-z)H(z-z_{inj})\right) \quad \text{for} \quad S(z) = I_0\delta(z-z_{inj}) \tag{1.6}$$

$$I(z) = \frac{I_0}{D}\frac{z_{inj}e^{-z/z_{inj}}\left(e^{z/z_{inj}}(z+z_{e1})(L+z_{e2}-z_{inj}) + e^{z/z_{inj}}(z_{inj}-z) - z_{inj}\right)(L+z_{e2}+z_{e1})H(z)}{(L+z_{e2}+z_{e1})}$$

$$\text{for} \quad S(z) = I_0 e^{-z/z_{inj}}, \tag{1.7}$$

where H is the Heaviside step function. As an illustrative example we plot in Fig. 1.1b,c) the intensity distribution inside a diffusive medium for the two types of sources mentioned before: the point source (Fig. 1.1b), and the exponentially decaying source (Fig. 1.1c).

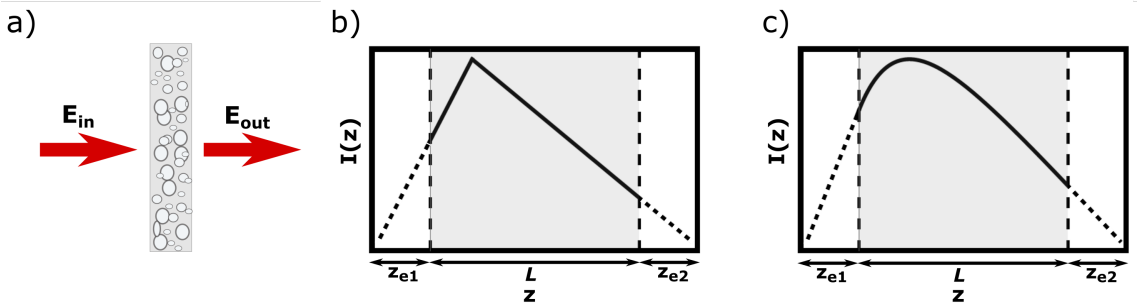

FIGURE 1.1: a) Schematic of a sample with slab geometry. b) Intensity distributions for a medium of thickness $L = 5\ell_s$ (shadowed part), and coefficients $\overline{R} = 0.3, D = 12$ originated by a point source following equation 1.6 and an exponential source given by equation 1.7(c)

In many situations it is useful to know how much diffuse intensity is being transmitted or reflected from the sample, as we discuss in Chapter 5. The total transmission through a diffusive medium is given by Fick's law for the current $J = -D\nabla I$,[40,41] resulting in:

$$T = -\frac{D}{I_0}\left.\frac{\partial I(z)}{\partial z}\right|_{z=L} \tag{1.8}$$

When $L \gg z_{inj} \simeq \ell_s$ and $L \gg z_{e1}, z_{e2}$, we obtain the Ohm's law for optics: $T \simeq \frac{\ell_s}{L}$.

1.2 Scattering and transmission matrices

Despite the usefulness of the diffusion theory to describe the propagation of the average intensity, it neglects light interference and therefore it does not provide the full picture of light transport inside the scattering medium. The most notable example of what diffusion theory fails to explain is the speckle pattern, a random interference intensity pattern resulting from the light scattered by a medium disordered in the order of the wavelength.[42] In principle, if we had all the information about the scattering medium such as the position of the scatterers, size, etc. it would be possible to determine exactly how light propagates inside.

It is well known that when light propagates through a material, e.g. a waveguide, its geometry imposes boundary conditions for the Maxwell equations, defining light propagation through the waveguides. Depending on the geometry of the waveguide, there will be a different number of solutions to the Maxwell equations that can propagate. These solutions are called propagating modes of the waveguide or the system. This same concept of propagating modes also holds in a disordered scattering medium. In a real sample there is a limited number of supported propagating optical modes: $2M$, where the 2 accounts for reflection and transmission, as we see later. An optical field propagating through a scattering medium can therefore be described as a combination of the $2M$ orthogonal modes. These propagating modes are also known as the scattering channels of the sample. It is possible to represent the scattering medium as a scattering matrix in the basis of these propagating modes such that:

$$E_{out} = SE_{in}, \tag{1.9}$$

where E_{out} is the outgoing electric field, E_{in} the incoming one and S is the $2M \times 2M$ scattering matrix.[43] The knowledge of this matrix allows to determine the output field once the input is known.

In a sample with a slab geometry, as shown in Fig. 1.2, it is necessary to take into consideration only fields coming from the left or from the right. In that case, we have a tensor S describing the scattering sample:[43]

$$S = \begin{pmatrix} r^{-+} & t^{--} \\ t^{++} & r^{+-} \end{pmatrix}, \tag{1.10}$$

where the first signs ($+$ and $-$) show the direction of the incident beam and the second, the direction of the outgoing one (as indicated in Fig. 1.2).The terms r and t represent the $M \times M$ reflection and transmission matrices, respectively.

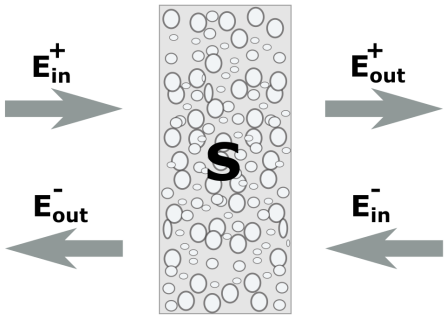

FIGURE 1.2: Schematic of the incident electric fields on a scattering sample with a slab geometry.

Given that in the experiments performed in this thesis we are only interested in the illumination coming from the left, and mostly interested in the transmitted intensity, the problem simplifies and the only term relevant to us is the transmission matrix t^{++}, that we will refer as t for simplicity. The transmitted field through a scattering medium, then follows the equation:

$$E_{out} = tE_{in}. \tag{1.11}$$

The dimensions of the transmission matrix $(M \times M)$ depend primarily on the illuminated area of the sample. In the waveguide geometry, the illuminated area at the entrance is the same that at the output, therefore following eq. 1.11, the transmission matrix is square. In these cases it is possible to choose a complete and orthogonal basis of propagating TE and TM modes, that fully describe light propagation.

In the slab geometry there are no lateral constraints and light can spread sidewise as it propagates, following a diffusion process. This implies that at the output of the sample the beam is broader than at the entrance, resulting in a rectangular transmission matrix ($N \times M$, with $N > M$). As a consequence, in this case it is not possible to choose a basis that is both complete and orthogonal. In this geometry it is common to use an over-complete set of modes describing the propagation through the sample such as the number of diffraction limited spots contained in the illuminated area A:[27]

$$N_A \simeq \frac{2\pi A}{\lambda^2}, \tag{1.12}$$

where the factor 2 is due to two orthogonal polarizations and λ is the wavelength of the beam.[44] When we consider the area illuminated at the entrance of the slab, $N_A = M$ and at the output of the medium $N_A = N$. As an example, from equation (eq. 1.12) we have that for a wavelength $\lambda = 633\,\text{nm}$ the number of propagating modes in an illuminated area of $1\,\text{mm}^2$ is around one million, resulting in a matrix of enormous dimensions to work with.

For a particular realization of disorder the transmission matrix t connects the incoming and outgoing fields of the sample. It is important to note however, that the two orthogonal polarizations of the field are independent of each other and even though the transmission matrix (characterized by the disorder) remains unchanged, the two polarizations give rise to different output fields. If we take into account polarization, the transmission matrix t takes the form:

$$\begin{pmatrix} E_{out_\perp} \\ E_{out_\parallel} \end{pmatrix} = \begin{pmatrix} t_{\perp\perp} & t_{\perp\parallel} \\ t_{\parallel\perp} & t_{\parallel\parallel} \end{pmatrix} \begin{pmatrix} E_{in_\perp} \\ E_{in_\parallel} \end{pmatrix}. \tag{1.13}$$

For simplicity we consider the case in which we are filtering out one polarization channel both in the incident and outgoing fields, unless it is stated differently.

The use of samples with slab geometry makes it more difficult to fully describe the system. However, as we will mention later, it is possible to obtain some analogies from the theory that works in the wave-guide geometry. In the wave-guide geometry where the transmission matrix is square, by using eigenvalue decomposition we can write t as:

$$t = U\Gamma U^{-1}, \tag{1.14}$$

where U is a square and unitary matrix performing the basis transformation between the free space modes incident on the sample and the transmission eigenchannels (or eigenvectors) of the sample and vice versa. Γ is a diagonal square matrix, with real and positive elements τ representing the eigenvalues of the sample or transmission coefficients. The distribution of the eigenvalues τ is described using Random Matrix Theory.

When the sample under study has the slab geometry, the transmission matrix is rectangular ($N \times M$) where N are the modes at the output surface and M the modes at the input. In this case, we would need to follow a singular value decomposition ($t = U\Gamma V^\dagger$ instead of eq. 1.14) where now U is a $N \times N$ matrix and $V^\dagger$ is $M \times M$. In this situation it is not possible to obtain a diagonal Γ matrix and the maximal number of diagonal elements in Γ is $\min(N, M)$. The distribution of the singular values in the case of slab geometry is not trivial, however when the thickness of the slab is not too large, (a few micrometers generally), numerical calculations[45,46] showed that Random Matrix Theory is a good tool to describe its distribution, despite the fact that it is originally only valid for waveguide geometries.

1.3 Random Matrix Theory

Random matrix theory (RMT) is a mathematical tool to study the statistical properties of large matrices with random distributed elements. It was originally introduced in 1928 by Wishhart,[47] but it was not until 1950's that it emerged as a useful approach in nuclear physics, to study the spacings between the energy levels of slow neutron resonances in nuclear reactions.[48,49] After that, RMT was shown to be useful in different areas of physics such as quantum chaos, quantum field theory and wave propagation through disordered media.[43,50,51]

RMT is based on the assumption that the complex system can be described by a random Hamiltonian or potential[¶] . However it takes into account physical constraints such as energy conservation, which allows it to represent very accurately physical phenomena. RMT provides the probability distribution of the eigenvalues of the matrix elements. The probability density of the transmission eigenvalues through a disordered medium is described by the Dorokhov-Mello-Pereyra-Kumar (DMPK) distribution:[43,52]

$$P(\tau^2) = \langle \tau^2 \rangle \frac{1}{2\tau^2\sqrt{1-\tau^2}}, \tag{1.15}$$

where $\langle \tau^2 \rangle \approx \ell_t / L$ is the averaged transmitted intensity through the sample. The probability density function is shown in figure 1.3. The function in equation 1.15 has two divergences: one at 1, and the other at 0. The divergence at 1 is integrable and therefore it implies the probability of finding eigenvalue coefficients 1 is finite. At zero, the function is not integrable, meaning that the eigenvalues can not reach the value 0, so the minimum value used as truncation of the distribution is generally $\tau^2 = cosh^{-2}(L/\ell_t)$.[38,43]

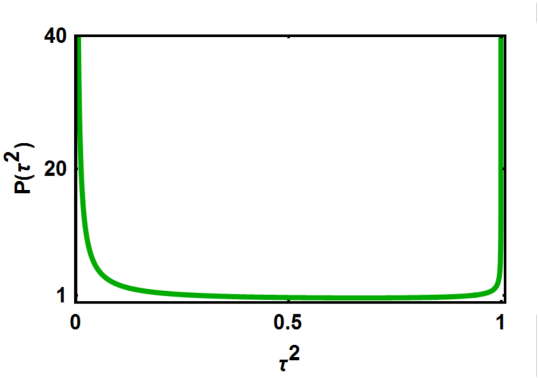

FIGURE 1.3: Probability density function of the intensity eigenvalues according to DMPK distribution.

The fact that the transmission coefficients through a scattering medium follow the distribution in eq. 1.15 entails an important consequence. From the distribution we see that the number of eigenvectors with average transmission is very small, therefore the wave transport through the

[¶] In optics the concept of a random potential can be seen as a system with random variations of the refraction index in the order of the wavelength.

sample is given by a combination of eigenvectors with transmission coefficients close to 1 (totally transmitted) or close to 0 (totally reflected). It is common to refer to eigenvectors or channels with transmission coefficient close to 1 as "open" channels, and to those with transmission close to 0 as "closed" channels.[53] Numerical simulations show the existence of such channels, even in a slab geometry.[45,46]

Experimental coupling to open and closed channels has been a subject of great interest from the very beginning, however success in fully coupling to these channels has been very limited in optics,[26–28,54] with a recent exception in acoustics.[55] In an equivalent way several experiments attempted to measure the DMPK distribution of eigenvalues,[56–58] but instead they retrieved a distribution similar to the Marcenko-Pastur distribution, described in the next section. It was shown numerically[46] that in order to access or visualize the DMPK distribution consequence of RMT it is necessary to have full control over the input and the output channels of the system. When the fraction of controlled channels is slightly smaller than 100%, the peak corresponding to the open channel quickly dissapears and the distribution gradually converges to the Marcenko-Pastur distribution. This is because the constraints imposed by RMT result in the matrix elements to yield correlations between themselves,[43] the moment all these elements are not fully measured or controlled, the correlations are less and less visible until the system becomes completely uncorrelated. Given that most experimental situations are in the uncorrelated regime, in the next section we briefly discuss the eigenvalue distribution in this case.

1.4 Uncorrelated Transmission Coefficients model

As discussed above, if in a experiment only a small region of the transmission matrix or channels are addressed, as it is the case in a practical situation, correlations coming form the RMT are not visible, and the elements of the transmission matrix can be treated as uncorrelated. In the Uncorrelated Transmission Coefficients (UTC) model the eigenvalues or singular values do not follow the DMPK distribution, therefore there are no open or closed eigenchannels. In this case they folow the probability distribution given by the Marcenko-Pastur law:[59]

$$P(\tau) = \frac{\gamma\sqrt{\tau^2 - \tau_{min}^2}\sqrt{\tau_{max}^2 - \tau^2}}{\pi\tau}, \tag{1.16}$$

where $\tau_{min} = 1 - \sqrt{1/\gamma}$ is the minimum singular value, $\tau_{max} = 1 + \sqrt{1/\gamma}$ the maximum singular value and γ is the aspect ratio of the matrix, therefore taking into account the cases where the transmission matrix is not squared. The distribution of singular values as well as τ_{min}, τ_{max} are very dependent on γ. In Fig. 1.4 we plot the distribution on eq. 1.16 for different values of γ.

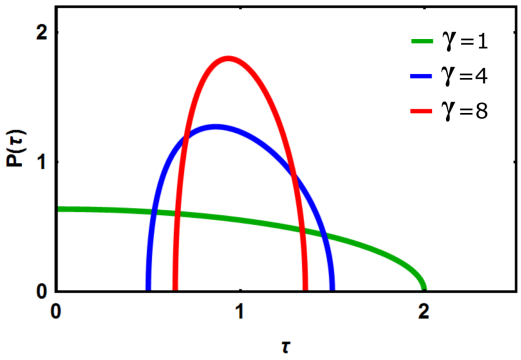

FIGURE 1.4: Probability distribution for the singular values τ given by the Marcenko-Pastur law, when considering different γ

In summary, although real scattering media are properly described using RMT and the transmission elements are correlated due to energy conservation, in practical cases these correlations are not observable and the use of UTC model can simplify the calculations, as we discuss in Chapter 3, therefore becoming more convenient. In this thesis we will be generally using the UTC model for the calculations. We will consider as well RMT when studying the distribution of eigenvalues in Chapter 5.

Chapter 2

Wavefront control in multiply scattering media

In this Chapter we look at the basic concepts of wavefront control and how interference determine the output intensity. We study as well two of the more common wavefront modulators: liquid crystals and Digital Micromirror Devices (DMD), reviewing their advantages and disadvantages. Given that in the experiments presented in this thesis we use a DMD, we give details of how these devices work and how the phase or amplitude of the wavefront can be controlled. In the final part we discuss the algorithm we designed and used for the wavefront optimization. Most of the information presented in this chapter is a review from the literature. The only contribution of my own is the custom algorithm defined at the end of the chapter.

2.1 Wavefront control

When coherent light propagates through a disordered material, most of the light is elastically scattered[†] by the inhomogeneities of the medium. Given that elastic scattering preserves the coherence, the different modes propagating through the medium interfere with each other, determining the global propagation through the medium. The principle behind wavefront control or wavefront shaping techniques relies on modifying the interference between these propagating modes, which leads to a different distribution of the optical energy, i.e. different light propagation. As we discussed in Section 1.2 even from a small illuminated area of ≈ 1 mm^2 in a highly scattering medium there are millions of propagating modes. To gain intuition, we first look at the simplest case: the propagation of two modes, that will help us to understand the full behaviour easier. We consider two modes (E_1, E_2) interfering with each other and giving rise to the field E:

$$E = E_1 + E_2 = A_1 e^{i\phi_1} + A_2 e^{i\phi_2} \tag{2.1}$$

[†] In the case the medium has negligible absorption, as it is the case we consider in this thesis.

where A_1, A_2 are the amplitudes of the modes 1 and 2 and ϕ_1, ϕ_2 are the respective phases. Following eq. 2.1, the intensity is:

$$I = E \cdot E^* = I_1 + I_2 + 2\sqrt{I_1 \cdot I_2}\cos(\phi_1 - \phi_2). \tag{2.2}$$

From the above equations we can see that a modification in the amplitude or phase of one of the modes modifies the interference term, leading to a higher (or lower) intensity and, consequently, modifying light propagation. Wavefront shaping techniques are based on the manipulation of the field incident on the sample in order to change the output field and consequently the propagation of light through the medium. The manipulation of the phase and/or amplitude is done using spatial light modulators. These devices contain a multitude of pixels that can independently control the amplitude or phase, therefore allowing the control of multiple propagating modes.

2.1.1 Wavefront modulators

The manipulation of the phase or amplitude of a wavefront is performed using Spatial Light Modulators (SLM). There are various types of SLM available, the two more broadly used for wavefront shaping techniques are Liquid Crystals SLM (LC-SLM) and Digital Micromirror Devices (DMD).

LC-SLM are capable of modulating the phase of the wavefront by controlling the orientation of the liquid crystal molecules in the different pixels. The big advantages of LC-SLM are that they have a large number of pixels and they are energy efficient, in comparison with other commercially available SLMs. However, despite their advantages, they also have some disadvantages. One of the disadvantages is the slow response time, limited by the time it takes the molecules to reach a stable orientation, resulting in a general speed limit around 100 Hz. The second important disadvantage is that in most available devices phase modulation is coupled to the modulation of the polarization of the beam, which prevents a simple independent phase modulation.

A common alternative to LC-SLM are the Digital Micromirror Devices. A DMD is a Micro-Opto-Electromechanical System (MOEMS) consisting of an array of mirrors of a few microns in size. Each mirror can be individually tilted to $\pm 12^\circ$, representing the "on" or "off" states. The main advantage of a DMD is that they can work at much higher speeds than LC-SLM (tens of kHz), which makes them an excellent option when dealing with live tissue for instance, where in general the media can be considered static only for a few milliseconds.[60,61] The main disadvantage of these devices is that they are binary amplitude-only modulators. Although it is possible to modulate the phase using Lee holographic techniques[62] , it is necessary to filter components in the Fourier plane as described in Section 2.2.2, but it is not as energy-efficient as a LC-SLM.

Although it was shown that it is possible to control both amplitude and phase successfully,[63,64] it is technically challenging, so in the majority of the cases either phase or amplitude are modulated, not both at the same time. It was shown in the literature,[14,15] and briefly discussed in

the next subsection, that when only the phase of the wavefront is modulated it is possible to obtain larger variations in the output intensity than when only the amplitude is modulated. For this reason, most experiments in wavefront control are performed by modulating only the phase.

The experiments presented in this thesis are performed using a DMD so in the next section we give details on how to manipulate amplitude or phase using a Digital Micromirror Device. The DMD used for the experiments in this thesis is a Texas Instruments DLP 9500. It consist of 1920 $\times$ 1080 squared mirrors of sizes 10.8 $\times$ 10.8 µm, with a maximal refresh rate of 23.1 kHz.

2.2 Amplitude and Phase modulation using a DMD

In this section we examine two main possibilities for modulating the wavefront: amplitude-only and phase-only modulation. In order to compare the two, we examine how much energy can be focused at the output of the medium, following the two different approaches. Focusing light into a diffraction spot at the output of the medium has been widely used and well characterized,[14,15] therefore the evaluation of the intensity deposited at the focus is a good measure of the wavefront control. In this section we examine how much intensity could be deposited at the focused spot using phase-only and binary amplitude modulation.

2.2.1 Binary amplitude modulation

The more straightforward approach to create a focus using a DMD binary amplitude modulator is by amplitude modulation.[15] It consists of turning "on" or "off" the different mirrors (or pixels) in the DMD. This is the same as assigning an amplitude of zero to one of the interfering waves in eq. 2.1. A graphical explanation of this concept using phasor diagrams is shown in Fig. 2.1. In Fig. 2.1a) we represent the sum of four random field components (red arrows) contributing to the intensity of a hypothetical focus spot. The total field is represented by the blue arrow. As we can see there are field elements like E_2 that contributes to the reduction of the total field at that spot. If we cancel the contribution of E_2 by assigning a zero amplitude to it, the total field at the focus spot will increase, as we see in Fig. 2.1b), therefore resulting in larger intensity deposited at the selected spot.

2.2.2 Phase modulation: Lee holography method

Phase modulation consists of modifying the phase in different areas of the electric field impinging on the medium. In the phasors diagram this is equivalent to rotating the small red arrows. If we start from the sum of random fields (Fig. 2.1a), if we rotate any of the red arrows aligning them with each other, i.e. adding them all in phase, the total field is maximal (Fig 2.1c) and larger than what could be achieved by amplitude-only modulation.

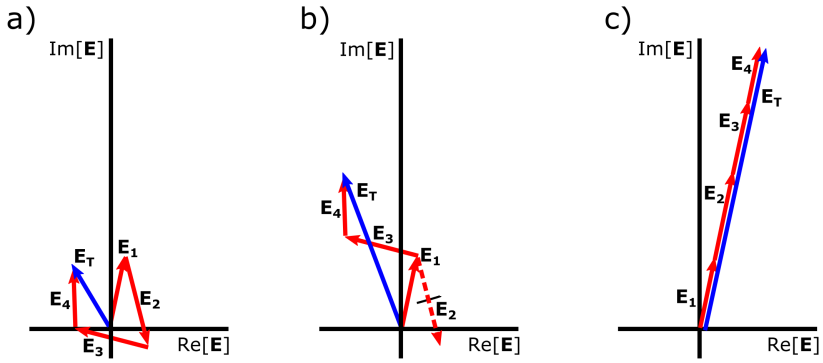

FIGURE 2.1: Examples of phasor sums of random complex components. a) Phasor sum of random components, simulating the field obtained in the target area to optimise when the wavefront is not shaped. b) Resultant sum when the components contributing to decrease the field have been cancelled in amplitude. c) Resultant sum when all the components have been optimised in phase.

Since a DMD is an amplitude-only modulator, we cannot modulate the phase directly, as can be done using a liquid crystal SLM. To modulate phase with an amplitude modulator, we use the Lee holography method.[62] Lee holography is a type of Computer Generated Hologram (CGH) that uses the similarities of CGH with interferograms to design or reconstruct different phases. The equivalent fringes in the interferogram are displayed on the screen of the DMD to form the CGH.

To give an insight on how the phase of the wavefront can be modulated in this way, we use the simplest example, in which we consider the amplitude pattern displayed is sinusoidal, in the form:

$$f(x) = \frac{1}{2}\left[1 + cos(2\pi x k_0 - \phi(x))\right] \tag{2.3}$$

where, x is the spatial coordinate of the pattern, k_0 the spatial frequency and $\phi(x)$ accounts for the lateral shift of the sinusoidal pattern. Once this pattern is loaded onto the DMD, we use a lens to perform a Fourier transform of it,[3,65] as illustrated in Fig. 2.2, leading to:

$$\mathcal{F}\{f(x)\} = \sqrt{\frac{\pi}{2}}\delta(k) + \sqrt{\frac{\pi}{8}}e^{i\phi(x)}\delta(k - 2\pi k_0) + \sqrt{\frac{\pi}{8}}e^{-i\phi(x)}\delta(k + 2\pi k_0) \tag{2.4}$$

where the first term is the zeroth diffracted order and the second and third are the +1 and -1 orders. In the Fourier plane of this lens we use a diaphragm to filter out the zeroth and one of the first diffracted orders (for example the last term in eq. 2.4). Using a second lens, we perform again a Fourier Transform but only of the filtered first diffracted order, obtaining:

$$\mathcal{F}\{\sqrt{\frac{\pi}{8}}e^{-i\phi(x)}\delta(k + 2\pi k_0)\} = \frac{1}{4}e^{i(2\pi x k_0 + \phi(x))}. \tag{2.5}$$

As a result of this second filtering we obtain a plane wave where the spatial shift information $\phi(x)$ defined in equation 2.3 is now encoded in as a phase shift in the plane wave: $e^{i(2\pi x k_0 + \phi(x))}$.

The experimental implementation of phase modulation with a DMD has however some subtleties. First of all, in order to obtain a proper phase modulation using this method, it is very

important that we have a 4-f system, as shown in Fig. 2.2. The reason for this is that only in the image plane of the system we will have the desired phase transformation, so it is there where the sample should be placed. If the distances are not the appropriate ones, quadratic phases will be added to the phase pattern,[65] due to the Fourier transforming properties of the lenses, which will reduce the efficiency of phase modulation.

Secondly, as we can see from eq. 2.5, even under the assumption of perfect sinusoidal modulation, only $1/4$ of the initial field is being used for the phase modulation, so using a DMD to modulate the phase is not very energy efficient. In addition, in order to generate an amplitude interferogram, half of the display has zero or near zero amplitude, resulting in roughly half the energy coming to the SLM lost. In our experimental case, given that we have a binary amplitude modulator, we load a binary square wave in the DMD chip instead of a sinusoidal pattern, with half of the mirrors in the 'off' state. The main difference coming from using the squared wave is that there will be higher orders generated in the Fourier plane, so even less energy will be controlled. Taking all this into account, the total energy efficiency of the DMD to modulate the phase is around 5-10% of the total intensity, which is far from the roughly 50% that can be achieved in LC-SLM. However the advantages such as speed can overcome the energy efficiency limitations in certain applications.

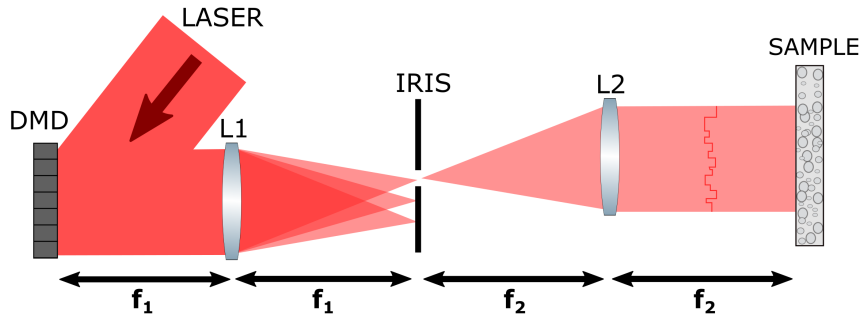

FIGURE 2.2: Schematic of the Lee holography method to perform phase modulation with a DMD. A lens (L1) performs the Fourier transform of the pattern loaded on the DMD, generating its Fourier Transform at distance f_1 from the lens. At this place an iris filters the first order of the diffraction pattern (eq. 2.4). A second lens (L2) performs the second Fourier Transform, resulting in the phase modulation (eq. 2.5) that is finally impinging on the sample.

In order to independently control the phase of different regions of the wavefront, the full array of pixels of the DMD is divided into smaller groups of mirrors, referred as "macropixels" (squared subarrays of pixels controlled independently) each with a sinusoidal-like pattern loaded, where the shift of each of them can be tuned independently. These macropixels are the smallest units used to perform phase modulation with the DMD.

The size of the macropixels is an important factor. In principle, given that different modes of the sample (or diffraction limited spots) can be considered independent, (as discussed in Section 1.2) the process will be more efficient when the individual macropixels match the size of the individual modes, i.e. when they are diffraction limited in size. The macropixels in our experiments were a

group of 12 by 12 mirrors, therefore the real size of them was 129.6 $\times$ 129.6 µm. In order to make them diffraction limited we had to choose the lenses and extra elements accordingly, as we will detail in the respective Chapters 4, and 5.

2.3 Wavefront optimization algorithms

The field leaving the sample is given by the product of the transmission matrix of the sample and the incident field, as described in eq. 1.11. If we had full knowledge of the transmission matrix, we could find the incident field needed to obtain the desired output field. However, as discussed in Section 1.2, measuring the transmission matrix experimentally is a very challenging task, mainly due to its large dimensions.[44,56]

However, if the goal of the experiment is to increase the intensity in a spot (such as light focusing), or any other that can be easily measured with a feedback device, it is possible to use an approach that does not require measuring the transmission matrix, but instead it is based on the use of an iterative algorithm. In these cases, in order to optimize the wavefront three main elements are needed: a wavefront modulator, a detector providing the feedback and an algorithm deciding which wavefront should be loaded in the modulator, according to the feedback. This is the approach we use in the experiments described in this thesis. The basic setup of the experiment is represented in Fig. 2.3.

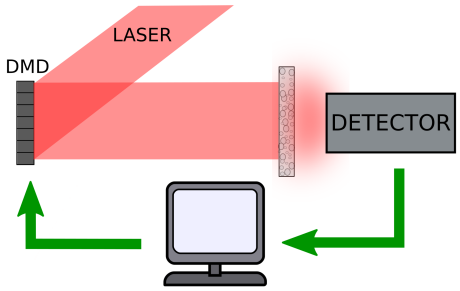

FIGURE 2.3: Schematic of the basic experimental set-up. The detector provides feedback that is analysed by the computer. After the analysis is done, the DMD or SLM is addressed by the software to display a pattern according with the feedback gathered.

In order for the algorithm to find the optimal configuration, it has to evaluate the feedback element for the different phases or amplitudes of the input. In the experiments of this thesis, we use an iterative algorithm to increase the intensity in transmission (at one diffraction limited spot and the total transmitted light), using phase-only modulation. The task of our algorithm is to find the input phase that maximises the intensity at the desired place. One might think that the easiest approach is to try all the independent input phases, and keep the ones leading to the maximal intensity. However, as we saw in eq. 2.2, the interference term follows a sinusoidal curve as the phase between the interference parts is changed, therefore it is possible to speed up the process by just taking 2 samplings of the sinusoidal, fitting the data to the function $A_0 \cos(\frac{2\pi}{\lambda}x +$

$\phi)$. However, the fewer data points we take the more sensitive to noise the measurements are. Therefore it is common to choose 4 or 6 samplings of the sinusoidal as a good compromise between speed and Signal to Noise Ratio (SNR).[66] In our experiments we found that 6 data points per iteration was a good compromise and that was the sampling used for the experiments in this thesis.

Types of algorithms

An important decision when designing the algorithm is to choose how many modes are being modulated in each iteration, or in other words, how many macropixels are being addressed at the same time. There are several variants in the literature[67] but here we only briefly discuss two that lead to our particular choice. These two basic algorithms are the so called step-wise and the partitioning algorithms.[67] Both change the phase or amplitude of a set of macropixels while the remaining macropixels are kept unchanged, basically the only difference is in the number of macropixels modulated at a time. When we are interested in increasing the intensity in a given region, e.g. focusing to a spot, using wavefront shaping, the number of macropixels addressed is particularly important in the Signal to Noise Ratio (SNR). The more macropixels we modulate, the larger the modulated signal will be, which will increase the chances the algorithm makes the right decisions when picking the optimal phase patterns.

Step-wise and partitioning algorithms

The step-wise algorithm modulates just one macropixel at a time. Given that different modes of the sample can be considered independent, modulating the macropixels (and therefore the modes) independently should lead to the best results. The main disadvantage of this algorithm is that the signal to noise ratio in this case is very small because the signal is given by only one macropixel.

A good alternative is the partitioning algorithm. In this case instead of modulating just one macropixel at a time, approximately half the total number of macropixels is modulated in one iteration. The macropixels to modulate are chosen randomly each time. This allows the signal to noise ratio to be maximal in each iteration.

Custom algorithm

In our experiments we used a variation of the partitioning algorithm, combining macropixels of different sizes. Figure 2.4 shows the dynamic of a typical intensity optimization. At the beginning of the optimization, the signal in the detector is small, so the measurement is noisy. In order to quickly increase the signal, we group 8 by 8 macropixels, changing a large percentage of them, around 30% up to iteration 2500 (first grey solid line in the figure). This allows the intensity in the target to increase fast, but given that the number of elements independently controlled is small

and the size of the macropixels is not optimal, the intensity increase becomes slower. At this point we choose a smaller group of macropixels (4 by 4), also reducing the percentage of macropixels addressed, which allows the intensity optimization to increase again. We continuously decrease the size of grouped macropixels (in the figure represented by the dashed vertical lines) until we address independent macropixels. At the same time we progressively decrease the percentage of macropixels addressed, up to 2% approximately.

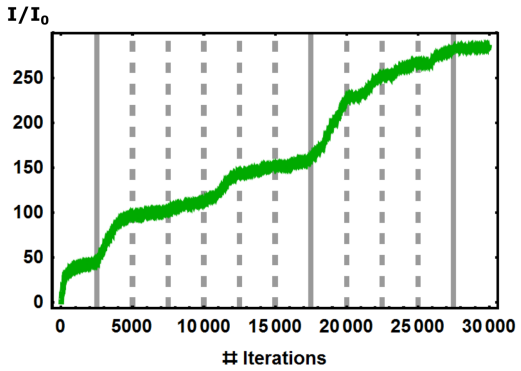

FIGURE 2.4: Graph showing the dynamic increase of the optimized intensity in which total transmission was being maximized. Solid vertical lines represent a reduction on the number of grouped macropixels addressed independently and dashed vertical lines indicate a reduction in the percentage of macropixels addressed in each iteration.

Chapter 3

Wavefront control and effect of imperfections: focusing and optimal transmission

In this chapter we present the ideal optimization that can be achieved by wavefront shaping and the influence that imperfections in the modulation have over it. We discuss the two observables that are measured in the experiments shown in the next two chapters of this thesis: focusing light into a diffraction limited spot and the increase of total transmission through a scattering medium. We first assume that one can achieve the wavefront needed, i.e. we assume the wavefront is ideally modulated, and therefore technical limitations from the experiment are not taken into consideration. In the final part of the chapter we present the influence of the imperfections and how these should be taken into account.

The derivation of the ideal focusing enhancement is taken from the literature[44,68] as well as the the influence of imperfections over the wavefront modulation.[44,68] My contributions to this chapter are the derivation of the maximal total transmission under experimental conditions as well as the study of the distribution of the ideal enhancements of the total transmission and optimal focusing.

3.1 Ideal wavefront control

In this section we explore the optimizations that can be achieved assuming ideal wavefront control in two cases: focusing through a scattering medium and increasing total transmission through it.

3.1.1 Focusing optimization

Light control in scattering media by wavefront shaping techniques is often measured by how much of a plane wave can be focused into a diffraction-limited speckle spot after passing through a scattering medium.[14] This figure of merit is referred to as enhancement factor and it is defined

as the ratio between the intensity focused in the optimized speckle spot over the average intensity at that spot with a non-optimized wavefront:[14,44]

$$\tilde{\eta} = \frac{\tilde{I}_f}{\langle I_f \rangle}, \tag{3.1}$$

where $\langle \cdot \rangle$ represents the ensemble average over different realizations of disorder, $\tilde{I}_f$ is the intensity in the optimized speckle spot f and I_f is the intensity at the same spot with a non-optimized wavefront.

In the following we derive the optimal enhancement factor following the same procedure used in the literature.[44,68] The intensity at one speckle spot at the output of the scattering material is given by:

$$I_f = \mid \sum_i^N t_{fi} \cdot E_i \mid^2, \tag{3.2}$$

where N is the number of modes transmitted through the sample, E_i is the incident field at the input channel i and t_{fi} are the transmission matrix elements contributing to the output channel f from the input i. The maximal value that the intensity in equation I_f can take is given by the Cauchy-Schwartz inequality:

$$\mid \sum_i^N t_{fi} \cdot E_i^* \mid^2 \leq \sum_i^N \mid t_{fi} \mid^2 \sum_i^N \mid E_i \mid^2 . \tag{3.3}$$

The maximal intensity that is possible to concentrate in one speckle spot is then given by the equality of these two terms. The two terms are equal if the electric field $E_i = \propto t_{fi}^*$. In order to have a normalized total intensity $\sum_i^N \mid E_i \mid^2 = 1$ we choose the proportionality factor to be the normalization factor, so that $E_i = C\, t_{fi}^*$, with $C = \left(\sqrt{\sum_i^N \mid t_{fi} \mid^2} \right)^{-1}$. We refer to this field as $\tilde{E}_i$ to indicate it is the optimal field for the desired output. The optimal intensity at the spot f is given by:

$$\tilde{I}_f = \sum_i^N \mid t_{fi} \mid^2 \sum_i^N \mid \tilde{E}_i \mid^2 = \sum_i^N \mid t_{fi} \mid^2, \tag{3.4}$$

where the last simplification is due to the normalization of the incident field.

The non-optimized intensity can be described either as a different field impinging on the same scattering medium ($\mid \sum_i^N t_{fi} \cdot E_i' \mid^2$) or as the same optimized input filed $\tilde{E}_i$ impinging onto a completely different region of the sample, defined by a different transmission matrix ξ_{fi}. We will use the latter approach for simplicity. In this way, the non-optimized intensity at the spot f is given by:

$$I_f = \mid \sum_i^N \xi_{fi} \cdot \tilde{E}_i \mid^2 = \sum_i^N \mid \xi_{fi} \mid^2 \mid \tilde{E}_i \mid^2 + \sum_i^N \sum_{i' \neq i}^{N-1} \xi_{fi} \tilde{E}_{i'}^* \xi_{fi'}^* \tilde{E}_i. \tag{3.5}$$

In order to calculate the enhancement factor (defined in eq. 3.1), we ensemble average the non-optimized intensity I_f over different realizations of disorder. In this case, the terms representing the disorder of the system are the matrix elements ξ_{fi}, so we obtain:

$$\langle I_f \rangle = \langle \sum_i^N \mid \xi_{fi} \mid^2 \mid \tilde{E}_i \mid^2 \rangle + \langle \sum_i^N \sum_{i' \neq i}^{N-1} \xi_{fi} \xi_{fi'}^* \tilde{E}_i \tilde{E}_{i'}^* \rangle. \tag{3.6}$$

Assuming different elements of the transmission matrix are uncorrelated, the second term reduces to zero when averaged over a large number of realizations of disorder, and so the remaining averaged intensity is:

$$\langle I_f \rangle = \sum_i^N \langle \mid \xi_{fi} \mid^2 \rangle \mid \tilde{E}_i \mid^2 = \langle \mid \xi_{fi} \mid^2 \rangle \sum_i^N \mid \tilde{E}_i \mid^2, \tag{3.7}$$

thus the enhancement factor becomes:

$$\tilde{\eta} = \frac{\tilde{I}_f}{\langle I_f \rangle} = \frac{\sum_i^N \mid t_{fi} \mid^2 \sum_i^N \mid \tilde{E}_i \mid^2}{\langle \mid \xi_{fi} \mid^2 \rangle \sum_i^N \mid \tilde{E}_i \mid^2} = \frac{\sum_i^N \mid t_{fi} \mid^2}{\langle \mid \xi_{fi} \mid^2 \rangle}. \tag{3.8}$$

The average value of the enhancement factor is then given by:

$$\langle \tilde{\eta} \rangle = \frac{\langle \tilde{I}_f \rangle}{\langle I_f \rangle} = \frac{\sum_i^N \langle \mid t_{fi} \mid^2 \rangle}{\langle \mid \xi_{fi} \mid^2 \rangle} = \frac{N \langle \mid t_{fi} \mid^2 \rangle}{\langle \mid \xi_{fi} \mid^2 \rangle} = N, \tag{3.9}$$

where the last simplification is possible given that the matrices t and ξ are uncorrelated and the average over disorder of the absolute value squared is the same for both. Equation 3.9 recovers the results presented in the literature.[14,44,68] This result has been broadly used in the literature as the reference optimal value when focusing through scattering media. However, although the average value give us a very good estimate of what we can hope for, this is not the value we obtain from a single measurement of the enhancement factor. When we make a single measurement we measure the enhancement factor given by eq. 3.8, which follows a probability distribution that has not been investigated so far. In the next section we look into the properties of this probability distribution and show its dependence on the number of independent modes N.

Enhancement factor distribution

The focusing enhancement factor is given by the ratio of the optimized intensity $\tilde{I}_f$ divided by the average intensity, as seen from eq. 3.8. Given that the average intensity is a constant, the probability distribution of the enhancement is given by the probability distribution of the optimized intensity $\tilde{I}_f$. As defined in eq. 3.4, the optimized intensity is given by the sum of intensity terms $\mid t_{fi} \mid^2$. This term comes from the optimal field intensity (eq. 3.4) and therefore its distribution is given by the components of the electric field. The real and imaginary parts of the electric field are normally distributed, therefore the modulus squared (i.e. the intensity) is the sum of two

normally distributed random variables squared:$\mid t_{fi} \mid^2 = \mid \Re[t_{fi}] \mid^2 + \mid \Im[t_{fi}] \mid^2$. The distribution of the sum of squared terms is given by the χ^2_2 distribution, where the sub index is the number of degrees of freedom (or number of terms summed up). As a consequence, the distribution of the enhancement factor is given by the sum of χ^2_2 distributed terms, which tends to a Gaussian distribution when the number of added elements is large ($N \gg 1$), for the Central Limit Theorem. In order to evaluate the probability distribution for all values of N we go into the details of the calculation.

It follows from the definition of chi-squared distributions that the sum of N terms χ^2_2 distributed also follows a chi-squared distribution, which is given by: χ^2_{2N}. If we consider N to be the sum of the two orthogonal polarizations $N = N_\perp + N_\parallel$, the resultant distribution is the result of the sum of these two polarizations:

$$P(\tilde{\eta}) = \frac{1}{2}\chi^2_{2N_\perp} + \frac{1}{2}\chi^2_{2N_\parallel} = \frac{1}{2}\chi^2_{(2N_\perp + 2N_\parallel)} = \frac{1}{2}\chi^2_{2N}, \tag{3.10}$$

where $N = N_\perp + N_\parallel$ and the factor $1/2$ is given by the denominator in equation 3.8: $\langle \chi^2_2 \rangle = 2$.

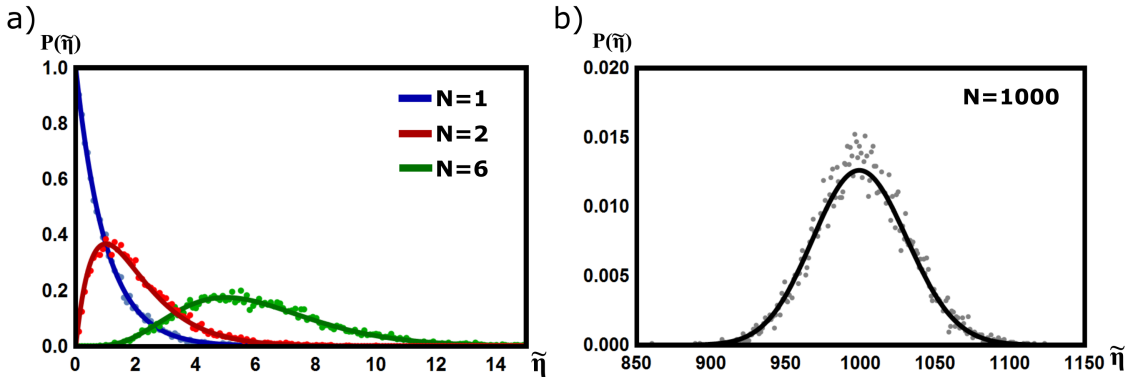

FIGURE 3.1: In these graphs we show the probability distribution of the enhancement factor for different number of modes N, where the solid line represents the probability distribution described in eq. 3.10 and the dots are numerical data for the given number of modes. On left hand side graph we show the widening of the function as the number of N increases, towards a more symmetric function. In the graph on the right side shows the function for a large number of independent modes $N = 1000$.

In figure 3.1 we show the normalized probability distribution of the ideal enhancement factor together with numerical data for different values of N. When $N = 1$ and therefore only one polarization mode is present, we obtain the exponential decay in intensity, whereas when two independent modes are present the Rayleigh distribution appears, as we should expect.[42] It is of particular interest to note how, for small values of N, (easily achievable in small core optical fibers) the enhancement factor can deviate significantly from the mean value. When the number of modes is much larger, as shown in the graph on the right, the distribution is closer to a Gaussian, as a result of the central limit theorem.

For the numerical analysis of the distribution of the enhancement factor, we defined a transmission matrix with normally distributed terms. The dots in Fig. 3.1 represent the normalized histogram of the summation of the absolute value squared of the transmission matrix elements, i.e. the dots represents the histogram of the summation: $\sum_{i=1}^{N} \mid t_{fi} \mid^2 = \sum_{i=1}^{N} \left(\mid \Re[t_{fi}] \mid^2 + \mid \Im[t_{fi}] \mid^2 \right)$, which leads to the distribution of the enhancement factor in eq. 3.8. The solid line curve represents the normalized χ^2_{2N} function.

3.1.2 Total transmission optimization

In the previous section we have seen how much of the incident wavefront we can redirect into one selected speckle spot, by looking at the ratio between the optimized and non-optimized fields. However, this is not the only thing that can be achieved by wavefront shaping the incident beam. Another application of wavefront shaping that we will implement in the experiment described in Chapter 5 is the increase of the total transmission of light through a scattering material. In this section we study the optimal transmission that can be achieved under ideal modulation and experimental situations using wavefront shaping.

Optimal transmission under ideal modulation

The transmitted field through a scattering material is determined by the incident field and the transmission matrix (eq. 1.11). The properties of the transmission matrix are well described using Random Matrix Theory (see Section 1.3). It was found by Dorokhov[52] that the transmission through scattering materials is described by a set of open channels (sample scattering channels with transmission close to unity) whereas the main contribution to the reflected wave was given by the closed channels (sample scattering channels with transmission close to zero), as discussed in Chapter 1. If the incident field is optimized so that it couples to an open channel, in principle it is possible to transmit all of the light.[43,52]

Experimental coupling to open channels is a subject of great interest in optics. Kim *et al*[54] designed an experiment where they measured the transmission matrix and calculated the open channels (or the ones with optimal transmission which was in fact much lower than 1). After implementing the incident field corresponding to that open channel, they achieved a total transmission 4 times larger than the non-optimized one. Choi *et al* showed as well the possibility to increase total transmission by a factor of 2 and reduce total reflection by iterative algorithms.[26] Another approach that was proved very useful in exploiting the coupling to high transmission channels was shown by Vellekoop and Mosk,[27] where they showed the increase in total transmission converges to the average universal value of $2/3$ when an optimal focus is created in transmission. This is because creating a focus in transmission is in fact done by mainly coupling to high transmission channels.[27,68]

One of the difficulties when attempting to couple to the open channels described by Random Matrix Theory (RMT) is that they are only well defined in the wave-guide geometry,[43,52,69] where the transmission matrix is square, as discussed in Section 1.3. In the slab geometry, for small thicknesses, there are simulations showing their existence,[45] as well as experiments showing that the DMPK distribution from RMT is still valid to some extent.[26–28,54] However in none of these cases the total transmission achieved was close to full transmission, as one could expect from coupling to open channels. This tells us that although RMT can be useful to describe some features or in particular cases, it is not fully describing the real situation.

As discussed in Section 1.3, RMT only only defines well the scattering material when there are the same number of modes through propagation, i.e. the transmission matrix is squared.[43] In addition, RMT also takes into account energy conservation, which as a consequence considers the transmission coefficients to be correlated. In a general experiment with a slab as scattering material, the transmission matrix is not squared. Furthermore, in general only a small part of the transmission matrix is illuminated in a experiment, so the correlations between the transmission coefficients described by RMT are not visible. In these cases, it is useful to consider the Uncorrelated Transmission Coefficients (UTC) model, where no correlations are considered between the transmission elements and there are no open or closed channels, as seen in Section 1.4.

We expect our experiments to be better described by the UTC than RMT model, given that the number of experimentally controlled modes is much smaller than the propagating modes through the sample, and therefore correlations between transmission coefficients should be negligible. Whereas in the RMT model the optimal transmission is 1 when coupling to an open channel, the optimal transmission that can be achieved assuming the UTC model has not been investigated in detail, and that is the purpose of the next subsection.

Experimental maximal transmission under ideal modulation

Here we derive the optimal total transmission that can be achieved when optimizing every individual channel. The procedure of this derivation is based on the optimization performed with the step-wise algorithm, in order to show the optimal situation that can be achieved with the experimental procedure. We optimize channel by channel and pick the phase of each of them that give us an optimal total transmission. The relation between input and output fields is given by the transmission matrix, so following eq. 1.11:

$$\begin{aligned} E_{O1} &= t_{11}E_{I1} + t_{12}E_{I2} + ... + t_{1N}E_{IN} \\ E_{O2} &= t_{21}E_{I1} + t_{22}E_{I2} + ... + t_{2N}E_{IN} \\ &\vdots \\ E_{ON} &= t_{N1}E_{I1} + t_{N2}E_{I2} + ... + t_{NN}E_{IN}. \end{aligned} \tag{3.11}$$

This equation shows the contribution of each input channel (E_{Ii}) to the output ones (E_{Oi}). The total field transmitted when no optimization is done is given by the sum of all the output modes N: $T_F = \sum_{k=1}^{N} E_{Ok}$. We assume phase-only modulation, and so the amplitude of the incident field is not modified in the optimization, therefore the intensity is uniformly distributed over all the incident channels:

$$E_{Ii} = \frac{1}{\sqrt{N}} e^{i\phi_i}, \quad \mid E_{Ii} \mid^2 = \frac{1}{N} \quad \text{and} \quad \sum_{i=1}^{N} \mid E_{Ii} \mid^2 = 1. \tag{3.12}$$

The contribution of the input channel E_{I1} to the total transmitted field is given by:

$$T_F \mid_{E_{I1}} = (t_{11} + t_{21} + ... + t_{N1}) E_{I1} = \sum_{j=1}^{N} t_{j1} E_{I1} = \mid \sum_{j=1}^{N} t_{j1} \mid e^{i\theta_{t1}} \cdot \mid E_{I1} \mid e^{i\phi_1}, \tag{3.13}$$

where θ_{t1} is the resultant phase of the sum of transmission matrix components t_{j1} and ϕ_1 is the phase component of E_{I1}, which is the phase that varies during the optimization. Using equation 3.12, the contribution of E_{I1} to the total transmitted field results:

$$T_F \mid_{E_{I1}} = \frac{1}{\sqrt{N}} \mid \sum_{j=1}^{N} t_{j1} \mid e^{(\theta_{t1} + \phi_1)} = A_1 e^{i(\theta_{t1} + \phi_1)}, \tag{3.14}$$

where $A_1 = \frac{1}{\sqrt{N}} \mid \sum_{j=1}^{N} t_{j1} \mid$.

In the step-wise algorithm we modify the phase of one channel (say E_{I1}) and look at the interference term of the intensity between the contribution of this channel and the rest of the channels, that works as a reference field. The contribution to the total field of the rest of the channels that are not being modified is given by:

$$T_F \mid_{T-E_{I1}} = \sum_{k \neq 1}^{N-1} \left(\sum_{j=1}^{N} t_{jk} E_{Ik} \right) = \sum_{k \neq 1}^{N-1} \left(\mid \sum_{j=1}^{N} t_{jk} \mid\mid E_{Ik} \mid e^{i(\theta_{tk} + \phi_k)} \right) = \sum_{k \neq 1}^{N-1} (A_k e^{i(\theta_{tk} + \phi_k)}). \tag{3.15}$$

Again to simplify the notation we define A_R as the absolute value of $T_F \mid_{T-E_{I1}}$ and ψ_R as the resultant phase, so that:

$$T_F \mid_{T-E_{I1}} = A_R e^{i\psi_R}, \tag{3.16}$$

where $A_R = \mid \sum_{k \neq 1}^{N-1} (A_k e^{i(\theta_{tk} + \phi_k)}) \mid$ and $\psi_R = Arg[\sum_{k \neq 1}^{N-1} (A_k e^{i(\theta_{tk} + \phi_k)})]$. The interference term between the modulated channel and the reference is given by:

$$\begin{aligned} T_I &= \mid A_1 e^{i(\theta_{t1} + \phi_1)} + A_R e^{i\psi_R} \mid^2 = (A_1 e^{i(\theta_{t1} + \phi_1)} + A_R e^{i\psi_R})(A_1 e^{-i(\theta_{t1} + \phi_1)} + A_R e^{-i\psi_R}) \\ &= \mid A_1 \mid^2 + \mid A_R \mid^2 + A_1 A_R (e^{i(\theta_{t1} + \phi_1 - \psi_R)} + e^{-i(\theta_{t1} + \phi_1 - \psi_R)}) \\ &= \mid A_1 \mid^2 + \mid A_R \mid^2 + 2 A_1 A_R \cos(\theta_{t1} + \phi_1 - \psi_R). \end{aligned} \tag{3.17}$$

Equation 3.17 shows the intensity interference when only one channel is modulated and the rest

act as a reference. The first two terms of the sum give the offset of the interference, or non-optimized total intensity as we discuss later. The last term in the sum is the interference term, that is changed when the modulated phase (ϕ_1 in this case) changes. In order to obtain a good intuition about the optimal increase in transmission we look at the average value.

$$\langle T_I \rangle = \langle \mid A_1 \mid^2 \rangle + \langle \mid A_R \mid^2 \rangle + \langle 2A_1 A_R \cos(\theta_{t1} + \phi_1 - \psi_R) \rangle. \tag{3.18}$$

Using eq. 3.14, the average value of $\mid A_1 \mid^2$ is given by:

$$\langle \mid A_1 \mid^2 \rangle = \langle \frac{1}{N} \mid \sum_{j=1}^{N} t_{j1} \mid^2 \rangle = \frac{1}{N} \langle \mid \sum_{j=1}^{N} t_{j1} \mid^2 \rangle. \tag{3.19}$$

In the same way, using eq. 3.16 the average value of $\mid A_R \mid^2$ is:

$$\begin{aligned} \langle \mid A_R \mid^2 \rangle &= \langle \mid \sum_{k\neq 1}^{N-1} A_k e^{i(\theta_{tk}+\phi_k)} \mid^2 \rangle = \langle \left(\sum_{k\neq 1}^{N-1} A_k e^{i(\theta_{tk}+\phi_k)} \right) \left(\sum_{k'\neq 1}^{N-1} A_{k'} e^{-i(\theta_{tk'}+\phi_{k'})} \right) \rangle \\ &= \langle \sum_{k=k'\neq 1}^{N-1} \mid A_k \mid^2 \rangle + \langle \sum_{k\neq k'\neq 2}^{N-1} A_k e^{i(\theta_{tk}+\phi_k)} A_{k'} e^{i(\theta_{tk'}+\phi_{k'})} \rangle. \end{aligned} \tag{3.20}$$

The last term of the summation averages to zero given that they are random complex numbers normally distributed around zero. In this way, using eq. 3.15, $\mid A_R \mid^2$ becomes:

$$\langle \mid A_R \mid^2 \rangle = \langle \sum_{k=k'\neq 1}^{N-1} \mid A_k \mid^2 \rangle = \langle \sum_{k\neq 1}^{N-1} \mid\mid \sum_{j=1}^{N} t_{jk} \mid \cdot \mid E_{Ik} \mid\mid^2 \rangle = \sum_{k\neq 1}^{N-1} \frac{1}{N} \langle \mid \sum_{j=1}^{N} t_{jk} \mid^2 \rangle = \frac{N-1}{N} \langle \mid \sum_{j=1}^{N} t_{jk} \mid^2 \rangle. \tag{3.21}$$

The average value of the interference term in eq. 3.18 can be split into the average of the cosine and the average of the amplitude, given that the two terms are independent from each other, so that:

$$\langle 2A_1 A_R \cos(\theta_{t1} + \phi_1 - \psi_R) \rangle = \langle 2A_1 A_R \rangle \langle \cos(\theta_{t1} + \phi_1 - \psi_R) \rangle. \tag{3.22}$$

From the definition of variance we know that: $Var[A_1 A_R] = \langle A_1^2 A_R^2 \rangle - \langle A_1 A_R \rangle^2$, so that $\langle A_1 A_R \rangle$ can be written as: $\langle A_1 A_R \rangle = \sqrt{\langle A_1^2 A_R^2 \rangle - Var[A_1 A_R]}$. Given that the variance of a distribution is always positive, in order to find a simplification for the calculus of $\langle A_1 A_R \rangle$ we use the inequality: $\langle A_1 A_R \rangle \leq \sqrt{\langle A_1^2 A_R^2 \rangle}$. The term $\langle A_1^2 A_R^2 \rangle$ is:

$$\langle A_1^2 A_R^2 \rangle = \langle \frac{1}{N} \mid \sum_{j=1}^{N} t_{j1} \mid^2 \left(\sum_{k=k'\neq 1}^{N-1} \mid A_k \mid^2 + \sum_{k\neq k'\neq 1}^{N-2} A_k e^{i(\theta_{tk}+\phi_k)} A'_k e^{i(\theta_{tk'}+\phi_{k'})} \right) \rangle,$$

thus

$$\langle A_1 A_R \rangle \leq \sqrt{\langle \frac{1}{N} \mid \sum_{j=1}^{N} t_{j1} \mid^2 \sum_{k=k'\neq 1}^{N-1} \mid A_k \mid^2 \rangle + \langle \frac{1}{N} \mid \sum_{j=1}^{N} t_{j1} \mid^2 \sum_{k\neq k'\neq 1}^{N-2} A_k e^{i(\theta_{tk}+\phi_k)} A'_k e^{i(\theta_{tk'}+\phi_{k'})} \rangle}. \tag{3.23}$$

The second term of the summation inside the square root averages to zero as in the previous case, given that it is the sum of random normally distributed variables centred around zero. This leads to a simplification in eq. 3.23, so that:

$$\begin{aligned}\langle A_1 A_R\rangle &\leq \sqrt{\langle \frac{1}{N} \mid \sum_{j=1}^{N} t_{j1} \mid^2 \sum_{k=k'\neq 1}^{N-1} \mid A_k \mid^2\rangle} = \sqrt{\frac{1}{N}\langle \mid \sum_{j=1}^{N} t_{j1} \mid^2\rangle \frac{N-1}{N}\langle \mid \sum_{j=1}^{N} t_{jk} \mid^2\rangle} \\ &= \frac{\sqrt{N-1}}{N}\langle \mid \sum_{j=1}^{N} t_{ji} \mid^2\rangle,\end{aligned} \tag{3.24}$$

where we have assumed that the average value of the sums of uncorrelated transmission matrix elements are equal, so we use the index i for a general term $\sum_{j=1}^{N} t_{ji}$. Next we look for the average value of the cosine. However this is not a regular average, due to the nature of the optimization. The value of the cosine will change only to maximize the interference term, meaning that it will not take negative values. The possible values we can obtain when optimizing are 0 if the channel addressed is already optimal or two times the amplitude of the cosine, in the case the phase of the channel addressed is minimal. In order to account for this, we will look at the average of the cosine when varying between 0 and 1 and multiply the result by two to account for the fact it can double the amplitude. In this way, the average of the cosine is:

$$\langle \cos(\theta_{t1} + \phi_1 - \psi_R)\rangle = 2\frac{1}{\pi/2 - 0}\int_0^{\pi/2} \cos(\theta_{t1} + \phi_1 - \psi_R) d\phi_1 = 2\frac{2}{\pi} = \frac{4}{\pi}. \tag{3.25}$$

Putting it all together, we have that the interference term due to the modulation of one channel is:

$$\langle T_I\rangle \leq \frac{1}{N}\langle \mid \sum_{j=1}^{N} t_{j1} \mid^2\rangle + \frac{N-1}{N}\langle \mid \sum_{j=1}^{N} t_{jk} \mid^2\rangle + \frac{8}{\pi}\frac{\sqrt{N-1}}{N}\langle \mid \sum_{j=1}^{N} t_{ji} \mid^2\rangle. \tag{3.26}$$

The optimized total transmitted intensity as a result of the optimization of the N channels is given by multiplying by N the interference term in equation 3.26:

$$\begin{aligned}\langle T_I^{OP}\rangle &\leq \frac{1}{N}\langle \mid \sum_{j=1}^{N} t_{j1} \mid^2\rangle + \frac{N-1}{N}\langle \mid \sum_{j=1}^{N} t_{jk} \mid^2\rangle + \frac{8}{\pi}\sqrt{N-1}\langle \mid \sum_{j=1}^{N} t_{ji} \mid^2\rangle \\ &= \langle \mid \sum_{j=1}^{N} t_{jk} \mid^2\rangle + \frac{8}{\pi}\sqrt{N-1}\langle \mid \sum_{j=1}^{N} t_{ji} \mid^2\rangle.\end{aligned} \tag{3.27}$$

In order to quantify the enhancement due to the optimization of each channel, we calculate the total transmitted intensity when no optimization is performed and look at the ratio, as we did when looking at the optimal focusing enhancement. The total field transmitted when no optimization is performed is given by:

$$T_F \mid_T = \sum_{k=1}^{N}\left(\sum_{j=1}^{N} t_{jk} E_{Ik}\right) = \sum_{k=1}^{N}\left(\mid \sum_{j=1}^{N} t_{jk} \mid\mid E_{Ik} \mid e^{i(\theta_{tk}+\phi_k)}\right) = \sum_{k=1}^{N}\left(A_k e^{i(\theta_{tk}+\phi_k)}\right), \tag{3.28}$$

therefore the non-optimized total intensity is given by:

$$T_I^{NO} = \left(\sum_{k=1}^{N} A_k e^{i(\theta_{tk}+\phi_k)}\right)\left(\sum_{k=1}^{N} A_k e^{-i(\theta_{tk}+\phi_k)}\right) = \sum_{k=k'=1}^{N} \mid A_k \mid^2 + \sum_{k\neq k'}^{N-1} A_k e^{i(\theta_{tk}+\phi_k)} A'_k e^{i(\theta_{tk'}+\phi_{k'})}, \tag{3.29}$$

thus the average intensity becomes:

$$\langle T_I^{NO}\rangle = \langle \sum_{k=k'=1}^{N} \mid A_k \mid^2\rangle + \langle \sum_{k\neq k'}^{N-1} A_k e^{i(\theta_{tk}+\phi_k)} A'_k e^{i(\theta_{tk'}+\phi_{k'})}\rangle. \tag{3.30}$$

Given that the second term in the sum averages to zero, the average non-optimized total transmission is:

$$\langle T_I^{NO}\rangle = \langle \sum_{k=k'=1}^{N} \mid A_k \mid^2\rangle = \langle \sum_{k=1}^{N} \mid\mid \sum_{j=1}^{N} t_{jk} \mid \cdot \mid E_{Ik} \mid\mid^2 = \sum_{k=1}^{N} \frac{1}{N} \langle \mid \sum_{j=1}^{N} t_{jk} \mid^2\rangle = \langle \mid \sum_{j=1}^{N} t_{jk} \mid^2\rangle. \tag{3.31}$$

The enhancement in the total transmitted intensity is then given by:

$$\langle \tilde{\eta}_T\rangle = \frac{\langle T_I^{OP}\rangle}{\langle T_I^{NO}\rangle} \leq \frac{\langle \mid \sum_{j=1}^{N} t_{jk} \mid^2\rangle + \frac{8}{\pi}\sqrt{N-1}\langle \mid \sum_{j=1}^{N} t_{ji} \mid^2\rangle}{\langle \mid \sum_{j=1}^{N} t_{jk} \mid^2\rangle} = 1 + \frac{8}{\pi}\sqrt{N-1}, \tag{3.32}$$

where the average in the elements of the transmission matrix can be simplified under the assumption that the elements are uncorrelated.

This result shows the optimal enhancement we can achieve when we consider the channels we address are completely uncorrelated. It is interesting to note the difference between the increase in total transmission and the increase in the focus intensity. We showed that the enhancement in total transmission scales with $\sqrt{N-1}$ whereas the enhancement in the focus intensity scaled linearly with N, as we showed in equation 3.9.

Numerical evaluation

We performed a numerical optimization that gives the optimal enhancement in transmission when the UTC model is considered[†]. We defined a transmission matrix with normally distributed elements. The incident field, as defined in eq. 3.12 with initial phase set equal zero in all the modes, except for the one that was being optimized, for simplicity. We added the fields given by the modulated mode and the rest, and evaluated the resulting intensity $|T_F\mid_{E_{I1}} + T_F\mid_{T-E_{I1}}\mid^2$.

In order to obtain the total optimized intensity due to the modulation of one mode (eq. 3.26) we calculated the differences in the intensity when choosing the right phase or the original phase, for each independent mode. After optimizing each different mode we added all of them (equivalent to the term $\frac{8}{\pi}\sqrt{N-1}\langle \mid \sum_{j=1}^{N} t_{ji} \mid^2\rangle$ in eq. 3.32). After adding and dividing by the total transmission, we obtain the normalized enhancement factor for the total transmission. We repeated the full

[†]The code used for this numerical simulation can be found on Appendix A.

optimization process 1100 times to obtain the average enhancement factor described in eq. 3.32.

Figure 3.2 shows the numerical results of the enhancement in total transmission as a function of the number of degrees of freedom N. The black solid line is a fit to the data in the form $1+\alpha\sqrt{N-1}$ where α is the fit parameter, in this case $\alpha = 2.95$. The green solid line shows a fit to the data in the form $1+\beta(N-1)$ with β the fit parameter, with $\beta = 0.09$ in the graph. The dots in the graph represent the average value of the enhancements achieved in the 1100 realizations. The error bars represent the standard deviation of the values in the enhancement factor. If the enhancement in total transmission had the same scaling as the focusing enhancement, it should follow the green curve. It is clear from the graph that total transmission fits to the $1+\alpha\sqrt{N-1}$ curve, in very good agreement with equation 3.32.

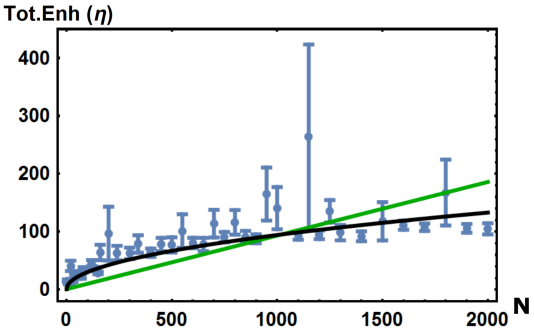

FIGURE 3.2: Numerical data showing the dependance of the enhancement in total transmission with the number of channels N. The black solid line is a curve following $1+\alpha\sqrt{N-1}$ where α is an adjustable parameter, and the green curve shows how the total transmission should increase if it was linear in N-1, that it is clearly off from the numerical data points.

Distribution of the enhancement in total transmission

As we showed for the case of optimal focusing, the optimal total transmission also follows a distribution. The distribution of the total transmission comes from the distribution of the interference term, which is the one leading to the increase in transmission. As we saw from equation 3.17 the interference term is the result of the product of two normally distributed terms, each of them with different mean and standard deviation values. Figure 3.3 shows the distribution of the total transmission for different number of degrees of freedom N. Each curve represents the histogram obtained out of 1100 total transmission optimizations. The histograms are not normalized, in order to enhance visibility they have been enlarged to have a maximal value of 1.

As shown in Fig. 3.3 for small number of N the distribution is asymmetric and shifted to the left. As the number of degrees of freedom N becomes larger, the distribution becomes more symmetric, as expected from the Central Limit Theorem.

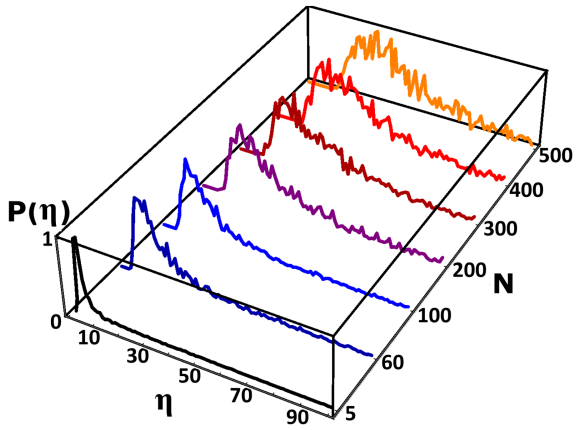

FIGURE 3.3: Numerical data showing the distribution of the enhancement factor ($P(\eta)$) of total transmission as the number of degrees of freedom N becomes larger.

3.2 Imperfect wavefront control

So far we have been looking at ideal enhancements assuming perfect phase modulation. In practice, this control gets reduced by several factors like the number of segments available to control in the spatial light modulator, individual control of phase or amplitude, etc. All these experimental imperfections can be captured by the factor γ, which is the scalar product between the ideal required optimal field $\tilde{E}_a$ and E_a, the experimentally synthesized field:[27]

$$\gamma = \sum_{a=1}^{N} \frac{\tilde{E}_a \cdot E_a^*}{\sqrt{\tilde{I}I}}. \tag{3.33}$$

where $\tilde{I}$ and I are the ideal and non-ideal intensities, respectively. Given that γ is defined as the scalar product of the ideal field and the synthesized one, we know that we can write the synthesized one as the its projection over the ideal one and an error term, so that:

$$E_a = \cos(\theta)\tilde{E}_a + \sqrt{1-\cos^2(\theta)}\Delta E_a, \tag{3.34}$$

where in our case $\cos(\theta) = \gamma$. The experimental synthesized field can then be written as:

$$E_a = \gamma\tilde{E}_a + \sqrt{1-\mid\gamma\mid^2}\Delta E_a. \tag{3.35}$$

where ΔE_a is an error contribution, by definition orthogonal to $\tilde{E}_a$. $\mid\gamma\mid^2$ is known as the fidelity factor.

Given that $\mid\gamma\mid^2 \leq 1$ this result shows the effect in the enhanced intensity under experimental conditions. If the fidelity factor is known it is then possible to obtain an estimate of the realistic optimal enhancement factor one can achieve. Given that the enhancement in total transmission and maximal focusing have a different dependency with N, we expect a different dependency for

the fidelity factor as well.

3.2.1 Focusing enhancement factor under imperfect modulation

Using equation 3.35 and substituting it into eq. 3.9, the average experimental enhancement factor becomes:

$$\langle \eta \rangle = \langle \mid \gamma \mid^2 \rangle \langle \tilde{\eta} \rangle + (1 - \langle \mid \gamma \mid^2 \rangle) \approx \langle \mid \gamma \mid^2 \rangle N \quad \text{when} \quad N >> 1, \tag{3.36}$$

so, the total enhancement is linear to the average value of the enhancement factor.

3.2.2 Total transmission enhancement under imperfect modulation

Given that the γ factor only affects to the term that has been actively modulated, as we saw in eq. 3.33, when calculating the enhancement in total transmission it should only be added to the interference term, which is the one we are actively modulating. That is, from equation 3.18, it should only affect the last term ($\langle 2A_1 A_R \cos(\theta_{t1} + \phi_1 - \psi_R) \rangle$), given that the rest cancel out when normalized (eq. 3.18).

Given that the actively modulated field is $A_1 e^{\phi_1}$, γ only affects this term. Following equation 3.35, we have that:

$$A_1^2 A_R^2 = \mid \sum t_{j1} \gamma \tilde{E_1} \mid^2 \cdot \mid \sum_{k \neq 1}^{N-1} (\sum t_{jk} E_k) \mid^2 . \tag{3.37}$$

Following the same procedure given in eq. 3.24 we obtain:

$$\langle A_1 A_R \rangle \leq \sqrt{\langle \mid \gamma \mid^2 \rangle} \frac{\sqrt{N-1}}{N} \langle \mid \sum_{k \neq 1}^{N} t_{jk} \mid^2 \rangle \tag{3.38}$$

resulting in an total transmission enhancement:

$$\langle \eta_T \rangle \leq 1 + \sqrt{\langle \mid \gamma \mid^2 \rangle} \frac{8}{\pi} \sqrt{N-1}. \tag{3.39}$$

In this case, we see how the enhancement in total transmission also scales with the square root of the fidelity factor, instead of linearly as for the focusing enhancement.

Main contributions to the fidelity factor

The fidelity factor is the combination of different independent experimental contributions.[27,44] Conditions such as phase-only modulation or temporal decorrelation of the sample are responsible for the reduction of the ideal value of the enhancement factor derived in equations 3.9 and 3.32. In table 3.1 we identify the more important contributions to the total fidelity factor. If the reader is interested in detailed derivations, Vellekoop's or van Putten's thesis are excellent references.[44,68]

The total fidelity factor is given by the product of all the different and independent contributions:

$$\mid \gamma \mid^2 = \mid \gamma_{cont} \mid^2 \cdot \mid \gamma_{ph} \mid^2 \cdot \mid \gamma_t \mid^2 \cdot \mid \gamma_{lee} \mid^2 \cdot \mid \gamma_{amp} \mid^2 \cdot \mid \gamma_{pol} \mid^2 . \tag{3.40}$$

In Chapter 4 we study the case in which speckle illumination is sent to the spatial light modulator and we detail how such a patterned illumination contributes to the fidelity factor.

3.3 Summary

In this chapter we have studied the ideal wavefront optimizations when focusing the light to a speckle spot, to be used in Chapter 4. We have studied for the first time at the distribution of its enhancement factor, showing that the optimal enhancement that can be achieved is not indeed a fixed number, but if follows a distribution that can lead to significant variations in the measurements. We have derived the optimal total transmission through a scattering material under ideal phase wavefront modulation although considering an experimental approach with the step-wise algorithm, along with its probability distribution, verified numerically. Although this derivation is not exact and only give us an upper limit on the increase in total transmission, it provides us with a useful tool to estimate the possible increase in total transmission when full access to the open channels is not possible due to reduced wavefront control.[46] In the final part we study how imperfections in the wavefront modulation effect the ideal enhancements and how these should be taken into account.

SOURCE OF IMPERFECTION	CONTRIBUTION
Controlled degrees of freedom[44,68]: accounts for the difference between degrees of freedom of the sample and the ones we can control with the SLM	$\mid \gamma_{cont} \mid^2 = \frac{N_C}{N}$ N_C : controlled degrees of freedom
Phase-only modulation[14]: accounts for the case when only phase is being modulated from the SLM	$\mid \gamma_{ph} \mid^2 \approx \frac{\pi}{4}$
Binary amplitude modulation[15]: : accounts for the case when only amplitude is being modulated from the SLM	$\mid \gamma_{ba} \mid^2 \approx \frac{1}{2\pi}$
Temporal decorrelation: account for the change in time of the sample or the system temporal instabilities	$\mid \gamma_t \mid^2 = \frac{\tau_S}{\tau_{op}}$ τ_S: time it takes the sample to change (due to heat, vibrations, ...) leading to a decorrelated speckle pattern τ_{op}: time of the wavefront optimization.
Discrete phase modulation[70]: takes into account the mistakes can be made by discretizing the steps in the synthesized phase	$\mid \gamma_{lee} \mid^2 = \left(\frac{sin(\pi/N_{st})}{\pi/N_{st}}\right)^2$ N_{st} : number of phase steps
Non-uniform illumination[44]: takes into account the case where the SLM is not illuminated homogeneously	$\mid \gamma_{amp} \mid^2 = \frac{\overline{A_a}^2}{\overline{A_a^2}}$ $A_a = 1 + \frac{\delta A_a}{\lvert E_a^{id} \rvert}$: amplitude error of the field in channel a. The overline is a spatial average
Single polarization control: accounts for the case where only one polarization is being modulated by the SLM	$\mid \gamma_{pol} \mid^2 = \frac{N_p^C}{N_p^C + N_p^{NC}}$ N_p^C, N_p^{NC} : Modes of the controlled and not-controlled polarizations, respectively

TABLE 3.1: Contributions to the fidelity factor arising from different and independent sources

Chapter 4

Improving beam quality by wavefront shaping of speckle patterns

In this chapter we study the implications of manipulating a completely randomized beam using wavefront shaping, a technique that has been well studied assuming plane wave illumination as starting point in the wavefront modulator. Then we use this approach to improve the beam quality of the output of a multimode fiber, converting it to a diffraction limited Gaussian beam, on average with 300 times more energy than conventional spatial filtering. This approach has the potential to be used with poor beam quality lasers, originated by the multimode lasing operation. All the results presented in this chapter are my own work.

4.1 Introduction

The fabrication of high power lasers with single mode operation (or high beam quality) are of great interest, having a wide range of applications, such as high energy density physics, laser printing, biomedical imaging, etc.[71–73] However the combination of high power and good beam quality is very challenging and in general, the easiest way to obtain a high power laser is by allowing multiple transversal modes to be amplified in the gain medium,[72,74] which results in a multimode beam with poor beam quality. The origin of the poor beam quality is the random interference of the multiple modes being amplified, that results in a random intensity speckle pattern at the output. This is comparable to the random interference of modes in multimode fibers, where the different modes travelling at different speeds end up in a random interference, resulting in a speckle pattern at the output.

Traditional solutions to improve the beam quality of multimode lasers are based on spatial filtering of the output beam, e.g. placing a pinhole or single mode fiber to filter one spot of the

speckle pattern. Other more sophisticated solutions are based on bend-induced losses to the modes different from the fundamental and gain filtering,[75,76] however all these approaches are highly energy inefficient and negate the power gained by employing multimode lasers.

It was shown that wavefront shaping techniques can focus most of the light to a diffraction limited spot at one end of the fiber (therefore making the beam quality optimal) if at the wavefront incident on the scattering system can be manipulated by an SLM.[77–79] Although this has useful applications, this approach is not suitable when we only have access to the already randomized or speckled beam. The manipulation of a partially randomized wavefront is not novel though, and it has been shown to be very useful to reduce imaging aberrations[80] or focus light to a diffraction limited spot.[81] However, when the wavefront is completely randomized, e.g. large variation in the length scale of $\lambda/2$,[80,82] as at the output of a highly multimode laser, the efficiency of wavefront shaping to transform the speckle pattern to a diffraction limited spot is not well studied, only done in passing.[25]

In this experiment we study the implications of using wavefront shaping techniques to modify a speckle pattern illumination. Then we experimentally shape the wavefront of a speckled beam and transform it into a diffraction limited Gaussian beam. As a proof of concept experiment, for simplicity and experimental convenience we perform the study using the speckle pattern generated at the output of a multimode fiber instead of a multimode laser, although this approach can be very well extrapolated to temporally coherent multimode lasers with static speckle patterns as output beam (e.g. high power VCSEL lasers[74]).

4.2 Random interference from a multimode optical fiber and beam quality

In this section we present a brief background to understand the origin of the random interference pattern observed at the output of a multimode fiber when coherent light travels through it.

Optical fibers are broadly classified into two types: single mode and multimode fibers, depending on the number of propagating modes they support. In single mode fibers only one mode can propagate and the output is given by the shape of this mode, a diffraction limited Gaussian beam in conventional fibers. Multimode optical fibers are, in simple terms, large core fibers supporting several propagating modes. The total number of propagating modes in a multimode fiber, N_f depends on its normalized frequency V (or V-parameter), containing the useful parameters of the fiber, such that:[4,83]

$$N_f \approx \frac{V^2}{2} \qquad \text{and} \qquad V \approx \frac{2\pi}{\lambda_0}(NA)a \tag{4.1}$$

where λ_0 is the source wavelength in vacuum, NA is the numerical aperture of the fiber and a is the core radius, in the case of a step index fiber[†].

In order to gain an intuitive and reasonably accurate understanding of mode propagation in optical fibers, we rely on geometrical ray optics. From this perspective, each propagating mode can be treated as a ray travelling with a given angle.[42,83] Depending on the angles the rays are propagating with, they travel different distances, given by: $d = \frac{L/\cos(\theta)}{c/n_1}$, as shown in the schematic on Fig. 4.1a, where L is the length of the fiber, θ the angle of the propagating ray with the horizontal axis, and c/n_1 the speed of light in the medium. Given that all rays travel at the same speed, different angles lead to different delays in leaving the medium, resulting in different phase delays. If the phase delays between different modes are larger than 2π and the source is coherent, all the different modes will interfere randomly, creating a speckle pattern at the output,[42] as shown in Fig. 4.1b.

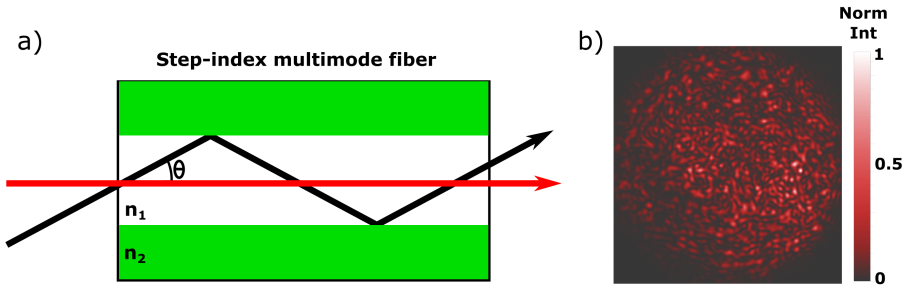

FIGURE 4.1: a) Schematic of a step-index multimode fiber where the red and black arrows represent propagating rays at different angles. b) Typical speckle pattern generated at the output of a multimode fiber when coherent light is propagated.

4.2.1 Beam quality

The quality of a laser beam is a term used to characterize how tight we can focus the laser. A standard way of quantifying the beam quality is the M^2 beam quality factor.[84] This factor is defined as the beam parameter product (product of the beam radius at the focus waist (ω_0) and the far-field divergence angle of the beam Θ), divided by λ/π (beam parameter product of a diffraction-limited Gaussian beam with the same wavelength):

$$M^2 = \frac{\pi\omega_0\Theta}{\lambda}. \tag{4.2}$$

The optimal beam quality factor M^2 is achieved by a diffraction limited Gaussian beam, resulting in $M^2 = 1$. At the focus of a diffraction limited spot the wavefront is flat, therefore any distortion that deteriorate the flatness of the wavefront, such as the random interference resulting from the multimode fibers, make the beam quality worse, and consequently the M^2 factor larger.

[†]We use the definition of the V-parameter for step index fibers because that is the kind of fibers we use in the experiment presented in this chapter.

4.3 Effect of speckle pattern illumination on focusing enhancement

In Chapter 3 we investigated the optimal focusing enhancement that can be achieved assuming ideal modulation. In order to obtain the optimal enhancement (see Section 3.1.1), we assumed we could implement any desired wavefront, and the optimal was given by the Cauchy-Schwartz inequality. Then, in order to account for imperfections in the modulation, we defined the fidelity factor, that takes into account if we can only modulate the phase or amplitude, controlled modes in the sample, etc. An important assumption underlying all this derivation was that in the experiment you can start from a plane wave to which you can in principle modulate the phase and amplitude. However, if the illumination of our wavefront modulator is a speckle pattern, the starting point will be an inhomogeneous intensity, as shown in Fig. 4.2a) which restricts importantly the options of modulation and makes the ideal focusing derivation not obviously valid in this case.

Although naively one could think the two cases are equivalent, there are indeed important differences: a speckle pattern has naturally mixed polarizations and inhomogeneous spatial intensity and phase. When different modes propagate through a fiber, the original polarization is scrambled and it results in a pattern where both orthogonal polarizations are present. Given that wavefront shaping is based on modifying the interference and different polarizations interfere independently, only one polarization can be actively controlled at a time. If we only control one polarization, the total controllable degrees of freedom is reduced by half (if both polarizations are equally present) from the beginning.

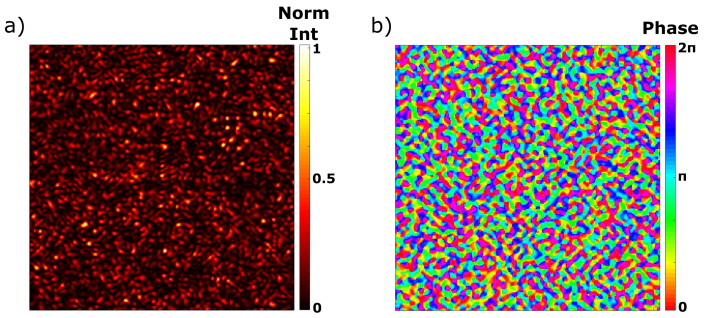

FIGURE 4.2: a) Simulated intensity speckle pattern. b) Phase pattern of the speckle in panel a)

The second important difference comes from the spatial inhomogeneities in phase and intensity of the speckle pattern, as seen in Fig. 4.2. In the regions where the phase is not well defined (phase vortices), the intensity of the pattern is zero. Obviously the SLM cannot act over these regions, given they have zero intensity, which reduces even more the degrees of freedom the SLM can control. The condition for the optimal focusing enhancement (equality on the Cauchy Schwartz condition in eq. 3.3) is that the modulated wavefront $\tilde{E}_i \propto t_{fi}^*$ which imposes

that $\mid \tilde{E}_i \mid = \mid t_{fi} \mid$ and $Arg[\tilde{E}_i] = Arg[t_{fi}^*]$. When speckle illumination is used, there will be regions where the intensity cannot match the required one (regions where intensity is zero, given that it can not be increased by the SLM). If either the amplitude or the phase can not perfectly match for all channels i in either the amplitude or phase, the equality is not fulfilled, which decreases the optimal enhancement factor.[‡]

Deriving from scratch the ideal enhancement that can be achieved under speckle illumination is not straightforward, given that now we can not use the Cauchy-Swartz inequality, as done in Section 3.1.1. As an alternative, we attempt to account for the speckle illumination in the fidelity factor (see Section 3.2 for details). As mentioned before, the consequences of speckle illumination was the reduced control due to the mixture of polarization and intensity inhomogeneity. The contribution to the fidelity factor from the polarization depends on the fraction of light in each of the polarizations. If we assume that both polarizations are equally present[§], we obtain:

$$\mid \gamma_{pol} \mid^2 = \frac{1}{2}. \tag{4.3}$$

We can account for the effect of the inhomogeneous intensity by using:

$$\mid \gamma_a \mid^2 = \frac{\overline{A_i}^2}{\overline{A_i^2}}, \tag{4.4}$$

where $A_i = 1 + \frac{\delta A_i}{|\tilde{E}_i|}$ is the variation in amplitude of the field over different incident channels and the over-line represents the spatial average. In particular, when contrasted speckle (coherent and initially polarized source) is the source of illumination, the fidelity factor becomes: $\mid \gamma_a \mid^2 \approx \frac{1}{2}$, so reducing by half the possible enhancements we could achieve with a plane wavefront.

In summary, the influence of using speckle pattern as the source of illumination, results in a fidelity factor of: $\mid \gamma_a \mid^2 \cdot \mid \gamma_{pol} \mid^2 \approx 1/4$. However, it is important to note that this is an approximation, a full new derivation would be necessary to rigorously obtain the optimal focusing enhancement of a speckle pattern.

4.4 Experimental results

In this section we present an experiment in which we use wavefront shaping techniques to improving the beam quality at the output of a multimode fiber, when only access to the random speckle pattern is available. A schematic of the experimental apparatus is shown in Fig 4.3. The laser source used was a He-Ne laser (632.8 nm) coupled to a multimode fiber ($a = 275\,\mu m$, $NA = 0.22$).

[‡] In Appendix A there is a simple code verifying that when the amplitude condition is not fulfilled, although the condition in the phase might be maintained ($Arg[\tilde{E}_i] = Arg[t_{fi}^*]$), the average focusing enhancement drops by roughly 1/2.

[§] This is true in our experiments, and most cases where speckle is generated, being a notable exception the speckle pattern generated by single scattering in diffusers.

At the output of the multimode fiber the random interference of the propagating modes generate a high contrast speckle pattern. The beam was then collimated by a 400 mm focal length lens and sent to a SLM to shape the wavefront. The focal length of the lens and the distance from the fiber to the lens was chosen so that the collimated speckle pattern had the speckle spots of the size of the phase pixels (or macropixels) on the DMD, that was 129.6 $\times$ 129.6 µm.[‡] A second lens of 750 mm focal length collected the modulated beam and focused it to its focal plane. We used a pinhole at the focal plane, of a size slightly larger than a speckle spot (100 µm in diameter), to filter out a diffraction-limited spot (or speckle spot). Using a photodiode behind the pinhole (to gain speed) we optimized the intensity passing through in it. That intensity was then used as feedback for the algorithm controlling the SLM. We could have used a CCD camera as feedback element, instead of the pinhole with the photodiode, however we decided to use the latter to gain speed in the optimization.

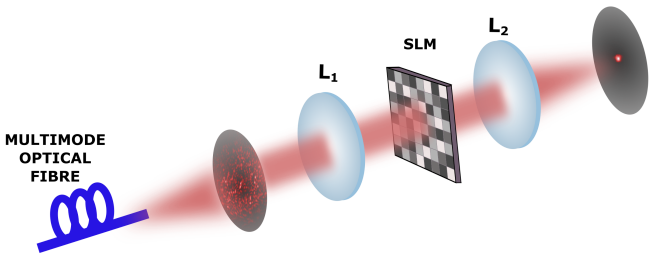

FIGURE 4.3: Schematic of the experimental setup used to improve the beam quality of a multimode beam by wavefront shaping techniques. The output of the multimode fiber is collimated and sent to the SLM, where an algorithm changes the phase of the wavefront in order to compensate for the random scattering of the modes in the fiber. An iterative algorithm evaluates the phase compensation needed by the SLM, in order to deposit the maximal energy into a diffraction limited spot.

4.4.1 Results: beam quality and total intensity measurements

In Fig. 4.4 we show the images of the beam waist at the focal length of the second lens (L_2 in the set-up schematic), when the beam is not optimized (panel a), when it has been spatially filtered by a single mode fiber (panel b), pinhole (panel c) and when it has been optimized through the pinhole. In order to evaluate the beam quality of this and subsequent beams, we use the standardized beam quality factor M^2, as described in Section 4.2.1, which compares any beam with an ideal Gaussian diffraction-limited beam.[84]

[‡]As we discussed in Chapter 2, given that different speckle spots are (to a very good approximation) independent from each other, the most efficient manipulation will happen when we control them also independently.

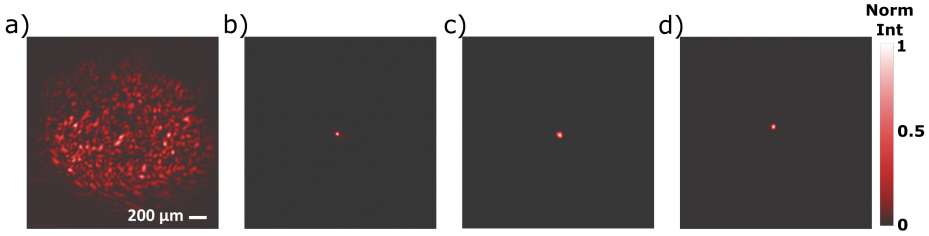

FIGURE 4.4: Images of the beam waists at the focal plane of a $750mm$ lens under different configurations. a) Beam waist of the output from the multimode optical fiber, showing the speckle pattern of the beam. The beam quality factor is $M^2 = 59 \pm 5$. b) Beam waist of the output of a single mode fiber. The beam quality factor in this case is 1.4 ± 0.4 and the intensity deposited is $\approx 0.5\%$ of the total intensity in the multimode beam. c) Beam waist of a filtered speckle spot using a 100μ diameter pinhole. The beam quality factor in this case is 1.5 ± 0.3. The intensity deposited is $\approx 0.5\%$ of the total intensity in the multimode beam.d) This picture shows the beam filtered through the pinhole after the completion of the wavefront shaping optimization. The beam quality factor in this case is 1.2 ± 0.3. The intensity deposited is $\approx 25\%$ of the total intensity in the multimode beam.

The beam waist at the output of the multimode fiber (Fig. 4.4a) shows a speckle pattern with a large number of diffraction limited spots ($N \approx 2000$). This results in a poor beam quality, with an M^2 factor equal to 59 ± 5. If we couple the beam to a single mode fiber, we can readily obtain a diffraction-limited spot at the beam waist (Fig. 4.4b). In this case $M^2 = 1.4 \pm 0.4$, which is very close to the ideal value of 1 for an ideal diffraction limited Gaussian beam. However the energy conversion from a multimode output to a single mode one is very energy inefficient, coupled power was less than 0.5% in our experiments. Another equivalent and conventional solution is to use a pinhole to spatially filter a single spot from the multimode pattern in Fig. 4.4a. The spatially filtered beam is shown in Fig. 4.4c, and although the beam quality is again improved, holding a value of $M^2 = 1.5 \pm 0.3$, the energy efficiency is reduced to less than 0.5%. In Fig. 4.4d we show the result of using wavefront shaping techniques to increase the intensity deposited into the chosen diffraction limited spot. In this experiment we achieved focusing enhancement factors of 300 ± 13, i.e. the intensity in the optimized spot became 300 times larger than the average intensity of any spot in the multimode beam (Fig. 4.4a). An immediate consequence of this is the improvement of the M^2 factor from 59 ± 5 to 1.2 ± 0.3 for the optimized spot.[¶]

In Fig.4.5 we show the increase in the intensity deposited in the optimized diffraction-limited spot as the algorithm progresses. The power of the filtered mode is normalized by the total power of the unoptimized multimode beam (shown in Fig. 4.4a). From this graph we can see that the power deposited in the optimized mode goes from an initial value of the total intensity smaller than 0.5% (when considering a simple pinhole filtering) to a value of $24 \pm 1\%$ of the total intensity, achieved when the transmission through the pinhole is optimized.

To conclude, we compare the experimental focusing enhancement factor obtained with the expected one, given by eq. 3.36 that accounts for the experimental conditions in the fidelity factor $\mid \gamma \mid^2$. The total number of degrees of freedom in this case is given approximately by the number

[¶]This experiment was performed 13 times. The uncertainty in the enhancement factor is given primarily by the different values obtained in the different measurements. The uncertainty in the beam quality is dominated by the uncertainty in the measurement of the beam diameter, for which the camera had few pixels to resolve. This measurement could be improved using other methods to measure the diameter, such as knife edge measurements.

of speckle spots in the multimode output $N \approx 2000$. Given that the illumination beam on the SLM is a speckle pattern, if we take into account the amplitude inhomogeneity and single polarization control, as discussed in Section 4.3 we have a contribution to the fidelity factor of $\mid \gamma_{speckle} \mid^2 \sim 1/4$[¶]. This limits our maximal enhancement factor to $\approxeq 500$. Other experimental factors also have to be included, such as phase-only modulation ($\mid \gamma_{ph} \mid^2 \approx \pi/4$), temporal decorrelation ($\mid \gamma_t \mid^2 \approx 0.9$) and discrete phase modulation ($\mid \gamma_{lee} \mid^2 \approx 0.98$). All these factors account for imperfections in the wavefront modulation, which result in an expected enhancement factor $\eta = \tilde{\eta} \mid \gamma \mid^2 \approx 340$. This value is in good agreement with our experimental results (300 ± 13). This shows that even though the approach followed to estimate the optimal enhancement factor and the influence of speckle illumination was not rigorously correct (as discussed in Section 4.3), it is still a useful theoretical framework even when speckle patterns are used as illumination.

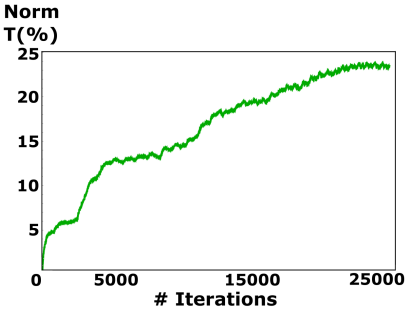

FIGURE 4.5: Total intensity transmitted through the pinhole as the optimization algorithm evolves. We can see the increase in transmission stagnates at approximately 24% after 24500 iterations.

4.5 Summary and outlook

In this chapter we have discussed the effect of having speckle patterns rather than plane waves as illumination for the efficiency of wavefront shaping techniques. We have seen that even though the current theoretical framework cannot be rigorously applied to the case of speckle illumination, it is possible to give a very good estimate of the expected experimental focusing enhancement. We have also discussed the problem that multimode lasers have with the output beam quality, and demonstrated that wavefront shaping techniques are capable of improving the spatial filtering of the beam while maintaining around 300 times more intensity than when no optimization is done, with a total optimized intensity of 24%. This opens new opportunities to use wavefront correction techniques as an added component at the output of multimode lasers, as long as they are coherent in time. This correction might be done with an SLM or it might also be in the form of an incorporated phase mask at the output.

[¶] In our experiment both polarizations are roughly equally present in the speckle pattern, so $\mid \gamma_{pol} \mid^2 \sim 1/2$, therefore leading to $\mid \gamma_{speckle} \mid^2 \sim 1/4$

Chapter 5

Enhanced deep detection of Raman scattered light by wavefront shaping

The work presented in this chapter is the result of a collaboration with Prof. Nick Stone and Dr. Adrian Ghita from the Biomedical Physics Group at the University of Exeter and our group lead by Dr. Jacopo Bertolotti. I did all the numerical calculations presented in the chapter, as well as the proof of concept experiment presented in Section 5.2. I performed the main experiment and improved the algorithm for the wavefront optimization with the help of Dr. Tom Vettenburg. The guidance and help of Dr. Adrian Ghita was particularly useful in the part involving the measurement of the Raman signal, as well as in the post-analysis.

The final goal of the experiment presented in this chapter is to enhance the optical detection of tumours (or other elements) embedded in biological tissue (such as human breast) using wavefront shaping techniques. As a first step, in this experiment we aim to improve the detection of elements hidden behind a highly scattering medium. The approach we use to detect the hidden element (and future detection of tumours) is based on studying the Raman inelastic scattered light, that provides a unique fingerprint of the chemical composition of the illuminated element (as detailed in Section 5.1). In order to improve the detection of the Raman signal of elements deep inside the medium, we increase the the light transmitted through the medium (equivalent to increase the penetration depth of the incident light, as we will see later in Section 5.6), using wavefront shaping techniques. Given that we use a fast Digital Micromirror Device (23.1 kHz refresh rate), this approach could potentially be used for almost real-time optimizations, given that biological tissue can be considered static for a few tens of milliseconds.[60,61]

We first introduce Raman spectroscopy, its advantages and the main limitation, that comes from a reduced penetration depth of the pump (or incident illumination). We then present the potential of wavefront shaping techniques to increase the penetration depth. Next we introduce a

numerical study to show the changes in the distribution of light inside the medium when the wavefront is (or is not) optimized, and its consequences for the Raman light detection. We then present the experiment and the experimental results, where we show the capability of increasing the intensity inside by almost 50%. In the final section we make an estimate of the extra penetration depth that the increase in pump intensity inside the medium would generate.

5.1 Introduction to Raman spectroscopy

Raman spectroscopy is an optical technique capable of identifying the chemical composition of the material that is being illuminated, via the analysis of the spectrum of the Raman inelastically scattered light. Although the light incident on a material is mostly elastically scattered, a small fraction of it (around 10^{-3} in gases to 10^{-6} in solids[85]) is inelastically scattered by the molecules of the material. In the semi-classical theory of scattering, under the dipole approximation (light wavelength much larger than the dimension of an atom) in the elastic scattering, a molecular system is on a fixed quantum state and the scattering is due to the periodic deformation of the state, caused by the electric field of the incident light. On the other hand, inelastic Raman scattering is associated with a quantum transition in the system. If the incident field excites the molecule with frequency ω and it causes the molecular system to go from an initial quantum state to a different one, that energy difference is compensated by a frequency change in the outgoing scattered photon $\omega \pm \Delta\omega$.[†] In this way, the inelastically scattered light has a spectrum different from the incident one, that is unique to any different chemical composition. The study of the spectrum of the Raman scattered light provides a unique way of identifying the molecules and chemicals of the illuminated element, which is very useful in imaging[88–90] and in sensing, e.g. to distinguish between cancerous or benign tumours in medical diagnosis.[9,91–94] In this work we are particularly interested in the sensing application of Raman spectroscopy. For sensing, the main limitation arises from the diffusive transport of light in scattering media, that makes the intensity decay roughly linearly with the depth, as discussed in Section 1.1 and represented in Fig.1.1. If the tumour or chemical to be detected is deep inside the medium, there will be very little intensity reaching it, and therefore the Raman scattered light (proportional to the pump intensity[‡]) will be very weak or even undetectable. Naively one might think we could solve that problem by increasing the intensity of the pump, to consequently increase the intensity inside. However this approach is not always valid, given that one might damage the illuminated tissues, overheating them.[95–97] As a consequence, Raman spectroscopic techniques are usually restricted to work near the surface of the material.[9,94,98] In this work we show that wavefront shaping techniques can significantly increase the intensity delivery inside the scattering material by just modifying the phase of the incident

[†] A full explanation of the semi-classical theory on Rayleigh and Raman scattering can be found in the literature.[86,87]
[‡] We study spontaneous Raman scattered light which is linear with the pump intensity[90]

wavefront, mitigating the problem of penetration depth of the pump light and avoiding the need to increase the pump power.

5.2 Increase of the transmitted intensity by wavefront shaping

When light impinges onto a medium with different refractive index, part of the energy is reflected, and the rest, transmitted (assuming a non-absorbing medium). Energy conservation tells us that: $R + T = I_0$, where I_0 is the initial intensity. If we want to illuminate a target embedded inside the medium, all the light that is being reflected is not useful for this purpose. In principle, one would like to reduce or eliminate the fraction of light reflected in these cases and increase the transmitted one, but this is not possible to do with conventional techniques.

With the development of wavefront shaping techniques, it was shown that it is possible to increase the transmission of light through a scattering material.[26,27,54] A schematic to show this idea is shown in Fig. 5.1, where panel a) shows the case where the incident beam is not optimized and a large fraction of light is being reflected, and panel b) the situation in which the wavefront has been modified to maximize transmission. In principle, in a wave-guide geometry it is possible to transmit all the incident light by coupling to the open channels of the sample[‡], however, in scattering media with slab geometry, limited control of the wavefront from the SLMs and imperfections in the modulation reduce considerably the efficiency of these techniques, as discussed in Sections 1.3 and 3.1.2.

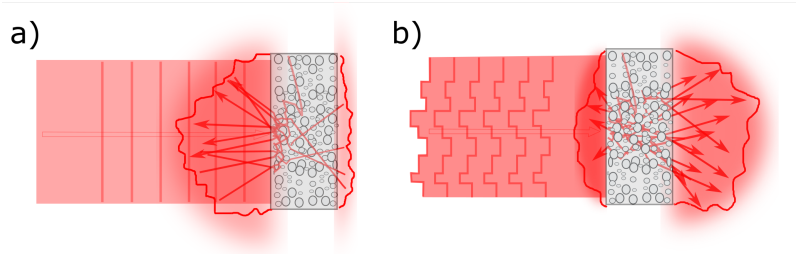

FIGURE 5.1: Schematic showing the amount of light reflected and transmitted when the wavefront incident on the material is not optimized (left) and when it is optimized to increase transmission through it (right).

As a proof of concept, to know how much we could increase the transmission in our experimental conditions, we designed an experiment in which we used a scattering sample of TiO_2 (of thickness $8 \pm 3\,\mu m$) and designed an algorithm to increase the total transmission through it. In Figure 5.2 we show the results of this experiment, where we can see the increase in transmission as the algorithm evolves, and at the same time, the decrease in the reflected intensity as dictated by energy conservation. In order to fully understand the plots in Fig. 5.2 it is important

[‡]The description of open and closed channels is in Section 1.3

to note that, to a very good approximation we were collecting the total transmission[§] but not the total reflection, only around 70% of it, due to the numerical aperture ($NA = 0.9$) of the collection microscope objective. Given that we do not know the reflection properties of our sample, it is not possible to determine exactly the total reflection when only a fraction of it is retrieved. However, it is clear from the data that there is a considerable drop in the reflected light as the transmitted increases by a factor 2.3.

In this experiment we are not coupling all the light to open channels of the sample. First of all because in a slab geometry they are not well defined (as discussed in Section 1.3), second, because although the total transmission is 2.3 times larger, we are not achieving total transmission of 100%, as shown in the vertical axis of Fig.5.2a). As we have already discussed, there are simulations[45] showing the existence of open channels for scattering slabs of small thicknesses, as well as experiments that show the possibility to couple more light to these open channels.[26–28,54] Given that we are able to increase the total transmission by a considerable amount (obtaining similar and in some cases larger increases in total transmission than the cited examples in the literature), we claim we are depositing as well more intensity into the open channels of our sample, which results in the increase of the total transmission.

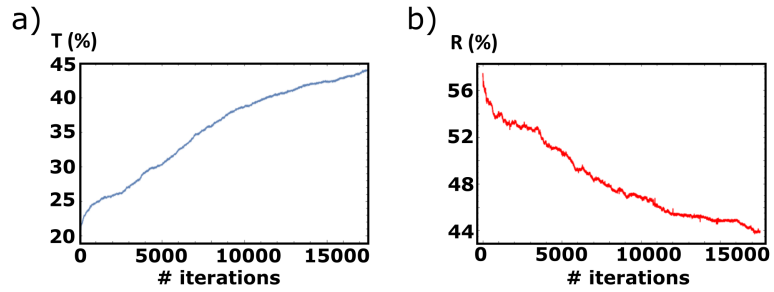

FIGURE 5.2: Experimental results showing the increase in total transmission through a scattering material (a) as reflection is decreasing (b), as the algorithm evolves.

A very interesting property of open channels is that they have a symmetric energy distribution inside the medium.[45,69] This implies that when optimizing the total transmission through a scattering medium, given that we distribute more light to open channels, we are indeed modifying the energy distribution inside, going from the originally diffusive intensity distribution (represented in Fig.1.1) to a symmetric one, peaked at the centre of the sample.[28,45,69] This difference in the energy distribution can be very useful to deposit more light at deeper positions within the sample and therefore increase the penetration depth inside.

[§]We can assume total transmission was collected, given that the photo-diode was around 150μm away from the sample and its collection area was much larger than the output spot (photo-diode diameter is 9.8 mm and the diameter of the output illuminated spot $\leq$ 100μm)

5.3 Energy density distribution of optimized and non-optimized wavefronts

As we mentioned in the introduction of this chapter, the main limitation to detect the Raman signal from elements embedded deep in scattering media is the decay of the pump intensity at large depths, due to the diffusive scattering process that light undergoes. The energy density distribution inside the material is given by the solution to the diffusion equation of the medium. For the slab geometry (that is the case of our experimental sample[¶]), we can use the one dimensional diffusion equation in the direction of propagation z, such that:

$$\frac{\partial I(z,t)}{\partial t} = D\nabla^2 I(z,t) + S(z,t), \tag{5.1}$$

where D is the diffusion coefficient and $S(z)$ the diffusive light source. The steady state solution of the diffusion equation can be written in the complete basis of the Laplacian. In this way the resulting energy density in the medium can be described as a linear combination of the eigenvectors of the Laplacian. The steady state solution to equation 5.1 in a slab geometry across the direction of propagation of light is given by:[99]

$$I_d(z) = \sum_{m=1}^{\infty} I_m(z) = \sum_{m=1}^{\infty} C_m \sin\left(\pi m \frac{z + z_{e1}}{L_{ex}}\right), \tag{5.2}$$

where m is the eigenvector index, C_m is the corresponding coefficient, $L_{ex} = L + z_{e1} + z_{e2}$ is the effective thickness of the sample and z_{e1}, z_{e2} the extrapolation lengths at the front and back surfaces of the sample, respectively, as defined in Section 1.1. The eigenvector's coefficients are derived in the literature[99] and given by:

$$C_m = \frac{A_m L_{ex}^2}{\pi^2 m^2 D} \sin\left(\pi m \frac{z_{inj} + z_{e1}}{L_{ex}}\right), \tag{5.3}$$

where z_{inj} is the thickness at which the light becomes diffuse, or the position of the diffuse source. The elements A_m are given by:

$$\begin{aligned} A_m = & \frac{2I_0\left[\pi m z_{inj}\cos\left(\frac{\pi m z_{e1}}{L_{ex}}\right) - e^{-\frac{L_{ex}}{z_{inj}}}\left(\pi m z_{inj}\cos\left(\pi m\frac{L_{ex}+z_{e1}}{L_{ex}}\right) + L_{ex}\sin\left(\pi m\frac{L_{ex}+z_{e1}}{L_{ex}}\right)\right)\right]}{L_{ex}^2 + \pi^2 m^2 z_{inj}^2} \\ & + \frac{2I_0 L_{ex}\sin\left(\pi m\frac{z_{e1}}{L_{ex}}\right)}{L_{ex}^2 + \pi^2 m^2 z_{inj}^2}. \end{aligned} \tag{5.4}$$

[¶]We use a round sample with a diameter of 18mm and the thickness of the layer over which the optimization is performed is of $29 \pm 2\mu m$. The illumination spot is approximately $66\mu m$ in diameter at the entrance and approximately $112\mu m$ at the back of the sample, still much smaller than the lateral dimensions of the sample, therefore edge effects are negligible and slab geometry is applicable in our case

If we sum all the solutions for the steady-state diffusion equation ($I_m(z)$ in eq. 5.2), it results in the energy density distribution for the non-optimized wavefront, described by eq. 1.7.

The use of diffusion theory for light propagation is valid as long as we neglect the interference effect. It is useful to determine how light propagates through a disordered medium, when the incident light (or light propagation) is not being modified, e.g. by wavefront shaping techniques. In our case, we optimize the wavefront in order to have maximal total transmission, and therefore we are modifying light propagation. As a consequence regular diffusion theory is not valid to describe the propagation of the optimized wavefront. As we mentioned earlier, when we optimize the transmission of the pump and couple more light to the open channels, the energy follows a different distribution.

The energy distribution of an open channel has been investigated in the literature[45,69] and several reasons have led to the conclusion that their energy distribution is very similar to the one described by the fundamental solution ($m = 1$) of the diffusion equation (green curve in Fig. 5.3a). The first main reason is that the fundamental solution is the one that contributes the most to the total transmission, as shown in Fig. 5.3b). As we mentioned before, the optimized wavefront is distributing more light to the open channels, so it should be coupling to the solutions that contribute the most to the transmission. The second important reason is that, as shown in the literature, the energy distribution of open channels is symmetric and peaked at the centre of the sample,[45,69] which are the features of the fundamental solution as well.

Taking all the above arguments into account, although we know that experimentally we are not coupling all the light into an open channel, it is safe to assume that we are coupling more light to the open channels. Although we do not know the energy distribution in our experimental case, it should be in between the diffusive and open channel distributions. For the sake of the comparison, we investigate the energy distributions in the two extremes: diffusive energy distribution (blue curve in Fig. 5.3a) and symmetric energy distribution corresponding to an open channel (green curve in Fig. 5.3a), representing the normalized [‖] distribution of the energy when the wavefront is not optimized and when it is optimized, respectively. Next we study how the different intensity distributions of the illumination pump can affect the collected forward and backwards scattering of Raman light[††] (F_S and B_S respectively) of elements at different depths.

The solution to the diffusion equation depends on different parameters of the sample, which set the boundary conditions to solve the equation, as seen in Section 1.1. In the numerical calculations shown in Fig. 5.3, the parameters of the sample are: $\ell_t = 0.6\,\mu\text{m}, L = 29\,\mu\text{m}$, $\overline{R} = 0.58, D = \frac{v_E \ell_t}{3} \approx 26.5\,\text{m}^2/\text{s}, z_{inj} = \ell_t,\ z_{e1} = z_{e2} = \frac{2}{3}\ell_t \frac{1+\overline{R}}{1-\overline{R}} = 7.6\,\mu\text{m}, L_{ex} = L + z_{e1} + z_{e2}$. These parameters were chosen to match the sample we used in the subsequent experiment.

‖ Details on the process of normalization is detailed in Appendix B

†† Raman scattered light is in principle scattered isotropically.[90] We make the distinction between forward and backwards scattered light to represent the light that is being collected in the forward direction (i.e. transmitted from the slab) and the light that is being collected in the backwards direction (i.e. reflected from the slab).

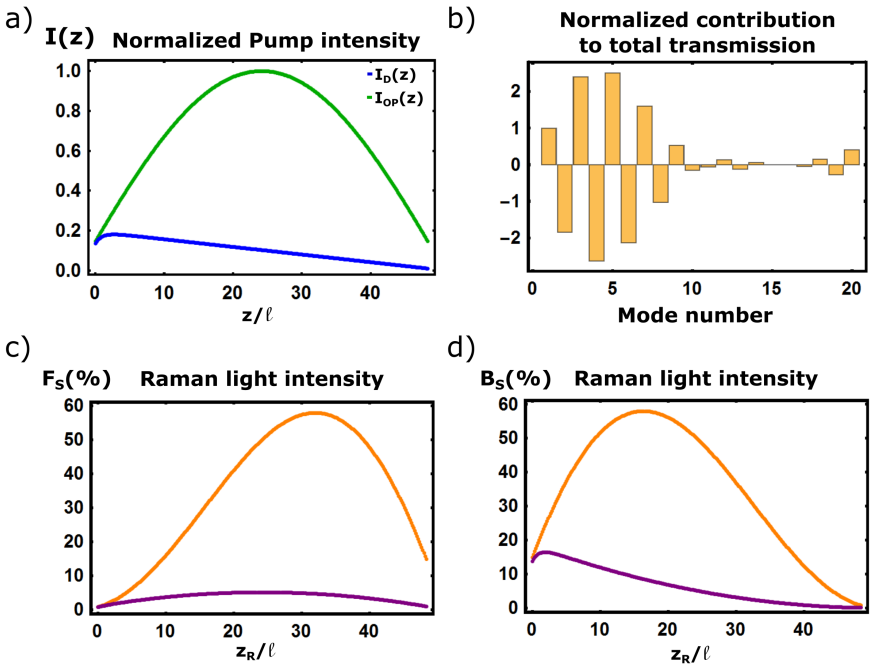

FIGURE 5.3: a) Normalized energy distribution of the pump light when the beam is not optimized (blue) and when all the incident energy is optimized and coupled to the fundamental solution of the diffusion equation (m=1). b) Contribution to the total transmission of the different solutions of the diffusion equation, normalized to the transmission of the fundamental mode. c) Forward scattered Raman light (F_S) of a target at position z_R/ℓ, when the beam is optimized (orange) and when it is not optimized (purple). d) Backwards scattering of the Raman light (B_E) of a target at position z_R/ℓ, when the beam is optimized (orange) and when it is not optimized (purple)

In Fig. 5.3b) we plot the normalized contribution of each of the solutions of the diffusion equation (in eq. 5.2) to the total transmission through the sample, following eq. 1.8. As discussed before, if we manage to couple to an open channel of the sample, the energy distribution would be equivalent to that of the fundamental mode of the diffusion equation, that as we can see, it is the one contributing the most to the total transmission.

Taking into account the intensity distribution of the optimized and non-optimized pump light, we modelled how much Raman scattering we can obtain from an element placed at different depths inside the sample. In order to do that, we assumed that the Raman scattering of the element we want to detect is originated at a specific position (z_R). Once generated, the Raman signal will propagate diffusively to the exit of the sample. Under the assumption that the Raman signal is only generated at position z_R, it is equivalent to assume it is generated by a point source $S(z) = I_0\delta(z - z_R)$, and therefore the intensity distribution follows eq. 1.6. We then calculated the normalized forward and backwards Raman scattering from the point source as the position of the element varied between $z_R = 0$ and $z_R = L$ (see Appendix B for full details on this calculation) if the pump light was the same at all positions inside the medium. However this assumption is false, as we can see in Fig. 5.3a). To obtain the realistic Raman scattering in the forward and backwards directions we weighted the normalized values by the intensity distribution of the pump at each position in depth (detailed in Appendix B). In Fig. 5.3c) and Fig. 5.3d) we plot

the forward and backwards Raman scattering weighted by the pump distribution, respectively. In the horizontal axis we plot the position in depth normalized by the transport mean free path, to give an insight on the optical thickness of the material. In the vertical axis we represent the percentage of the Raman signal that is being scattered in the forward and backwards direction, assuming an absorption-emission ratio of 1, for simplicity. The purple curves represent the Raman signal emitted with the non-optimized or diffusive pump intensity, whereas the orange curve is the resulting Raman scattering with the optimized pump.

An important feature from the graphs in Fig. 5.3c) and Fig. 5.3d) is that when the Raman target is close to the surface where the pump is incident ($z_R \simeq 0$), given that the non-optimized pump deposits more energy in that region (Fig. 5.3a), there is not much difference between the optimized and non-optimized pumps. However, when the Raman element is around the centre of the sample, the optimized pump is much more efficient in generating Raman signal. This is particularly interesting because the centre of the sample is the hardest region to access for conventional Raman spectroscopy.

The study shown in Fig. 5.3 was done for a sample with optical density $OD = L/\ell_t \approxeq 48$, which is comparable to approximately 5 cm of fatty tissues, such as human breast, where the transport mean free path is $\approx$ 1 mm.[32,34] We chose these parameters because they matched the experimental sample of the experiment detailed in the next section. However, in order to see how our approach would work for even optically thicker samples, we repeated the calculations for a thicker sample, $L = 120\,\mu$m, resulting in an optical density $OD = 200$. This would be comparable to approximately 20 cm of breast tissue.

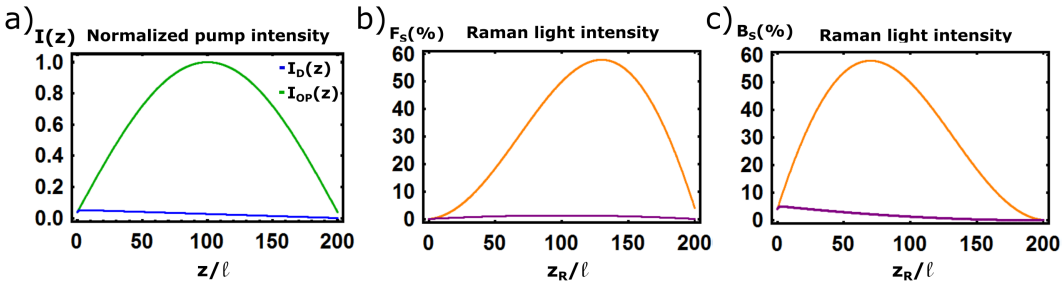

FIGURE 5.4: a) Normalized intensities distributions of a diffusive pump (blue curve) and an optimized pump coupling to an open channel of the sample (green curve). b) Forward Raman scattered light depending on the position of the Raman element (z_R) and the pump distribution. The orange curve represents the Raman scattering generated by the optimized pump, and the purple curve, the Raman scattering generated by the diffusive one. c) Backwards Raman scattered light as a function of the position of the Raman element (z_R) and the pump distribution. The orange curve represents the Raman scattering generated by the optimized pump, and the purple curve, the Raman scattering generated by the diffusive pump.

In Fig. 5.4 we present the numerical results obtained in this case. In Fig. 5.4a) we plot the normalized intensity pumps for a regular diffusive pump (in blue) and for the optimized wavefront coupled to an open channel (in green). As we can see, in this case the energy density of the non-optimized pump becomes very small for large optical densities, and given that by definition the optimized wavefront is being fully transmitted (given that it is coupled to an open channel),

there is a larger difference between the two intensity distributions. When the non-optimized pump is used, we find that the intensity collected higher near the surface of illumination ($z = 0$), in agreement with the results in Fig. 5.3. When the optical density gets larger, the collection of Raman signal becomes very small. When the optimized pump is used, we see how much more energy is at deeper positions of the medium, therefore generating more Raman scattering. As a consequence we see a high increase in the collected forward and backwards Raman scattering at for deeper regions (Fig. 5.4b, c), particularly near the centre of the medium, which is the hardest region to detect for conventional Raman spectroscopy, given that it is not easy to access it with high intensity (conventional) pump.

As a summary of this section we have seen that an optimized pump is very useful to retrieve the Raman signal from elements deep inside a scattering medium, the region of hardest access for conventional Raman spectroscopy. Additionally, we have seen that as the scattering medium becomes thicker, the optimized pump presents more advantages in comparison to the non-optimized one. Although (as we mentioned at the beginning) in our experiments we are not achieving the distribution of the perfectly optimized one presented in this section (given that we are not coupling to the open channels of the sample), when we increase the total transmission through the medium, we are depositing more light into these channels, so we expect the energy distribution to be in between the two presented here. As a consequence, we expect that our experimentally optimized wavefront will present an advantage (versus the non-optimized one) in retrieving the Raman signal of an element deep inside a medium, as we verify in the next section.

5.4 Experiment

In this experiment we increase the Raman scattered light of an element hidden behind a strongly scattering layer, by means of increasing the total transmission of the pump light. By increasing the total transmission of the pump we intend to couple more light to the open channels of the sample, which should deposit more pump intensity at deeper layers of the sample and, consequently, generate more Raman signal of elements embedded deep inside, as discussed in the previous section.

The experimental apparatus is shown in Fig. 5.5. The pump laser has central wavelength in the near infrared $\lambda = 785$ nm, to achieve larger penetration depth in biological tissue. The wavelength region that allows maximal penetration in the optical regime is roughly between $700 and 900$ nm,[32,34] where the absorption band of water has a broad dip. The pump laser is incident on the Spatial Light Modulator (SLM) that iteratively adapts the phase profile of the wavefront. The modulated wavefront is focused on the sample by a microscope objective. A photo-diode collects the total transmitted light (mainly from the pump) and utilizes it as feedback for the algorithm controlling the

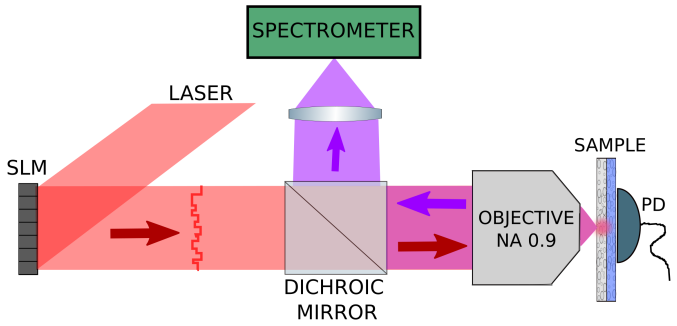

FIGURE 5.5: Schematic of the experimental apparatus used to increase total transmission through a scattering medium whilst the Raman spectra is collected in reflection. Red arrows represent the pump light at 785 nm and the purple arrow represents the longer wavelengths generated due to the spontaneous Raman scattered light.

SLM. A dichroic mirror allows us to filter the pump laser line and analyse the longer wavelengths of the Raman scattered light.

The sample is made of two different scattering materials squeezed between two microscope cover slides. The reason to use a two layered sample is to test how much light we are depositing at a different depth when the total transmission is increased. The incident beam is first impinging on a layer of a highly scattering material (TiO_2) and right behind it there is an inner layer of a common biological element: Hidroxyapatite (HAP)[‡‡]. The spectrometer collects the backscattered Raman light, mostly the signal form the first (or outer) layer of TiO_2. We chose the thickness of this scattering layer so that we could still collect a small amount of Raman signal from the inner HAP layer, to characterize the optimization. We increase the total transmission through the sample and evaluate the intensity from the different layers by looking at the intensity of the Raman spectrum of the different layers. Given that spontaneous Raman scattering is linear with the pump intensity, the intensity increase in Raman spectrum is equivalent to the intensity increase of pump light at the layer.

Naively, one might think that a more direct and effective option to increase the Raman signal from an element would be to use that same Raman signal (from the HAP in our case) as feedback for the optimization algorithm. This procedure has been reported previously in the literature,[100] but that approach is conceptually different from ours. The goal of our experiment is to use this technique for "blind sensing" with Raman spectroscopy, i.e. where one does not know if there is a hidden material, e.g. in breast screenings to know if there are cancerous tumours or not. As a consequence, using the target Raman signal as feedback is not useful for this purpose. Secondly, increasing the pump light instead of the Raman light, has the advantage of using a feedback signal much stronger, which would allow to speed up the optimization to times considerably shorter than that needed for a Raman measurement, and potentially use it for *in vivo* sensing.

[‡‡]More details about the sample and its composition is given below in the subsection **Sample**

Sample

The sample consists of a layer of TiO_2 of thickness $L = 29 \pm 2\,\mu m$ and a second layer of Hidroxyapatite (HAP) with a thickness of $120 \pm 10\,\mu m$. The layer of TiO_2 was chosen because it is a highly scattering material with very little absorption, so a thin layer of this material can lead to large optical densities, that can be compared to thicker biological samples, given that the transport mean free path in the latter is much larger. In our case, the mean free path of TiO_2 is $\ell = 0.6 \pm 0.2\,\mu m$, and the thickness of $L = 29\,\mu m$, which results in an optical density $OD \approx 48$. In biological media such as fatty tissues, where the transport mean free path is approximately 1 mm,[32,34] an optical density of 50, is equivalent to a thickness of approximately 5 cm.

HAP is a calcium phosphate mineral that is used in different biomedical applications,[101] for instance as a marker to detect calcifications in breast tissue.[9] In our case it has the advantage of having its strongest Raman peak well separated from those of TiO_2, which allows a good differentiation in the experiment. Fig. 5.6 shows the spectral data for the TiO_2 and HAP materials (panels a and b) and panel c) shows the combined spectra collected by the spectrometer in the experimental configuration, where we can see the reduced peak from HAP at around $960\,cm^{-1}$, attenuated by the TiO_2 layer in the inset of the figure.

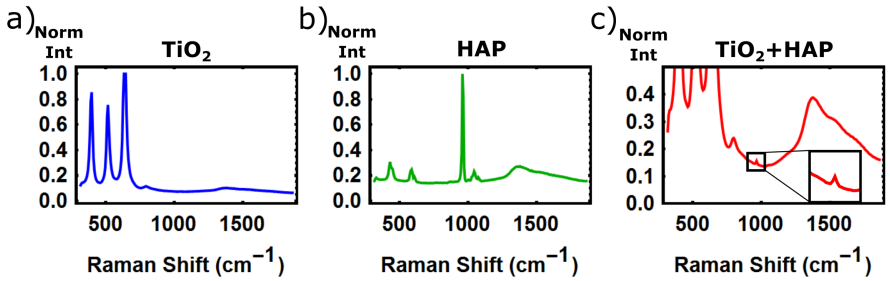

FIGURE 5.6: Normalized Raman spectra of the different materials used in this experiment: a) Anatase TiO_2 spectrum, with three main peaks at $396, 512 and 631\,cm^{-1}$ b) Hydroxyapatite (HAP) with the main peak at $960\,cm^{-1}$ and c) collected spectrum of the combined sample of TiO_2 and HAP, where we can see a strong signal coming from the first layer of TiO_2 and a weak peak coming from the inner HAP at $960\,cm^{-1}$ in the inset. The broad contribution around $1500\,cm^{-1}$ is due to the fluorescence of the microscope cover slip.

5.5 Raman signal enhancement

Using the apparatus described in the previous section, after increasing the total transmission of the pump by a factor close to 1.5, we managed to collect up to 1.48 times a stronger Raman signal from the inner layer of the sample. In Fig. 5.7 we show the intensity corresponding to the inner HAP main peak when no optimization is done (red) and after the wavefront has been optimized (green), and the spectral background subtracted. The solid line curves are Lorentzian fits to the data.

The enhancement in the Raman signal was calculated by looking at the ratio of the areas of the HAP peak when the beam was optimized and not optimized. Given that the measurements of the

optimized and non-optimized spectra were taken with the same integration time, the noise of the spectra is the same, whereas the signal is around 40% stronger in the optimized case, therefore achieving a significant increase in the signal to noise ratio of the Raman spectra. The two spectra were taken consecutively to avoid any possible artefacts, e.g. coming from the sample changing during the optimization time, changes in temperature, etc. This increase in the Raman signal was achieved when the total transmission was increased by 39%, suggesting a simple relationship between the two. In order to test how these two values are correlated, we performed several optimizations with different transmission enhancements and measured the Raman increase in every case.

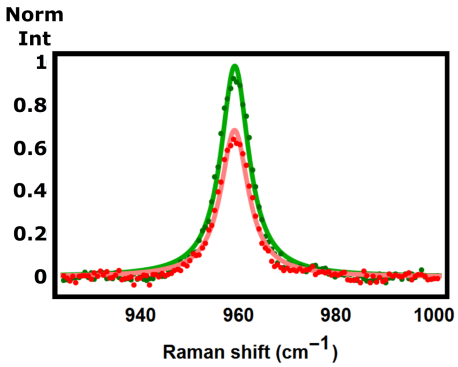

FIGURE 5.7: Graph showing the normalized spectral data points of the HAP peak collected in reflection before and after the wavefront optimization. The red dots represent the data of the HAP peak before the wavefront optimization and the the green ones, after the optimization is done. The red and green solid lines represent the Lorentzian fits of the non-optimized and optimized data respectively. The data in the figure corresponds to an enhancement in the Raman signal of 41%, which was achieved with an increase in total transmission of 39%.

5.5.1 Linearity of the enhancement

We performed several measurements for different values of the increase in total transmission, which shows the relationship between the percentage increases in the Raman emission (R_E) and the increase in the total transmitted intensity (ΔT). The graph in Fig. 5.8 shows the linear scaling between the two.

The best fit linear model, represented by the green solid line, shows a slope of 1.07 $\pm$ 0.12, which tells us there is approximately a one to one relationship between the increase in total transmission and the increase of Raman signal from the second (or inner) layer of the sample. This result does not only reassure that the increase in total transmission is a reliable way of increasing the light delivered deeper inside a material, but it also shows that wavefront shaping can be used to control the intensity deposited through the material, given that it is directly proportional to the increase in total transmission, which is a measurable quantity.

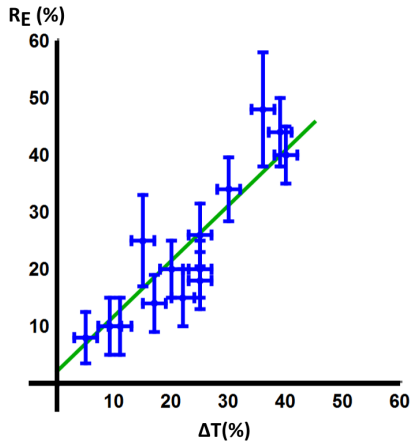

FIGURE 5.8: Plot of the increase in the Raman emission against the increase in the total transmission. It is possible to see how the data points follow a linear trend (in green) with a slope of 1.07 $\pm$ 0.12.

5.6 Estimated increase in penetration depth

As we mention at the beginning of the chapter, the aim of this work was to use wavefront shaping techniques to increase the penetration depth of the pump light, however so far we have just seen how much we can increase the Raman scattered signal from an inner layer, the total transmission of the pump through the sample, and the relationship between the two.

In order to experimentally determine the extra penetration depth that an optimized wavefront reaches versus the non-optimized one, we would need to place the HAP element at different distances or to embed Raman active particles inside the medium at controlled distances. Although that is not impossible, it is experimentally challenging and could not be done for lack of time. Instead, we decided to make an estimate of what is the extra distance at which an element with the extra intensity (given by the optimized pump) can be placed, so that the collected Raman signal from the medium is the same. The Raman signal can be quantified by the total forward and backwards scattering from the medium, which is equivalent to calculate the total transmission or reflection from the Raman source, given by Fick's law (as discussed in Appendix B), and leads to:

$$F_S = -\frac{D}{I_0}\frac{\partial I(z)}{\partial z}\bigg|_{z=L} \quad \text{and} \quad B_S = \frac{D}{I_0}\frac{\partial I(z)}{\partial z}\bigg|_{z=0} \tag{5.5}$$

where F_S is the equivalent to the transmission from a diffusive source (eq. B.5) and B_S is the equivalent to the total reflection from it (eq. B.6). We use different terminology to avoid confusion with transmission or reflection from the pump.

One way of estimating the extra depth achieved as a consequence of the extra pump intensity is by looking at the Signal to Noise Ratio (SNR) of the collected Raman signal. That is, calculate the extra depth at which the optimized and non-optimized Raman intensities give rise to the same SNR. Given that the noise of the measurement will be the same for the optimized or non-optimized

case, this is equivalent to evaluating the intensity of the signal. In order to find the extra depth achieved by the extra intensity in forward scattering, we impose the equality: $F_S(z_R) = F_S^{OP}(z_R^O)$, where $F_S(z_R)$ is the collected forward emission generated by a Raman element at position z_R and $F_S^{OP}(z_R^O)$ is the collected forward emission generated from a Raman element at position z_R^O with the optimized intensity. The same condition has to be set to find the extra depth in reflection: $B_S(z_R) = B_S^{OP}(z_R^O)$. For simplicity and to easily interpret the results, we consider the intensity distribution of a point source Raman element, that follows:

$$I(z) = \frac{\beta I_0}{D}\left(\frac{(z+z_{e1})(L+z_{e2}-z_R)}{L+z_{e2}+z_{e1}} + (z_R - z)H(z-z_R)\right) \tag{5.6}$$

where I_0 is the initial intensity, β is the increase in the Raman intensity due to the wavefront optimization, L the thickness of the medium, z_{e1}, z_{e2} the extrapolation lengths and H is the Heaviside function.

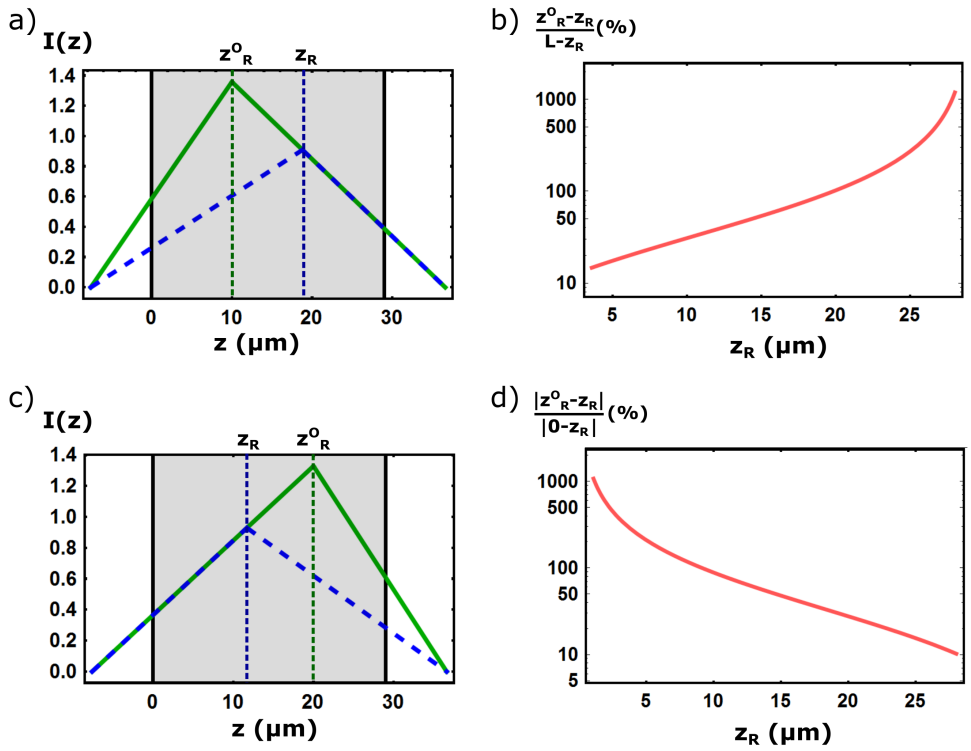

FIGURE 5.9: a) Intensity distributions of Raman elements at two different positions giving rise to the same forward emission. The dashed blue curve represents the intensity distribution of a Raman element excited with a non-optimized pump at position z_R. The green curve represents the intensity distribution of a Raman element at a position z_R^O excited with an optimized pump (with 1.5 times more intensity), farther from the end of the sample ($L = 29\mu m$) and resulting in the same forward emission. b) Normalized increase in the distance at which an optimized Raman element would give rise to the same forward emission than a non-optimized one, dependent on the position of the Raman element (z_R). Vertical axis are represented in logarithmic scale. c) Intensity distribution of an optimized and non-optimized Raman elements resulting in the same backward emission. d) Normalized increase in the distance at which the optimized Raman element should be in order to give the same backwards emission than the non-optimized.

In Fig. 5.9a) we present the intensity distribution of two point Raman elements resulting in the same forward scattering. The grey area represents the limits of the sample. The dashed blue

curve shows a point Raman element of intensity $I_0 = 1, \beta = 1$ (i.e. not optimized) at position z_R, where the peak is. The green curve represents the energy distribution of a Raman element with equivalent forward scattering detected and excited by a larger intensity I^{OP} ($I_0 = 1, \beta = 1.5$) at position z_R^O, further from the output surface (black solid line at $L = 29\,\mu m$). Given that we are using the simplified point source intensity distribution in eq. 5.6, the total forward Raman scattering (eq. 5.5) is essentially given by the slope of the intensity distribution at the exit of the medium. In this way, the forward signal of the two Raman distributions is the same as long as the slopes coincide at the output of the medium, as represented in Fig. 5.9a). When we are interested in measuring the Raman signal scattered in the forward direction, the closer the Raman element is to the output surface, the better (see Fig. B.2 for more details). Therefore, being capable of achieving the same Raman signal from an element which is deeper inside the medium is a important advantage.

The extra distance $d = \mid z_R^O - z_R \mid$ is not fixed for a given increase in pump intensity, but it is dependent on the position of the Raman element. Given that the condition to obtain the same Raman output is reduced to have the same slope (or angle with the horizontal axis), as discussed before, it is possible to calculate the dependency of the extra distance with the position of the Raman element d(z_R) with purely geometrical arguments. Imposing that both intensity distributions hold the same angle in the output side of the sample $z = L$, we have that:

$$\tan(\alpha) = \frac{I(z = z_R)}{Ds_L} = \frac{I^{OP}(z = z_R^O)}{Ds_L^O}, \tag{5.7}$$

where $Ds_L = L - z_R + z_{e2}$, $Ds_L^O = L - z_R^O + z_{e2}$ are the distances to the output surface L. Taking into account that $d = \mid z_R^O - z_R \mid$, and that $I^{OP}(z) = \beta I(z)$, eq. 5.7 gets reduced to:

$$\frac{I(z_R)}{Ds_L} = \frac{\beta I(z_R - d)}{Ds_L + d}. \tag{5.8}$$

Solving eq. 5.8 for the distance d, we obtain that the dependency of the extra distance with the position of the Raman element z_R is given by:

$$\begin{aligned} d(z_R) = {} & \frac{-1}{2\beta}\left(-\beta G(z_R) + \frac{C(z_R)}{Ds_L(z_R)}\right) \\ & + \frac{1}{2\beta}\sqrt{\left(\beta G(z_R) - \frac{C(z_R)}{Ds_L(z_R)}\right)^2 - 4\beta(C(z_R)(1-\beta))}, \end{aligned} \tag{5.9}$$

where the function $G(z_R) = -L + z_{e1} - z_{e2} + 2z_R$ and $C(z_R) = (z_R + z_{e1}) \cdot (L + z_{e2} - z_R)$.

In Fig. 5.9b) we show the extra depth at which a Raman element with the optimized pump can be placed, giving the same output than the non-optimized. In the vertical axis we plot (in logarithmic scale) the normalized increase in the distance to the output surface ($\frac{d(z_R)}{L - z_R}$), achieved by the extra pump intensity. In the horizontal axis we plot the position of the non-optimized Raman

element. When we collect the forward Raman scattering, having extra intensity would help to detect elements which are deeper inside the medium, usually detected with lower intensities. We can see how the increase in the distance to the output surface depends on the position of the element and in the limit, where the non-optimized Raman element is close to the output surface, the optimized Raman element with equivalent transmission is more than 10 times deeper inside (1000% increase).

In Fig. 5.9c) we represent the intensity distribution of two Raman elements excited by the optimized and non-optimized pumps. These are placed at different positions and result in the same Raman signal now collected in the backwards direction. The main difference with Fig. 5.9a) is that the output surface is now at $z = 0$, collecting the backscattered light. In analogy with Fig. 5.9a) the position of the optimized Raman element giving the same signal, is farther from the output surface or deeper inside the medium.

In Fig. 5.9d) we represent the normalized increase in the distance to the output surface of the optimized and non-optimized Raman elements, with the vertical axis in logarithmic scale. The function $d(z_R)$ in this case is slightly different to eq. 5.8. The main differences are that now the distances to the output surfaces are given by $Ds_0 = z_R + z_{e1}, Ds_0^O = z_R^O + z_{e1}$ and $G(z_R)$ has the opposite sign: $G_R(z_R) = -G(z_R) = L - z_{e1} + z_{e2} - 2z_R$, resulting in:

$$d_R(z_R) = \frac{-1}{2\beta}\left(-\beta G_R(z_R) + \frac{C(z_R)}{Ds_0(z_R)}\right) + \frac{1}{2\beta}\sqrt{\left(\beta G_R(z_R) - \frac{C(z_R)}{Ds_0(z_R)}\right)^2 - 4\beta(C(z_R)(1-\beta))} \tag{5.10}$$

In the same way as Fig. 5.9b), we find that the increase in the distance is dependent on the position of the Raman element. In the same way, when the Raman element is close to the output surface of the sample, the equivalent distance of the optimized element is more than ten times larger.

The plots in Fig. 5.9b,d) give an estimate of the increase in the penetration depth due to the increase of the pump intensity inside the medium. We can conclude from these graphs that there is no fixed increase in the penetration depth, but instead it depends on where the Raman element is. The most impressive increase in penetration depth is when the Raman element is close to the output surface, as mentioned earlier. However, when the Raman element is close to the surface, conventional approaches of Raman spectroscopy already work well, so this region is not of enormous interest. When the Raman element is deeper inside, farther away from the output surface, it is still possible to obtain important increases in the penetration depth, between 30-100%. This region is where conventional Raman finds difficult to work in, and an increase of 30-100% in the depth at which they can work can be extremely useful.

5.7 Effect of sample thickness on the signal enhancement

When light propagates through a scattering medium, the thicker the material is, the larger the output illuminated spot will be, as a result of the natural diffusion of light. However a large illuminated spot at the output surface makes wavefront shaping techniques more inefficient and therefore the total increase in the pump intensity will be smaller.

As seen in Section 3.1.2, the efficiency of wavefront shaping techniques in increasing the total transmission depends on the number of modes of the sample that can be controlled. This number is fixed and it is given by the SLM used in the experiment. If the number of modes of the sample is the same that what we can control, we would be in the optimal case. However, as we discussed in Section 1.2, the number of modes of the sample (i.e. the total degrees of freedom) grow linearly with the illuminated area. The illuminated area grows as the beam propagates through the material, as result of the diffusion process, so the illuminated area at the end of the sample will be larger than at the entrance, and the thicker the material, the larger the illuminated area. This implies that there will be more modes at the output of the sample than at the entrance, so we will have control only over a fraction of the total number of modes. Given that the energy travelling through the sample is divided approximately uniformly between the different modes, this means we will only have control over a fraction of the total energy.

The influence of the size of the output spot (and therefore the thickness) on the efficiency of wavefront shaping can be estimated by means of the fidelity factor (see Section 3.2). The contribution to the fidelity factor takes the form of: $\mid \gamma_{cont} \mid^2 = \frac{N_{in}}{N_{out}}$, where N_{in} is the number of controlled modes at the input of the sample (generally given by the number of pixels of the SLM), and N_{out} is the number of modes (proportional to the illuminated area as seen in eq. 1.12) at the output side of the sample. This allows us to estimate how much the total transmission can be increased (eq. 3.39) or how the effect of the thickness reduces the optimal value.

5.8 Summary

In this chapter we have shown that an increase in total transmission of the pump light through a sample leads to an increase of the energy deposited at deeper layers. In particular, we have seen that the optimization of the pump is particularly well suited to detect centred elements, of harder access for conventional Raman spectroscopy. We experimentally increased the total transmission through the sample using wavefront shaping techniques, achieving a maximal increase of 48% in the energy deposited inside. We showed that the increase in total transmission leads to a linear increase in the emitted spontaneous Raman signal of an element hidden behind the TiO_2 layer with $OD \sim 48$. Additionally we estimated numerically and analytically the increase in the penetration depth due to the extra intensity in the medium. We saw that the extra penetration depth

is dependent on the position of the Raman element, that in the central regions of the sample can be between 30-100% larger. These results show the potential of wavefront shaping techniques as a useful tool in sensing applications in scattering media, offering a significant mitigation to the problem of small penetration depth, opening new possibilities to optical sensing in biomedical applications.

Chapter 6

Intensity correlations between transmitted and reflected speckle patterns

In this chapter we present the work conducted in collaboration with Remi Carminati's group at ESPCI in Paris (France).[102] They worked on the theoretical framework and numerical simulations[†]. Ilya Starshinov and myself conducted the experiments presented in this chapter. Most of the results presented in this chapter have been recently published[102] Here we present the first experimental observation of the intensity correlations between reflected and transmitted speckle patterns. In order to place the result into context, we introduce the background theory on speckle correlations in the well studied transmission configuration[104] and the reflection-transmission configuration. We then present the experimental measurement of the correlation function between reflected and transmitted speckle patterns, and show its dependency with the thickness L and scattering mean free path ℓ of the medium, exploring all the range from the single scattering ($L \lesssim \ell$) to the diffusive regime ($L \gg \ell$). In the last part of the chapter we present the agreement between theory and experiments and introduce some preliminary results on polarization dependence of the correlation function, exploring its features beyond the theoretical model.

6.1 Introduction

In multiply scattering materials, coherent light is mostly elastically scattered leading to a seemingly random interference pattern, known as speckle pattern,[42,105] as discussed in Chapter 1. However, speckle patterns are not as random as they seem. The interference between the possible scattering paths in the medium produces spatial correlations between the intensity measured at different positions.[29,104,106] Recently it was demonstrated that these correlations can be used for

[†] Full theoretical calculations and details about the simulations are provided in the PhD thesis of Nikos Fayard,[103] and references therein.

imaging,[10,11] although its use has been limited to the optical memory effect[12] so far, a correlation of purely geometrical origin.

Recent theoretical papers suggested the existence of non-zero statistical correlations between the reflected and transmitted intensity speckle patterns, even for optically thick scattering media.[107,108] Although the presence of these correlations have been mentioned in the past,[109,110] very little attention has been paid to it. Naively one might think that such correlations should quickly average to zero, given that reflected and transmitted waves follow very different scattering sequences, however that is not the case. The existence of this non-zero intensity correlation between reflected and transmitted speckle patterns in optically thick scattering materials open new possibilities for imaging and wave-front control in opaque media, allowing the retrieval of information from the transmitted speckle pattern by just measuring the reflected intensity.

6.1.1 Intensity correlations in the transmitted speckle pattern

Speckle correlations are commonly divided into three categories: Short-range correlations (C_1) that determines the size of a speckle spot, decaying with the separation between the observation points on the scale of the wavelength.[111] Long-range correlations (C_2) with a polynomial decay and originated as a consequence of constraints such as energy conservation or reciprocity,[111–113] and the third are infinite-range correlations (C_3).[104,114]

In order to characterize the correlation function in a disordered medium it is necessary to have some knowledge about the medium or the field interacting with it. The usual approach is based on studying the statistics of the field leaving the disordered medium and the knowledge of the statistical properties of the medium.[103] Considering scattering systems such that $k_0\ell \gg 1$, with k_0 the wave vector in vacuum (as the majority of scattering media where the Anderson localization regime is not considered), the fields following two different scattering paths are independent from each other. As a consequence, the total scattered field should follow Gaussian statistics, due to the central limit theorem.[42] However it is possible that two different scattering paths cross inside the medium and the pairs of fields following these paths[‡] get mixed (see Fig. 6.1), therefore breaking that independence assumption. Non-Gaussian corrections to the field have been derived to take this into consideration,[106,114] resulting in different contributions to the correlation function, such as C_0, C_2 and C_3. The short-range term C_1 is the contribution from the Gaussian approximation of the field.[105] Having this distinction in mind, the total correlation function can be separated in two, representing the Gaussian and non-Gaussian contributions, such that:

$$C^{TT}(\vec{r}_2,\vec{r}_1) = \frac{|\ \langle \delta E_1(\vec{r}_1)\delta E_2(\vec{r}_2)\rangle\ |^2}{\langle I_1\rangle\langle I_2\rangle} + \frac{\langle \delta E_1(\vec{r}_1)\delta E_1^*(\vec{r}_1)\delta E_2(\vec{r}_2)\delta E_2^*(\vec{r}_2)\rangle_c}{\langle I_1\rangle\langle I_2\rangle}, \tag{6.1}$$

‡When fields propagate in pairs (i.e. E, E^*) they can travel longer distances through the sample, giving rise to the diffuse intensity. Paired propagating fields are predominant for thicknesses much larger than the wavelength.

where $\delta f = f - \langle f \rangle$ is the fluctuation of the random variable f and $\langle ... \rangle$ denotes the ensemble average. δE_1 and δE_2 are the fluctuating fields at positions $\vec{r_1}$ and $\vec{r_2}$ in transmission, respectively, and I_1, I_2 their correspondent intensities. The second term of the sum, represented with the sub-index $\langle ... \rangle_c$ represents the connected or non-Gaussian part of the correlation function. The first term of eq. 6.1 corresponds to C_1, or the contribution from the Gaussian approximation of the field. For distances $r_2 - r_1 < \lambda$ the fields δE_1 and δE_2 are strongly correlated, leading to a strong C_1 intensity-intensity correlation, dominating C^{TT}. When the distance between two points is larger than λ the C_1 term vanishes quickly, leaving the second term as the dominant one. The second part of eq. 6.1 is a complicated term to study mathematically, given that it involves all possible ways of connecting four fields inside a medium.

One way of gaining intuition on the complex mathematical expressions such as the non-Gaussian term in eq. 6.1 is the use of diagrammatic representations.[115] The diagrammatic approach[§] is based on the decomposition of scattering sequences into smaller building blocks, in which the information of each scattering sequence is contained. The diagrammatic representation of C_1 in transmission, C_1^{TT}, is shown in Fig. 6.1a). The twisted lines in the diagram represent the fluctuating paired fields (or diffuse intensity)[¶] The solid and dashed lines represent the electric field and its conjugate. The different colours in the diagrams represent pairs of fields travelling originally through different scattering paths. In the diagram leading to the C_1 term, the pairs of fields follow independent propagation or scattering paths up to the last scattering event where they exchange field partners. This is the dominant term between intensities at two different points at distances shorter than λ.

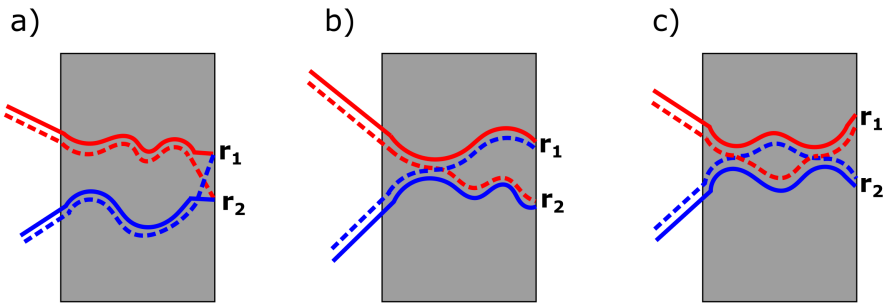

FIGURE 6.1: a) Diagrammatic representation of the field terms leading to the C_1 correlation in the diffusive regime. Different colours represent the fields travelling originally by different scattering paths. In this case both paired fields travel independently from each other up to the very last scattering event where the fields exchange partners. b) Diagram of the field terms leading to the C_2 correlation in the diffusive regime. In this case the fields exchange partners inside the medium, and propagate diffusively afterwards. c) Diagrammatic representation of the field terms leading to the C_3 correlation in the diffusive regime. Here field partners are exchanged twice inside the medium.

[§] An alternative to the diagrammatic approach is based on the Random Matrix Theory, however it is difficult to obtain a physical insight from the results, and it fails to provide an exact form of the correlation function.[116]

[¶] Even though in a scattering material the scattered fields can travel paired or unpaired, after averaging over realizations of disorder the contribution due to the unpaired fields averages out, leaving only the contribution from the paired terms, which is the case we are considering.

The C_2 long-range correlation is the dominant term of the correlation between the intensity of two points or directions from an integrated illumination source. Microscopically this term comes from the exchange of field partners inside the medium, as represented in Fig. 6.1b). The C_3 correlation is the main term of the fluctuation of the integrated intensity when all channels of the medium are excited. This term is the one responsible for the universal conductance fluctuation.[106] It originates from a double exchange of field partners inside the medium, as shown in Fig. 6.1c). An additional infinite-range correlation (C_0) is the leading contribution of the correlation between two distant speckle spots under illumination by a point source located inside the medium.[117]

6.1.2 Intensity correlations in the reflection-transmission configuration

Similarly to eq. 6.1, the correlation function between reflected and transmitted speckle patterns is given by:

$$C^{RT}(\Delta\vec{r}) = \frac{|\langle \delta E_R(\vec{r_1})\delta E_T(\vec{r_2})^*\rangle|^2}{\langle R(\vec{r_1})\rangle\langle T(\vec{r_2})\rangle} + \frac{\langle \delta E_R(\vec{r_1})\delta E_R(\vec{r_1})^*\delta E_T(\vec{r_2})\delta E_T(\vec{r_2})^*\rangle_c}{\langle R(\vec{r_1})\rangle\langle T(\vec{r_2})\rangle}, \tag{6.2}$$

where $\delta E_R(\vec{r_1}), \delta E_T(\vec{r_2})$ are the fluctuating fields in reflection and transmission respectively, at positions $\vec{r_1}$ and $\vec{r_2} = \vec{r_1} + \Delta\vec{r}$. The term $\langle R(\vec{r_1})T(\vec{r_2})\rangle = \langle \delta E_R(\vec{r_1})\delta E_R(\vec{r_1})^*\delta E_T(\vec{r_2})\delta E_T(\vec{r_2})^*\rangle$.

The first term of Eq. 6.2 represents the Gaussian contribution to the correlation function, the short-range C_1 contribution. This contribution can be large, of the order of unity, if the distance between observations points is smaller than the wavelength. Whereas this is possible in the transmission configuration, where points r_1 and r_2 are in the same plane, in the R-T configuration the distance between observation points is $\sqrt{L^2 + \Delta r^2}$, therefore, the C_1 contribution is always negligible for $L \gg \lambda$, as is the case in our experiments. This analysis shows that the R-T configuration is particularly well suited to isolate the non-Gaussian contributions to the correlation function ($\langle \delta E_R(\vec{r_1})\delta E_R(\vec{r_1})^*\delta E_T(\vec{r_2})\delta E_T(\vec{r_2})^*\rangle_c$), without requiring any post-processing to remove the C_1 contribution that dominates in the pure transmission geometry.[111,112,118,119] Non-Gaussian terms are the ones dominating the C^{RT} correlation in the full range from the deep diffusive ($L \gg \ell$) to the quasi-ballistic ($L \lesssim \ell$) regime.

The correlation function between reflected and transmitted speckle patterns is mainly due to the contribution of two Non-Gaussian terms: C_2^{RT} and a new term C_0^{RT}, with the same diagram structure than C_0^{TT}.[102,103] The diagrams representing these contributions are shown in Fig. 6.2.

The diagram of the C_2^{RT} contribution is represented in Fig. 6.2a), and it is the leading term for large optical densities ($OD = L/\ell \gg 1$). It represents the case where the fields are exchanged at the entrance of the medium and one more time inside, after they have propagated diffusively. The long-range character of this term originates from the crossing of two diffusive paths. Due to the multiple scattering sequences that the fields undergo before and after exchanging partners, the C_2^{RT} term is isotropic and independent of the angle of incidence. The contribution of this term

to the correlation function scales as $C_2^{RT} = -f(|\ \Delta\vec{r}\ |)/(k\ L)^2$ (as we verify experimentally in Section 6.4.1),where f is a dimensionless function decaying on a range $|\ \Delta\vec{r}\ | \approxeq\ L$.[107]

There are two main differences between C_2^{RT} and C_2^{TT}: first of all, in the diffusive regime ($L\ \gg\ \ell$), C_2^{RT} is independent of the disorder strength $k\ \ell$, in contrast to $C_2^{TT}\ \sim\ \frac{1}{(k\ \ell)(k\ L)} \propto 1/g$, where g is the dimensionless conductance of the sample.[114] The second difference is the evolution of the information content for detection purposes. Whilst in the case of C_2^{TT} it does not matter where it is measured, i.e. the surface of the sample or in the far field, this is not the case for C_2^{RT}. In order to recover the information of C_2^{RT} it is necessary to measure the intensity pattern on the sample surface, given that in the far field $C_2^{RT}(\vec{k_b},\vec{k_{b'}})\ \sim\ \int C^{RT}(\Delta\vec{r})d\Delta\vec{r} =$ const., for any pair of observation direction $k_b, k_{b'}$, and the information content is uniformly spread across all degrees of freedom.[102,103] For this reason all the measurements described in the next section were done by measuring the speckle patterns at the surface of the sample.

In the single scattering regime ($\ell \sim L \gg \lambda$) the correlation function is dominated by the C_0-type contribution. The diagram leading to this contribution is formally similar to the one leading to the infinite-range C_0 term originated by a point source inside the medium.[117,120] The difference is that in this case the source is an incident plane wave instead of a point source. The diagram is represented in Fig. 6.2b). The contribution of this term to the correlation function scales as $1/(k\ L)^4$ for $OD \gg 1$, therefore at large optical thicknesses the C_2^{RT} term (scaling as $1/(kL)^2$) dominates. In this case the two fields are connected at the entrance of the scattering medium by an extra scattering event (black spot in Fig. 6.2b) and propagate diffusively from there. This extra scattering event makes this term sensitive to the angle of incidence of the illumination beam. This C_0-type contribution to the reflection-transmission correlation is long-range and satisfies $\int \langle C_0^{RT}(\Delta\vec{r})\rangle d\Delta\vec{r} = 0$. This fact leads to the conclusion that this C_0-type contribution is specific to speckle patterns measured on the surface of the sample, vanishing in the far field as C_2^{RT}.

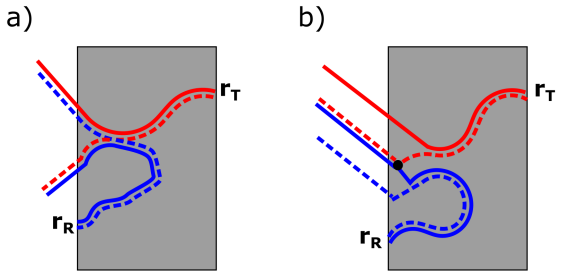

FIGURE 6.2: Diagrams representing the leading terms of the reflection-transmission correlation. a) Diagrammatic representation of the C_2 contribution term to C^{RT}. Two pairs of fields exchange partners inside the medium and propagate diffusively to the different sides of the medium. b) Diagram of the C_0 contribution to the reflection transmission correlation. The fields exchange partners in a scattering event at the entrance of the medium (black spot) and then propagate diffusively to the different sides of the medium.

6.2 Experimental observation of reflection/transmission correlations

6.2.1 Experimental apparatus

The experimental apparatus used to measure the reflection-transmission correlation is shown in Fig. 6.3a). A 2 mW HeNe laser is incident on the scattering sample at an angle of approximately $45°$. The reflected and transmitted intensity patterns, $R(\vec{r})$ and $T(\vec{r})$ respectively, are recorded by two identical imaging systems involving a 10x microscope objective, a plano-convex 150 mm lens, and a CCD camera (Allied Vision Manta G-146). The scattering material is made of a suspension of TiO_2 particles in glycerol. The sample is held between two microscope slides separated by calibrated spacers to form a scattering slab, where the thickness of the sample (L) can be adjusted by using different spacers. The mean free path of the sample (ℓ) is modified by varying the TiO_2 concentration of the solution. In Fig. 6.3b) we show three samples with different optical thicknesses $OD = L/\ell$, from semitransparent ($OD \sim 0.3$) to fully opaque ($OD \sim 2$).

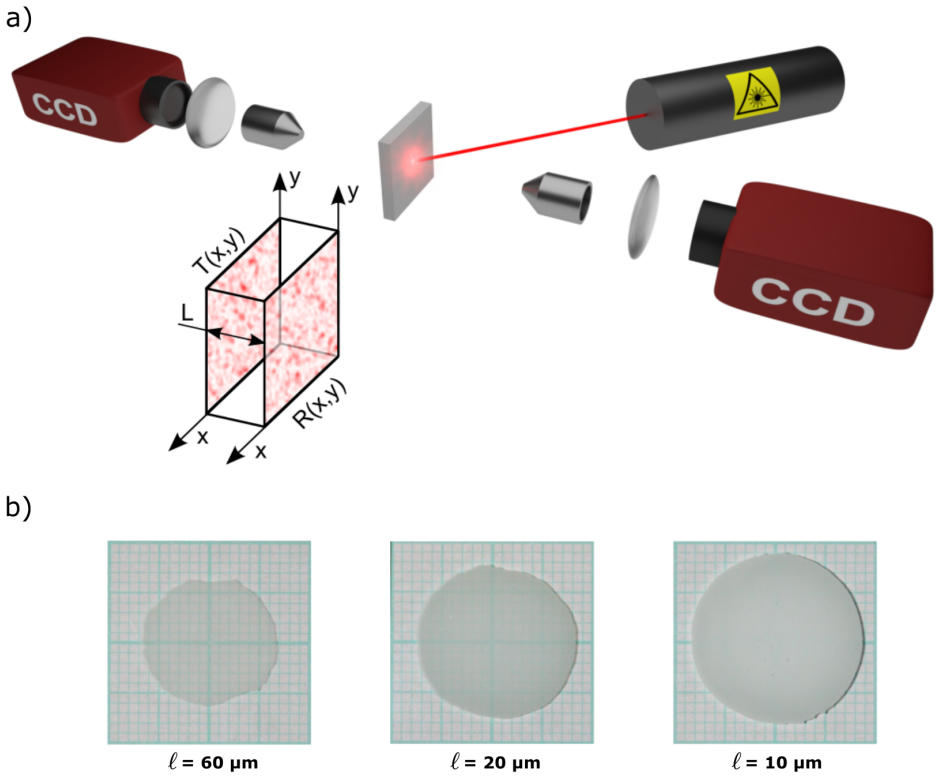

FIGURE 6.3: (a) Experimental set-up: a scattering slab, made of a suspension of TiO_2 particles in glycerol, is illuminated by a HeNe laser incident at an angle $\sim 45°$. The speckle patterns on the two surfaces, $T(x,y)$ and $R(x,y)$ respectively, are recorded with two identical imaging systems. (b) Examples of samples with thickness $L = 20\,\mu m$ but different TiO_2 concentrations: from left to right 5 g/l, 10 g/l and 40 g/l, which correspond to a mean free path of (60, 20.4 and 9.8) $\pm$ 2.5 µm, respectively.

Given that the samples used are liquid, Brownian motion of the scatterers result in continuously changing speckle patterns, with a decorrelation time τ, dependent on the sample thickness. Choosing an integration time in the cameras $< \tau$, and a time interval between successive measurements $> \tau$, it is possible to measure speckle patterns $R(\vec{r})$ and $T(\vec{r})$ for a large number of realizations of disorder. In Fig. 6.4a,b) we show an example of two speckle patterns measured for a given realization of disorder. For each pair of patterns $R(\vec{r})$ and $T(\vec{r})$ we calculate the correlation function C^{RT}, defined as:

$$C^{RT}(\Delta\vec{r}) = \frac{\langle \delta R(\vec{r}) \delta T(\vec{r}+\Delta\vec{r}) \rangle}{\langle R(\vec{r}) \rangle \langle T(\vec{r}+\Delta\vec{r}) \rangle}, \tag{6.3}$$

which is the experimental equivalent to eq. 6.2, where $\Delta\vec{r} = (\Delta x, \Delta y)$ is a transverse shift between the images. In the experiment, the averaging process is performed in two steps[‖]. In first place we perform a cross correlation product between δR and δT, i.e. the integral $\int \delta R(\vec{r}) \delta T(\vec{r}+\Delta\vec{r}) d\vec{r}$, is processed for each realization of disorder. In Fig. 6.4c) we show the 2D plot of the cross-correlation product, showing a random granularity similar to a speckle pattern. The second step consist on ensemble averaging over the realizations of disorder, which shows the shape of the correlation function $C^{RT}(\Delta x, \Delta y)$, with features much larger than a speckle spot (Fig. 6.4d).

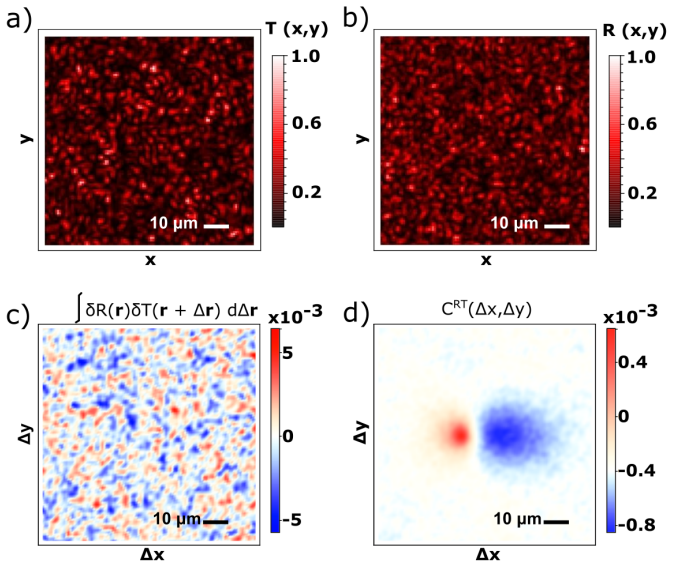

FIGURE 6.4: Typical measured speckle patterns in transmission (a) and reflection (b), for a sample with $L = 20\,\mu$m and $\ell \simeq 60\,\mu$m. (c) Cross correlation product between the speckle patterns in (a) and (b) after average subtraction. (d) Correlation function $C^{RT}(\Delta x, \Delta y)$ obtained after additional ensemble averaging from 10^4 realizations of the disorder. The long-range character of the correlation function, that extends far beyond the size of a speckle spot, is clearly visible.

6.2.2 Experimental results

In Fig. 6.5 we show the correlation function C^{RT} for different mean free paths ℓ and thicknesses L, from the single scattering to the diffusive regime. The upper graph is a 2D map of $C^{RT}(\Delta x, \Delta y)$ and the lower graph represents a cut through $\Delta y = 0$, indicated by a dotted line. The columns display

[‖] Detailed information of this process can be found in Appendix C

the correlation C^{RT} for fixed thicknesses and varying mean free paths. In the rows the samples have the same mean free path and the thickness changes. By looking at the experimental results we find that the shape of C^{RT} varies consistently with the optical density, being dominated by a peak in the single scattering regime ($OD \lesssim 1$), a dip in the diffusive ($OD \gg 1$), and in the intermediate regime a peak and a dip. However, it is clear from the experimental that C^{RT} has a different dependency with ℓ and L, showing how as L becomes larger, the extension of C^{RT} increases as well, for similar OD.

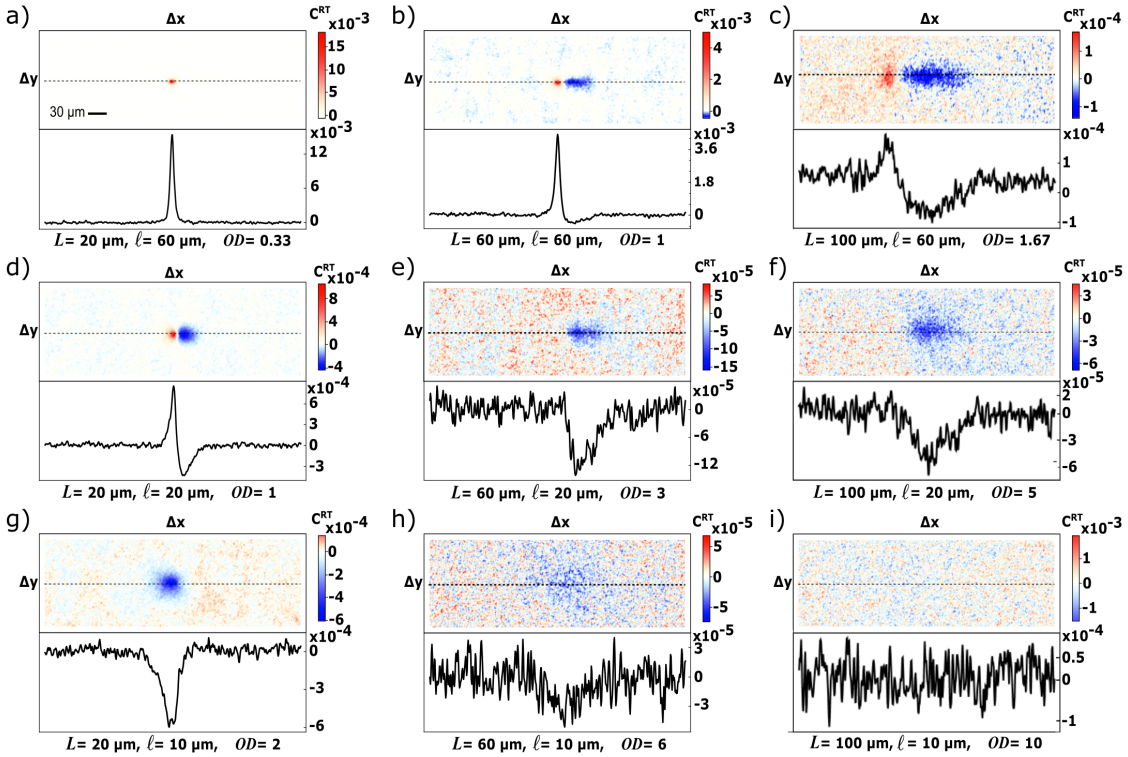

FIGURE 6.5: Averaged reflection-transmission correlation function C^{RT} for different values of L and ℓ and optical thickness $OD = L/\ell$. In each case we show both 2D maps of $C^{RT}(\Delta x, \Delta y)$ and a cross-sections along the line $\Delta y = 0$, indicated as a dotted line in the 2D maps. Two regimes are identified: for moderate optical thickness ($OD \lesssim 1$), the correlation function is dominated by a narrow peak with a negative side lobe. For large optical thicknesses, ($OD > 1$), the correlation function is dominated by a wide negative dip.

As mentioned before, the short-range (C_1) contributions to C^{RT} decay on the scale of the wavelength, therefore C^{RT} is necessarily a non-Gaussian long-range correlation. The measured quantities also exclude any possible specularly reflected or transmitted fields, thanks to the experimental geometry where the beam is incident at an angle.

To support the experimental data, in Fig. 6.6 we present full numerical simulations of wave propagation in three-dimensional disordered media. In the simulations, the samples consist of slabs of dipole scatterers at random positions. Given that the experiments are not resolved in polarization and after travelling a distance of roughly ℓ the wave is expected to be randomly polarized, it can be well approximated by a scalar wave,[121] which simplifies the calculations. The scalar wave equation is solved numerically using the coupled-dipole method.[122] As we can observe, the

general shape of the correlation function is in very good agreement with the experimental data (first column of Fig. 6.2.2) when comparing similar optical densities, $OD < 1$, $OD \simeq 1$ and $OD > 1$.

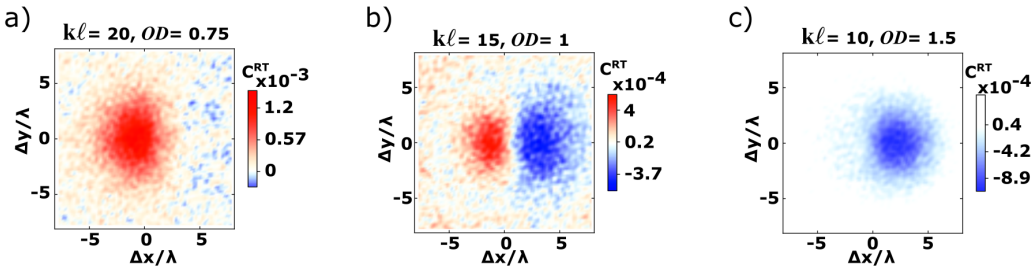

FIGURE 6.6: 2D maps of the correlation function $C^{RT}(\Delta x, \Delta y)$ resulting from 3D numerical simulations in the differnt scattering regimes: a) single scattering ($OD < 1$), b) moderate ($OD \sim 1$) and c) diffuse ($OD \gg 1$).

6.3 Properties of C^{RT}

In the regime of large optical thicknesses $L \gg \ell$, corresponding to Fig. 6.5(e-i), we find that $C^{RT}(\Delta\vec{r})$ is negative, in agreement with the prediction in literature.[107] This means that for every bright spot in reflection (transmission) the corresponding area in transmission (reflection) is more likely to be darker, and *vice versa*. It is worth noting that the existence of negative long-range C_2 correlations has been previously pointed out,[110,123] but this is the first time they have been experimentally observed. The theoretical study of this correlation function showed that both the amplitude and the width of the correlation function depend on L and ℓ,[103] in agreement with the experimental data in Figs. 6.5(e-i). For $L \gg \ell$, the dominant diagrams belong to the class represented in Fig. 6.2a), the long-range C_2^{RT} correlation function.

In the regime of moderate optical thickness $\ell \sim L \gg \lambda$, single scattering is expected to dominate, and we find an intensity correlation much larger than the size of a single speckle spot, as shown in Fig. 6.5(a-d). In this case we have a positive peak appearing in the vicinity of the negative C_2^{RT} contribution. The apparent relative position and amplitude between the peak and the dip depends on the angle of incidence of the illumination (as we discuss in more detail in Section 6.4.2). The long-range character and dependence on the angle of incidence are in agreement with a description based on the diagrams represented in Fig. 6.2b), as mentioned before. Finally, in the quasi-ballistic regime $\ell \gg L \gg \lambda$, which is not the focus of our experiment, we expect the correlation C^{RT} to contain additional contributions to C_2^{RT} and C_0^{RT}.[102,103]

6.4 Further details of the R/T correlation

In order to get a deeper insight on the nature of this newly observed correlation between reflected and transmitted speckle patterns, we performed additional measurements that corroborate the

theoretical derivations as well as measurements that go beyond the developed theory so far.

6.4.1 Thickness dependence of C_2^{RT}

In Section 6.1.2 we discussed how the theory developed by our collaborators at ESPCI determines that in the large optical thickness regime, the C_2^{RT} contribution to the correlation function scales as: $C_2^{RT} = -f(|\,\Delta\vec{r}\,|)/(kL)^2$, meaning that the amplitude of the correlation is independent of the mean free path and only depends on the thickness L. We designed an experiment to check if this scaling can be observed experimentally.

Experimental thickness dependence of C_2^{RT}

Using the same experimental apparatus described in Fig. 6.3 we prepared a new diffusive sample that allowed us to observe the C_2^{RT} correlation for the largest number of thicknesses, in order to obtain a sampling range as large as possible. In this section we experimentally demonstrate the dependence of the amplitude of C_2^{RT} on the thickness of the sample, when the mean free path of the sample is fixed. Ideally we wanted a sample with an optical thickness such that we obtain the sole contribution of the C_2^{RT} term and that it is still visible for a large number of thicknesses, that go in steps of 10 µm due to the availability of spacers. We found that a sample with a mean free path of 16.0 ± 2.5 µm gave us a good range of thicknesses, allowing us to take 6 data points.

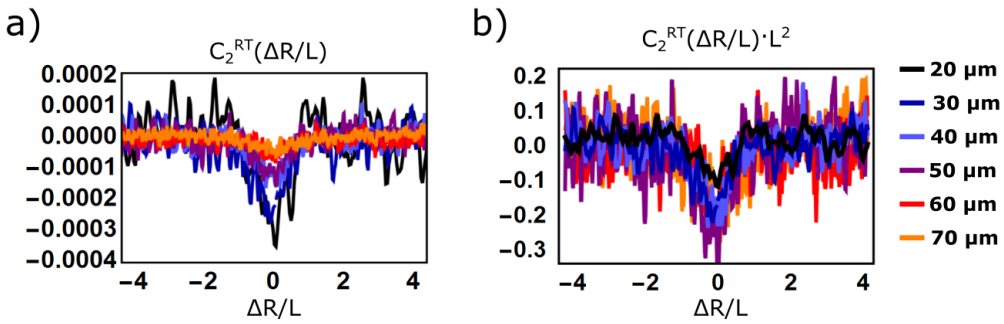

FIGURE 6.7: a) Plot of the dip of the correlation function dominated by C_2^{RT} for different thicknesses of the same sample, against the transverse distance normalized by the thickness L. b) Plot of the correlation function normalized by the thickness factor L^2 for different thicknesses of the same sample, against the transverse distance normalized by the thickness L

In Fig. 6.7 we plot a cross-section (at $\Delta y = 0$) of the correlation function C_2^{RT} over $\Delta R/L$, i.e. the transverse distance normalized by the thickness. In Fig. 6.7a) the amplitude of the correlation function is the original obtained from the experiments. We can see how the amplitude of the correlation functions of samples with different thicknesses decrease as the thickness increases, as expected. As we mentioned above, the theory says the amplitude should decrease with the thickness squared so in Fig. 6.7b) we normalize by this factor and plot $C_2^{RT}(\Delta R/L) \cdot L^2$. If the theory is correct, all curves should overlap with each other, which as we can see is in general well satisfied by our experiment.

This experiment confirms that in the regime of large optical thickness the amplitude of the C_2^{RT} mainly depends on the thickness of the sample, scaling with L^{-2}. It would also be interesting to check the scaling of C_0^{RT}, predicted to drop with L^{-4}, however in order to collect reliable data, ideally we would need to be in a regime where only C_0^{RT} exists, so we can be sure the overall amplitude is not being affected by C_2^{RT}. This means the measurement should be done in the quasiballistic regime or very weak scattering regime but as we mentioned before, we can not be sure there are not additional terms contributing to the peak in the correlation.[102,103]

6.4.2 Dependence on the angle of incidence

In this subsection we examine the dependence of the correlation function $C^{RT}(\Delta\vec{r})$ on the angle of incidence of the beam. In subsection 6.1.2 we discussed that the diagrams leading to C_0^{RT} allow for angular dependence with the incident beam, so we investigate this phenomenon in the moderate optical regime ($\ell \sim L$), where C_0^{RT} is dominant.

In Figure 6.8 we show the experimental line-shape of the correlation function at $\Delta y = 0$ for different angles of incidence. The experimental results correspond to a sample with $OD \sim 1$ with a variation in the angle of incidence from 44° to 73°, limited by experimental constraints. The data represented in Fig. 6.8 has been slightly shifted in the x axis so that the dips of all measurements coincide, with the purpose of facilitating the visualization of the variation of the correlation with the angle of incidence.

As the angle of incidence increases, the line-shape of the correlation changes, and the peak and dip appear separated by a larger distance, at the same time, the peak also increases in size. The shape of this correlation function is interpreted as the superposition of the two contributions to C^{RT}: C_0^{RT} and C_2^{RT}. As discussed in Section 6.1.2 the C_2^{RT} contribution is responsible for a dip and it is independent of the angle of incidence. In this sense, the peak should be the only one moving and changing in size. However we were not able to verify experimentally that only the peak was moving**, although one can clearly see an absolute change in the distance between the peak and the dip.

6.4.3 Polarization dependence

In the study of the correlation function we have never taken into account the polarization of the beam. The main reason is that both the theoretical and numerical studies of the correlation function become much harder to solve. However, as discussed in Section 6.2.2, when polarization is not discriminated in the measurement, assuming a scalar wave reproduces very well the experimental results. Given that from the experimental point of view a study of the polarization does not

**This is because in the experiment the position of the correlation function was highly sensitive on the alignment of the imaging systems. This alignment slightly changed every time we had to, for instance, refocus to a different part of the sample, to avoid inhomogeneous regions due to cluttering of the powder, or if we had to change the sample.

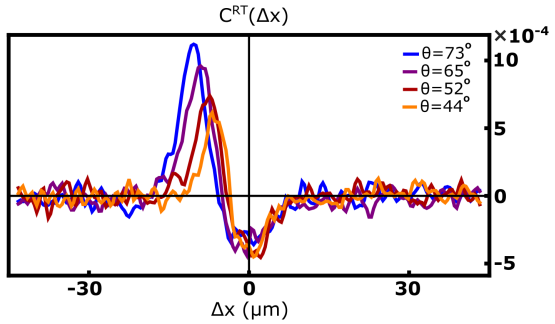

FIGURE 6.8: Experimental data showing the variation of the line-shape of the correlation function as the angle of incidence on the sample is changed.

complicate the experiment significantly we performed an experiment to gain further understanding of the nature of C^{RT}. In this subsection we present the preliminary results obtained when filtering different polarizations in the collected speckle patterns.

The experimental apparatus used for this experiment is very similar to the one described for the main experiment in Fig. 6.3a), with the difference of two additional linear polarizers, placed between the cameras and the focusing lenses. The sample used had an optical thickness $OD \simeq 2$ ($\ell \simeq 16\mu m$ and $L = 30\mu m$). When no polarization is filtered we expect a single and narrow dip dominating the correlation function, in agreement with Fig. 6.5h). In Fig. 6.9a) we show the correlation function obtained in this case, without filtering any polarization, which is in good agreement with Fig. 6.5h). In panels b-e of Fig. 6.9 we show the correlation function with the four combinations of the linear polarizers, when the transmission and reflection polarizers are both parallel to the incident beam (a) (reference polarization), when the transmission polarizer is parallel and the reflection perpendicular (b), when reflection is perpendicular and transmission parallel (d) and when both are perpendicular to the reference (e).

When both polarizers are parallel to the reference (Fig. 6.9b) we can see that a dip still dominates the correlation function. Naively one might expect to retrieve this same correlation function when both polarizers are perpendicular to the reference (Fig. 6.9e), given that they both correlate the same polarization again. However, in this case the correlation function shows an unexpected peak instead of the original dip.

When the polarizers in transmission and reflection are filtering different polarizations we also observe an unexpected behaviour. In principle we could think no correlation should survive, given that we are filtering and therefore correlating speckle patterns with orthogonal polarizations in the different half spaces. However that is not the case. In Fig. 6.9c) we show the correlation function when the transmission polarizer is parallel and the reflection one, perpendicular to the reference. We see a dip dominating the correlation function in this case as well. Again, there is no obvious reason to expect the opposite configuration (transmission perpendicular, reflection parallel) to be different. However, as we can see in (Fig. 6.9c), the correlation function displays a peak rather

than a dip. Surprisingly we find that instead of having a non-zero correlation function, we obtain a peak or a dip depending on which one is perpendicular to the reference.

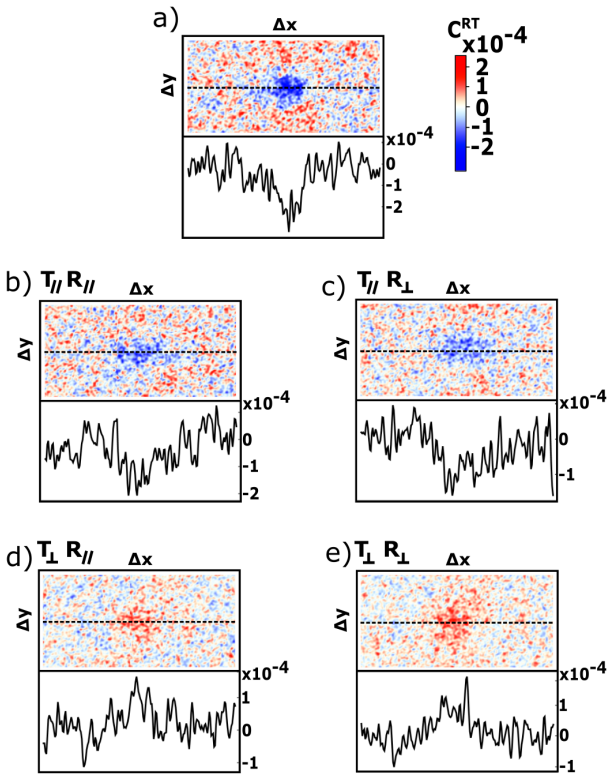

FIGURE 6.9: 2D maps of the correlation function C^{RT} and 1D cuts for $\Delta y = 0$ (indicated by the dotted line) when different polarizations are filtered. a) Correlation function C^{RT} when no polarization is filtered. b) C_2^{RT} when two linear polarizers are parallel to the reference polarization both in reflection and transmission. c) C_2^{RT} when the polarizer in reflection is perpendicular and the one in transmission is parallel to the reference. d) C_2^{RT} when the polarizer in transmission is perpendicular to the reference polarization and the one in reflection, parallel. e) C_2^{RT} when the two linear polarizers are perpendicular to the reference polarization both in reflection and transmission.

We can see that the measurements where the polarizers were used (Fig. 6.9b-e) appear more noisy and the shape of the correlation slightly larger. A possible explanation for this is that we were not retrieving an image exactly from the surface (which is important to clearly appreciate C^{RT}, as discussed in Section 6.1.2). The reason for not being imaging exactly the surface is that the polarizers were added after the imaging systems were focused. Given that re-focusing slightly changes the position of the correlation function, as discussed before, we avoided that, trying to obtain a precise position of the correlation function. However, the orientation of the glass of the polarizer was not perfectly perpendicular and when rotated (to explore all the polarization configurations) the position of the correlation also changed, so the exact position of the correlation function can not be considered artefacts-free.

The preliminary results showed in Fig. 6.9 constitute a step forward towards the full understanding of the nature of the correlation function C^{RT}. In this chapter, we first demonstrated that a purely scalar wave theory works very well to predict and explain the features of the correlation function C^{RT}. However, this last experiment where polarization is taken into account, suggests

that the terms contributing to the correlation function are very dependent on the polarization of the speckle patterns we collect. In particular we have seen that where originally (with no polarization filtering) the correlation function is dominated by a dip, when the transmission polarizer is crossed, we obtain a peak instead. Indeed the correlation function seems to be only dependent on the polarization filtered in transmission, when the polarization in transmission is aligned with the reference, it does not matter if the reflected one is aligned or crossed, we obtain a dip in any case.

These results suggest that the correlation function is made of two main contributions, that can be separated by filtering the polarization. In particular it seems that when the polarization of the transmitted field is crossed with the reference, the C_2^{RT} contribution to the correlation (responsible for the dip) vanishes, suggesting this term keeps a memory of the incident polarization of the beam. When the C_2^{RT} term is filtered out it is possible to see a weak peak as part of the correlation function, invisible otherwise, possibly due to the much stronger contribution of the C_2^{RT} element.

A full study of the polarization dependence in different scattering regimes would be interesting to gain a full and better understanding of this phenomenon. This experiment shows that in order to fully comprehend the correlation function in reflection-transmission, it would be necessary to develop a the analytical and numerical support dealing with vector waves instead of scalar waves. It would also be very interesting to study quantitatively the size of the different elements of the correlation, as well as the relative position.

6.5 Summary

In this chapter we have introduced the correlation function between reflected and transmitted speckle intensity patterns. We have demonstrated experimentally the existence of the C^{RT} correlation function and how its shape depends on the mean free path and thickness of the sample. We have shown how the experiment, theory and numerical simulations find excellent agreement with all the features of the correlation function in all optical regimes, from the diffusive to the quasi-ballistic. We have seen that in the optical regimes studied here there are two main contributions to C^{RT}: C_2^{RT}, responsible of the dip appearing in the diffusive regime and C_0^{RT}, leading term in the moderate optical regime, contributing a peak to the correlation function. These two contributions have different responses to the angle of incidence of the illumination beam and the filtered polarization. These findings open new ways to exploit intensity correlations in the fields of imaging, as we will see in Chapter 7, the control of wave propagation by wavefront shaping techniques[124,125] or mutual information experiments.[108]

Chapter 7

Blind Ghost imaging: using intensity correlations to image through turbid media

In this chapter we present a new approach to imaging, Blind Ghost Imaging (BGI), based on exploiting the correlations between reflected and transmitted speckle patterns that we described in Chapter 6. This new imaging modality has its roots in Ghost Imaging (GI) techniques, so we will first set the background on conventional GI along with its limitations and potentials. Then we will detail what BGI is, the fundamental differences with conventional GI and we will show how this new approach works. To conclude, we present the experimental results showing for the first time the image of an object hidden by an opaque scattering layer of Optical Density $OD \simeq 2.5$. The results presented in this chapter were obtained by Ilya Starshynov and myself.

7.1 Introduction

Imaging objects hidden by scattering media such as white paint, atmospheric turbulence or biological tissue has been an ongoing challenge for years.[6] Random scattering of light produces a blurred image of the object, reducing the resolution and contrast, up to the point in which the object is no longer recognizable. This limitation has been particularly under study for biological applications, where optical imaging usually does not involve damaging the material. In biological samples, the limiting depth at which conventional microscopy can work and retrieve a good image is around 100 µm.[126] Given that in biological tissues the transport mean free path is of the order of 1mm (dependent on the kind of biological tissue[34,126]), this results in an optical density $OD \sim 0.1$. Confocal and multiphoton microscopy managed to retrieve high resolution images beyond this OD, holding a limiting depth of around 1 mm, i.e. $OD \sim 1$.[126] Retrieve a good image for higher OD with optical techniques is difficult, and when possible, it is usually required the use of optical reporters such as fluorescent probes or chromophoric agents and nanoparticles,[126,127] making

the imaging process to some extent invasive or not always safe for medical applications, which limits the application of safe optical imaging techniques for $OD > 1$.

Here we present a non-invasive approach to optical imaging that is capable of retrieving the image of objects hidden by scattering layers of $OD > 2$. It takes advantage of the intensity correlations between the transmission and reflection speckle patterns of the scattering layer (described in Chapter 6). This technique can be added to existing microscopic techniques, allowing imaging objects hidden by scattering layers in principle independently of its opacity[†], in a non-invasive way.

7.2 Ghost Imaging techniques

Ghost imaging was originally developed in 1995 by Pittman *et al*[128] as an imaging technique taking advantage of the quantum nature of light. Despite its origin, it was soon realized that GI techniques could also work with classical light, using classical intensity correlations.[129–131] The field of GI has been attracting great attention from the very beginning, resulting in different experimental realizations, discussions of the fundamental physics as well as a long debate about the quantum or classical origin.[131–134] The experiment and technique described in this chapter make use of purely classical correlations so in the following there will be no discussion of the quantum features of the technique. Despite the variations in the design or approach of the different GI techniques, the general idea is based on the reconstruction of an image from the cross-correlation of the intensity from two spatially separated detectors. The term of "ghost imaging" was coined to point out that none of the beams of light generate an image itself, but it is the correlation of both what yields the image.

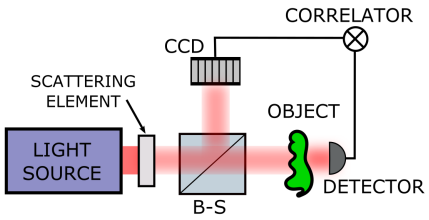

FIGURE 7.1: Typical set-up used for conventional Ghost Imaging experiments.

In Fig. 7.1 we show a typical experimental set-up for classical ghost imaging. This arrangement was initially used to prove the classicality of ghost imaging.[131] In general, a thermal light source passes through a rotating diffuser, resulting in a beam with spatial features. The beam with spatial information is then separated into two by a beam splitter, hence generating two totally (or highly) spatially correlated beams. In one of the arms it is common to have a multi-pixel detector such as a CCD, to image the spatial intensity distribution of the beam. The other half of the beam

[†]As discussed in Chapter 6, the amplitude of C^{RT} correlation decays with the thickness of the material, but it is not technically zero. Consequently, this technique should work as long as there is a non-zero C^{RT} correlation. In the experiment presented in Section 6.2 we measured a non-zero correlation for OD as large as $OD \simeq 6$.

illuminates the object to be imaged. The intensity transmitted (or reflected) by the object is then collected by a bucket detector with no spatial resolution. By correlating the information collected by the two detectors it is then possible to reconstruct an image of the object.

There have been several adaptations to this approach, such as substituting the rotating diffuser by other scattering materials,[135] or generating known patterns with spatial light modulators, giving rise to computational ghost imaging.[134,136]

The image reconstruction is possible because the spatial intensity patterns generated (by the diffuser, other mediums or the SLM) form a complete or over-complete basis. Any image can be written as a linear combination of weight terms of the basis elements. In the case mentioned before, when light goes through a diffuser, a speckle pattern is generated and a large number of different speckle patterns create an over-complete basis over which any image can be reconstructed. The weight factor correspondent to the respective speckle patterns is evaluated by the single pixel detector, that integrates the transmitted intensity of the speckle pattern and the object to image. Experimentally, the spatial distribution of the beam ($T(x,y,z=d)$) is usually collected by a multi-pixel detector, or CCD camera, at a distance $z=d$. For simplicity the object is placed at the same distance d, so one knows immediately that the intensity pattern illuminating the object is the same as the one collected by the camera ($T(x,y,d)$). The intensity recovered by the bucket detector is then $B_i = \int T_i(x,y,d)\, O(x,y)\, dx\, dy$, for every spatial intensity distribution i, and $O(x,y)$ is the the transmitted intensity from the object. The reconstructed image ($I(x,y)$) can then be written as:

$$I(x,y) = \frac{1}{N}\sum_{i=1}^{N} B_i T_i(x,y,d) = \langle B_i T_i(x,y,d)\rangle, \tag{7.1}$$

where N is the number of intensity patterns used to reconstruct the image and $\frac{1}{N}\sum_{i=1}^{N}$ is the averaging operator normalizing the image, equivalent to ensemble average over different spatial distributions of intensity $\langle \ldots \rangle$. The image is then reconstructed by the averaged sum of different spatial intensity distributions with the right weight, provided by the integrated intensity of the bucket detector, which holds the information about the object.

7.3 Blind Ghost Imaging

In this section we present a new variation to conventional Ghost Imaging (GI) techniques: Blind Ghost Imaging (BGI). This new approach exploits the correlations between reflected and transmitted speckle patterns discussed in Chapter 6, in order to reconstruct the image. As we mentioned in the introduction, conventional microscopic techniques are generally limited to work with samples where the scattering layers have an optical density $OD \simeq 1$, given that larger OD blurs and spoil the image. GI techniques have been limited by this phenomena in the same way. The

reconstruction of an image using GI is based on the knowledge of the spatial intensity pattern illuminating the object. If the scattering layer hiding the object is opaque enough ($OD \geq 2$), the pattern illuminating the object will be multiply scattered and will become very different from the original one used as reference, making the image retrieval extremely challenging and therefore posing an important limitation for non-invasive optical techniques.[126,137,138]

However, as we demonstrated in Chapter 6 multiple scattering of light does not fully randomize the beam and correlations between the reflected and transmitted intensity patterns C^{RT} survive, even for highly opaque ($OD \sim 6$) scattering layers. The existence of such correlations means that the reflected pattern contains information about the transmitted one, which is the pattern illuminating the object. BGI techniques use the correlations between reflected and transmitted speckle patterns to obtain information about the pattern that is illuminating the object (transmitted pattern) by measuring the reflected speckle pattern. This allows non-invasive optical imaging through scattering layers with $OD > 2$. Given that the correlation between the reflected and transmitted speckle patterns is not zero, in principle BGI techniques should work for any OD. However, the amplitude of C^{RT} decays with thickness of the sample, as discussed in Chapter 6, and experimentally one will reach a limit beyond which it will not be easy to retrieve the correlation function from the noise. In the experiments presented in Section 6.2 that limit was reached for $OD \simeq 6$.

In order to reconstruct an image with this approach, we can use a very similar process of reconstruction than the one used for conventional GI, with some conceptual differences. First of all, the spatial distribution of the beam that one has access to (reflected speckle pattern $R(x,y)$), is different from the spatial distribution of the beam reaching the object (transmitted speckle pattern $T(x,y)$). The intensity detected by the bucket detector is then: $B_i(x,y) = \int T_i(x,y)O(x,y)dxdy$ for every pattern i. In this way, the image would be formed by:

$$I_B(x,y) = \frac{1}{N}\sum_{i=1}^{N} B_i\, R_i(x,y) = \langle BR(x,y)\rangle. \tag{7.2}$$

In principle $R_i(x,y)$ and $T_i(x,y)$ are very different, so naively one might think there is no way of retrieving an image, given that the measured spatial information $R_i(x,y)$ is weighted by a non-similar integrated amount $\int T_i(x,y)O(x,y)dxdy$. However, as we mentioned before, due to the non-zero correlation between the reflected and transmitted speckle patterns, it is possible to obtain some information of the transmitted pattern ($T_i(x,y)$) by only retrieving the reflected one ($R_i(x,y)$). It is interesting to note that, as discussed in Section 6.2, the correlation function between two single speckle patterns ($R_i(x,y) \circledast T_i(x,y) = C_i^{RT}(x,y)$) does not provide very useful information, resulting in a random pattern with features similar to a speckle pattern (see Fig. 6.4c). It is the ensemble averaged correlation function ($\langle C_i^{RT}(x,y)\rangle = C^{RT}$) that displays the line-shape of with recognizable features only dependent on the parameters of the sample (see Fig. 6.4d). As a

consequence, it is necessary that we make use of the ensemble averaged correlation function in the image reconstruction process.

In order to gain intuition on how an image is retrieved using the Blind Ghost Imaging technique, we need to take make an assumption: approximate the autocorrelation of a speckle pattern by a delta function: $T_i(x,y) \circledast T_i(x,y) = \delta(x,y)$, where $\circledast$ is the correlation product. This is well justified in the experimental situation where a speckle spot can be as large as a pixel. This is equivalent to approximate the C_1 speckle correlation by a delta function, that in reality is a centred peak of the size of a speckle spot with a near-zero background. We know that the correlation between $R_i(x,y)$ and $T_i(x,y)$ is: $R_i(x,y) \circledast T_i(x,y) = C_i^{RT}(x,y)$. Using the previous assumption, as well as the associativity and identity properties of the correlation product, we obtain:

$$T_i(x,y) \circledast (R_i(x,y) \circledast T_i(x,y)) = T_i(x,y) \circledast C_i^{RT}(x,y) \Rightarrow R_i(x,y) = T_i(x,y) \circledast C_i^{RT}(x,y). \quad (7.3)$$

From this equation we can easily see that if $C_i^{RT}(x,y) = \delta(x,y)$ (meaning $R_i(x,y) = T_i(x,y)$ under our assumptions), the image recovered would be given by eq. 7.1. If now $C_i^{RT}(x,y) = -\delta(x,y)$, it would mean that both patterns are complementary (i.e. $R_i(x,y) = -T_i(x,y)$), therefore the outcome of eq. 7.2 would lead to retrieving the negative image of the object. However, as seen in Chapter 6, C_i^{RT} is not a delta function, but a seemingly random function instead (see Fig. 6.4c), and when it is ensemble averaged over disorder it shows features larger than a speckle spot (see Fig. 6.4d), which are dependent on the parameters of the sample. In this case, using eq. 7.3 in eq. 7.2, the reconstructed image results:

$$\begin{aligned} I_B(x,y) &= \frac{1}{N}\sum_{i=1}^{N} B_i T_i(x,y) \circledast C_i^{RT}(x,y) = \frac{1}{N}\sum_{i=1}^{N} B_i \int T_i(x+\Delta x, y+\Delta y) C_i^{RT}(x,y) d\Delta x d\Delta y \\ &= \frac{1}{N}\int \sum_{i=1}^{N} B_i T_i(x+\Delta x, y+\Delta y) C_i^{RT}(x,y) d\Delta x d\Delta y \\ &= \frac{1}{N}\cdot N \int \langle BT(x+\Delta x, y+\Delta y) C_i^{RT}(x,y)\rangle d\Delta x d\Delta y, \end{aligned} \quad (7.4)$$

where the integral comes from the definition of the correlation product. Given that we only know the shape of $\langle C_i^{RT}\rangle = C^{RT}$, we need to simplify the expression in eq. 7.4 further, in order to gain intuition of the effect of the averaged correlation function in the image formation. The covariance function allows us to separate the expected (or averaged) values of a product of variables such that:

$$Cov[X,Y] = E[X,Y] - E[X]E[Y], \quad \text{with} \quad Cov[X,Y] = E[(X - \langle X\rangle)(Y - \langle Y\rangle)], \quad (7.5)$$

where X, Y are different variables and $E[...]$ is the expected or average value. Applying eq. 7.5 to eq. 7.4 we obtain:

$$I_B(x,y) = \int \langle BT(x+\Delta x, y+\Delta y)\rangle \langle C_i^{RT}(x,y)\rangle d\Delta x d\Delta y \\ - \int \frac{1}{N}\sum_{i=1}^{N}[B_i T_i(x+\Delta x, y+\Delta y) - \langle BT(x+\Delta x, y+\Delta y)\rangle][C_i^{RT}(x,y) - \langle C_i^{RT}(x,y)\rangle] d\Delta x d\Delta y \tag{7.6}$$

For simplicity of notation we will omit the variables in T and C_i^{RT} in the next calculations. Simplifying further eq. 7.6, and taking into account eq. 7.1, we have:

$$\begin{aligned} I_B(x,y) =& I(x,y) \circledast \langle C_i^{RT}\rangle - \frac{1}{N}\int \sum_{i=1}^{N} B_i T_i C_i^{RT} d\Delta x d\Delta y + \frac{1}{N}\int \sum_{i=1}^{N} B_i T_i \langle C_i^{RT}\rangle d\Delta x d\Delta y \\ &+ \frac{1}{N}\int \sum_{i=1}^{N} \langle BT\rangle C_i^{RT} d\Delta x d\Delta y - \frac{1}{N}\int \sum_{i=1}^{N} \langle BT\rangle \langle C_i^{RT}\rangle d\Delta x d\Delta y \end{aligned} \tag{7.7}$$

thus:

$$\begin{aligned} I_B(x,y) =& I(x,y) \circledast C^{RT} - \frac{1}{N} N \int \langle BT C_i^{RT}\rangle d\Delta x d\Delta y + \frac{1}{N} N \int \langle BT\rangle \langle C_i^{RT}\rangle d\Delta x d\Delta y \\ &+ \frac{1}{N} N \int \langle BT\rangle \langle C_i^{RT}\rangle d\Delta x d\Delta y - \frac{1}{N} N \int \langle BT\rangle \langle C_i^{RT}\rangle d\Delta x d\Delta y \end{aligned} \tag{7.8}$$

Taking into account that $I_B(x,y) = \int \langle BT C_i^{RT}\rangle d\Delta x d\Delta y$ as seen in eq. 7.4, and that $I(x,y) = \langle BT\rangle$ from eq. 7.1, we have that:

$$I_B(x,y) = I(x,y) \circledast \langle C_i^{RT}\rangle - I_B(x,y) + I(x,y) \circledast \langle C_i^{RT}\rangle + I(x,y) \circledast \langle C_i^{RT}\rangle - I(x,y) \circledast \langle C_i^{RT}\rangle \tag{7.9}$$

which leads to the final result:

$$I_B(x,y) = I(x,y) \circledast \langle C_i^{RT}\rangle = I(x,y) \circledast C^{RT} \tag{7.10}$$

By comparing eq. 7.10 with eq. 7.1 we see that the resulting image is given by the convolution of the original image with the correlation function between reflected and transmitted speckle patterns.

7.3.1 Experimental set-up

The experimental set-up used for the blind ghost imaging experiment is shown in Fig. 7.2a). It is very similar to the one used to measure the correlation between the reflected and transmitted speckle patterns. The object is on the transmission surface of the scattering media, therefore it is illuminated by the transmitted speckle pattern of the scattering medium. An imaging system composed of a 10x microscope objective, 150 mm lens and a CCD camera (Allied Vision Manta G-146) records the image of the speckle pattern at the reflection surface of the sample. The

illumination source is a HeNe laser (2 mW, 632.8 nm) which is incident on the scattering sample at an angle of approximately $45°$.

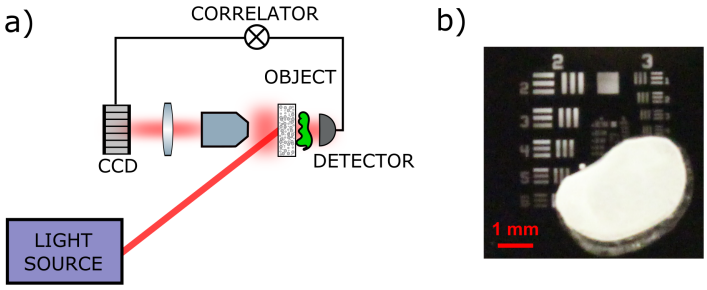

FIGURE 7.2: a) Experimental set-up used for the blind ghost imaging experiment. An imaging system records the reflected speckle at the surface of the scattering media. A bucket detector collects the transmitted intensity modulated by the object. b) Target element used as object for this experiment and a slab of scattering material with $OD \simeq 2.5$ that appears completely opaque.

Sample

The sample used in this experiment consists of a scattering material and an object on one of its surfaces. An image of the sample from the reflection side is shown in Fig. 7.2b). The scattering material is prepared in the same way that the samples used in the experiments in Chapter 6, a solution of TiO_2 particles in glycerol. The sample used in this experiment had an optical density $OD \simeq 2.5$, mean free path of $16 \pm 2.5\,\mu m$ and thickness of $40\,\mu m$. The scattering solution is squeezed between two glasses, a microscope slide and a calibration test target, that works as our object. The pattern on the test target (Thorlabs Negative 1951 USAF test target) is on one of the surfaces. In this way the object is just on the surface of the scattering material. As we can appreciate from Fig. 7.2b), the scattering layer completely hides the target in the region of interest.

7.3.2 Experimental results

We used a small region of the test target as our object, shown in Fig. 7.3a). We collected the reflected intensity of the scattering medium and following eq. 7.4 we reconstructed the image of the object, shown in Fig. 7.3b). Even though the retrieved image is still a bit noisy, it is possible to clearly distinguish all the features of the object.

As seen from eq. 7.10, a consequence of using the correlation between the transmission and reflection speckle pattern as a tool for imaging, is that the retrieved image is convolved with the correlation function of the scattering medium. In Fig. 7.4 we show the averaged correlation function C^{RT} for a sample with the same parameters as the scattering medium used in this experiment.

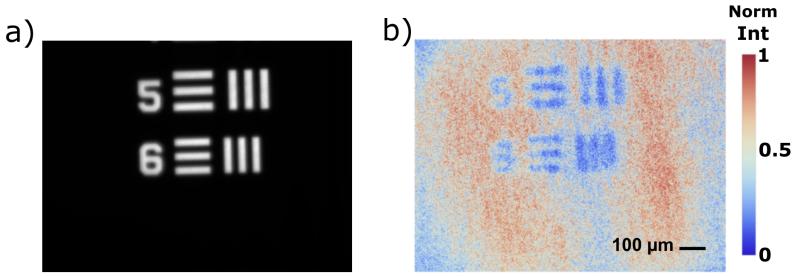

FIGURE 7.3: a) Picture of the region of the test target used as the object to image. b) Reconstructed image of the object shown in panel a, after 2.7 million averages over realization of disorder.

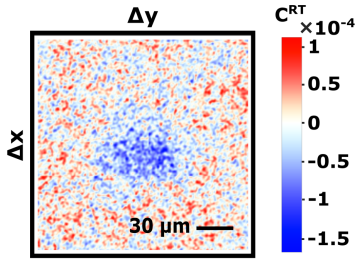

FIGURE 7.4: Correlation function between the reflected and transmitted speckle patterns for a sample with the same parameters ($\ell = 16 \pm 2.5\,\mu m, L = 40\,\mu m$) that the one used for the experiment of Blind Ghost Imaging.

As an illustration of eq. 7.10, here we compare the experimental image obtained by BGI (Fig. 7.3b) with a numerical convolution of the real image (Fig. 7.3a) and the correlation function of the sample (Fig. 7.4). For simplicity we only look at the profile of one of the features of the image, the top right vertical lines in Fig. 7.3 a,b). In Fig. 7.5a) we plot the intensity profile of the vertical lines of the object in Fig. 7.3a). As we could expect, the three lines appear clearly visible and with high contrast. In Fig. 7.5b) we plot an intensity cut of the correlation function shown in Fig. 7.4 at $\Delta y = 0$, presenting a broad and noisy negative dip. In Fig. 7.5c) we represent the numerical convolution of the real image in panel a) and the correlation function in panel b). We can see the intensity profile is now inverted, due to the convolution with the negative correlation function. In Fig. 7.5d) we plot the profile of the vertical lines from the experimental image using the BGI technique. Although it is not easy to make a quantitative comparison, we can see a qualitative resemblance between panel c) and d). In order to make a fair comparison, the correlation function shown in Fig. 7.4 should be obtained exactly with the same sample and experimental conditions, given that these can affect in the amplitude or extension of the correlation function.

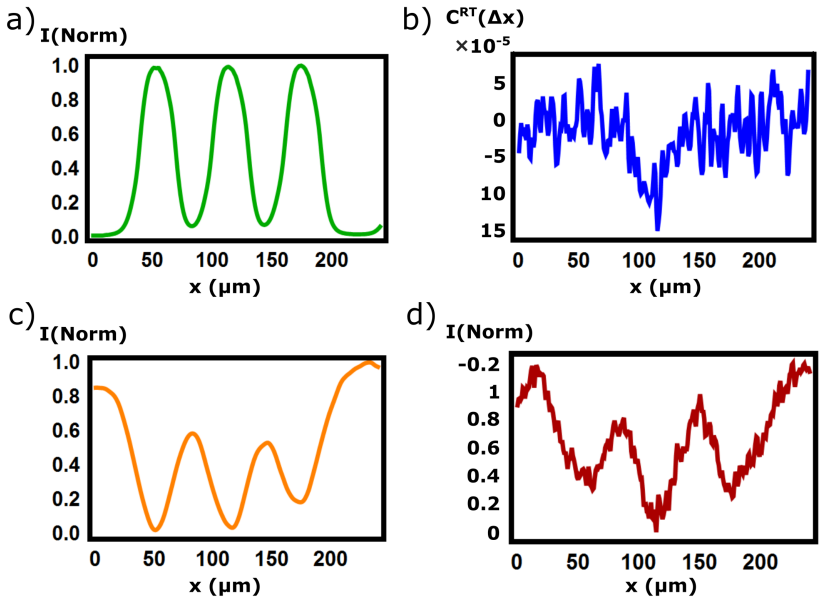

FIGURE 7.5: a) Normalized intensity cut of the top right vertical lines in Fig. 7.3a, b) Intensity cut of the correlation function C^{RT} in Fig. 7.4 at $\Delta y = 0$. c) Numerical convolution of the data presented in panels a and b. d) Intensity cut of the top right vertical lines in Fig. 7.3b.

7.4 Summary and outlook

In this chapter we have presented an alternative approach to conventional ghost imaging that we call blind ghost imaging. The main difference is that instead of using two highly correlated beams reaching the two detectors, now the information reaching the object is retrieved based on the correlations between the reflected and transmitted speckle patterns of the scattering layer hiding the object. We have shown for the first time that the statistical correlations between reflected and transmitted speckle patterns can be used for imaging through an opaque layer of scattering material with $OD \sim 2.5$, although in principle imaging through larger OD should be possible, due to the non-zero correlation C^{RT}. We have seen as well that the image retrieved with this technique is the result of the convolution between the regular image of the object and the correlation function of the scattering layer. This open new possibilities for non-invasive imaging through opaque scattering materials, such as the combination of blind ghost imaging with current imaging techniques in microscopy.

Summary and outlook

The work presented in this thesis is centred around two main areas: wavefront control, exploring its applications in the laser and biological sensing fields, and intensity speckle correlations, where we have presented the first experimental observation of the correlations between transmitted and reflected speckle patterns, characterizing it for the different scattering regimes as well as showing the possibility to use these correlations for imaging through scattering materials.

In the first part of the thesis, dedicated to wavefront control, we have applied wavefront shaping techniques for the correction of a multimode speckled beam into a diffraction limited spot, which could potentially be applied to large improvements in the beam quality and energy of temporally coherent multimode lasers. Although conceptually transforming a speckle pattern into a spot is not new, it is generally done by modifying a plane wave with an SLM before it impinges onto the scattering material. In our case, we directly shaped the speckle pattern, which has not been studied in detail and could lead to new applications of wavefront shaping. In the experiment presented in Chapter 4 we make a detailed study on the transformation of speckle pattern illumination into a diffraction limited spot, achieving a large improvement in the beam quality, as well as the energy deposited on it, in comparison with conventional techniques. We explored the theoretical and experimental expectations, setting a reliable frame for potential applications (e.g. in laser industry). As a further step, it would be interesting to consider the fabrication of a mask to add to the output of temporally coherent multimode lasers, which could enable the single mode operation with small losses in the wavefront correction operations.

The second application of wavefront control is presented in Chapter 5, and it is based on increasing the penetration depth of light in scattering media using wavefront shaping techniques. As mentioned in the introductory chapter, the diffusive behaviour of light limits the penetration depth of light in scattering materials, posing an important limitation for optical sensing techniques. In this experiment, by using an iterative algorithm we shape the wavefront incident on a scattering material, increasing the total transmission through it and consequently modifying the limiting diffusive behaviour. Using a two layered sample, we study the intensity of the Raman scattered light, proportional to the pump intensity, verifying that by means of increasing the pump transmission, we linearly increase the intensity delivered inside. We show with a numerical study that the energy distribution of the optimized pump is particularly well suited for the detection of centred objects, the most disadvantageous configuration for optical sensing techniques in scattering media. We

estimated the increase in the penetration depth of the pump as a consequence of depositing more light inside, finding that the extra distance at which we could detect a Raman element depends on the original position that we are comparing it with, but for centred elements the optimized pump is capable of detecting elements around 30-100% deeper. These results open new possibilities for non-invasive deep optical sensing in turbid media, where wavefront shaping techniques can increase the applicability or current existing techniques such as Raman spectroscopy. The results obtained in this project were performed with a very thin and highly scattering sample, and having biomedical applications in mind, a very interesting future step would be to change the sample for a more realistic one, with thicknesses, transport mean free paths and anisotropy factors closer to the ones of biological media. A further step would be to make the wavefront shaping optimization faster, exploiting the advantages in high speed of the DMD, and perform the optimizations in almost real time, making the technique suitable for *in vivo* biological applications.

The second part of the thesis is dedicated to the study and applications of the intensity correlations between the reflected and transmitted speckle patterns. In Chapter 6 we present the first experimental measurement of this correlation, revisiting briefly the theoretical framework as well as the numerical calculations. We presented a detailed characterization of this correlation in all scattering regimes, from the diffusive to the quasi-ballistic. We highlighted the its dependency with the sample thickness, transport mean free path, angle of incidence and polarization. A further study on the effects of the polarization detected would be very interesting to shine more light on the nature of these correlations. Additionally, a study to show the distance at which the information held in this correlation vanishes will be very interesting for the potential applications. The existence of these correlations open interesting opportunities for non-invasive wave control through scattering media, currently in need to access both sides of the scattering material to gain feedback. Being capable of extracting that information by just measuring the reflection half-space open new potential applications of wavefront shaping techniques. Not only limited to wavefront control, these correlations can be used for imaging as well, as demonstrated in our last project.

In the last part of the thesis we exploit the correlations between transmission and reflected speckle patterns to develop a new imaging technique: Blind Ghost Imaging. In this experiment we do not only demonstrate that the information contained by the correlations can be harnessed for imaging, but we derive the theoretical framework that allows us to characterize elements such as the point spread function, given by the correlation spatial profile, and the expected retrieved image, a convolution of the correlation function with the object to image. The possibility to image an object completely hidden by a optically thick scattering material open new possibilities towards non-invasive optical imaging in turbid media. Further steps in this field could be the use of compressive sensing techniques to speed up the imaging process, or a full non-invasive configuration, having no signal form the transmitted side.

Appendix A

Code for numerical simulations

In this appendix we attach the code that I produced to generate the different numerical simulations along the thesis.

A.1 Total optimal transmission

In Section 3.1.2 we calculated the optimal total transmission that can be achieved under ideal phase modulation, following a step-wise algorithm. In this section we present the code used for the numerical calculations plotted in Fig. 3.2 and Fig. 3.3. The code is written in the programme Wolfram Mathematica.

We first define a transmission matrix `t` of dimension `n` with uncorrelated normally distributed complex elements, centred around 0, with standard deviation σ such that:

```
t = Table[RandomVariate[NormalDistribution[0, σ]] +
 I*RandomVariate[NormalDistribution[0, σ]], n, n];
```

The normalized transmission matrix is then:

```
tn= t/ Abs[Total[Flatten[t]]];
```

We next define the incident field E_i as in eq. 3.11:

```
Ei = Table[E^(I*Mod[ϕ, 2 Pi])/Sqrt[n], n];
```

We then next create an array with the sum of the transmission elements corresponding to one output channel, as in eq. 3.13 for every index `i` of the incident field:

```
Cx = Total[Table[tn[[i]][[j]], {i, 1, n}, {j, 1, n}]];
```

With all this, the initial total transmitted field becomes:

```
InitTotField = Total[Table[Cx[[i]]*1/Sqrt[n], {i, 1, n}]];
```

The field corresponding to one modulated element of the incident field (equivalent to eq. 3.14) is then:

```
MacroField = Table[Ei[[i]]*Cx[[i]], {i, 1, n}];
```

The optimization is based on finding the constructive interference between the modulated field (`MacroField`) and the rest of the transmitted field (`InitTotField-MacroField`), consequently defined as (eq. 3.15):

```
RestField = Table[InitTotField - Cx[[i]]*E[[i]], {i, 1, n}];
```

The intensity interference term between one element modulated in phase and the rest, corresponding to eq. 3.17, is therefore:

```
IntMacroRest = Table[Abs[MacroField[[i]] + RestField[[i]]]^2, {i, 1, n}];
```

In this way, the contribution of this modulated element to the transmitted intensity is:

```
Contrib = Table[Abs[ Evaluate[IntMacroRest[[i]] /.  φ-> RandomReal[0, 2π]] -
Evaluate[IntMacroRest[[i]] /.  φ-> 0]], {i, 1, n}];
```

This corresponds to the contribution of one modulated element to the total transmission. If we now run this for all the elements in the incident field, we will be able to collect and add up all the contributions to the output transmitted field (`Total[Contrib]`). Now this value represents the extra increase in total transmission due to the optimization. To represent the total increase, we add this to the total initial transmission and divide by that same value, so that the total increase in the total transmission, equivalent to eq. 3.32, reads as:

```
Increase = (InitTotInt + Total[Contrib])/InitTotInt;
```

This process give us one total enhancement in transmission, however this code is done for generating i repetitions of the total enhancement, which allow us to generate the histogram. In order to generate a series of total enhancement it is only necessary to add the `For` loop, i.e., `For[i=1,i=NumberIterations, i++`

```
...]
```

Each point of the results presented in Fig. 3.2 is the average value of the list of elements produced in this way. The error bars are the standard deviation of these elements. The information in Fig. 3.3 represent the histograms of these values.

A.2 Effect of speckle illumination over ideal enhancement factor

In this section we present the code used to find out the effect of using a speckle pattern as illumination of the SLM to focus the light to a diffraction limited spot. The next calculations are based on the analytical derivations in Subsection 3.1.1.

In this code we numerically perform 1000 optimizations in order to gain a statistical insight.

(*We first define the lists where the enhancement factors will be stored*)

```
dop = Table[0, 1000];

dsp = Table[0, 1000];
```

(*Here we use the `For` loop to impose the number of optimizations, as in the previous section *)

```
For[j = 1, j < 1001, j++, nn = 1000;
```
(*This is the dimension of the incident vector field E_i*)

```
ArgT = Table[(I*RandomReal[0, 2 Pi]), {i, 1, nn}];
```
(*Here we define Arg[t_{fi}]*)

```
t = Table[RandomReal[0, 1]*E^(ArgT[[i]]), {i, 1, nn}];
```
(*This is equivalent to t_{fi} in Subsection 3.1.1*)

```
y = Table[RandomReal[0, 1]*E^(I*RandomReal[0, 2 Pi]), {i, 1, nn}];
```
(*This is equivalent to ξ_{fi} in Subsection 3.1.1*)

(*Definition of the ideal wavefront according to Cauchy-Swartz condition $\tilde{E}_i \propto t^*_{fi}$ *)

```
wo = Conjugate[t];
```

(*Following eq. 3.8 the ideal enhancement is:*)

```
IdEnhancement = Abs[Total[Table[t[[i]]*wo[[i]], {i, 1, nn}]]]^2/
                Abs[Total[Table[y[[i]]*wo[[i]], {i, 1, nn}]]]^2;
```

(*Definition of the speckled wavefront but optimizing the phase, i.e., $Arg[\tilde{E}_i] = Arg[t^*_{fi}]$*)

```
r = Table[RandomReal[0, 1], {i, 1, nn}];

sw = Table[r[[i]]*E^(-ArgT[[i]]), {i, 1, nn}];

phEnhancement = Abs[Total[Table[t[[i]]*sw[[i]], {i, 1, nn}]]]^2/
                Abs[Total[Table[y[[i]]*wo[[i]], {i, 1, nn}]]]^2;

dop[[j]] = IdEnhancement;

dsp[[j]] = phEnhancement;

]

Mean[dsp]/Mean[dop]≈ 1/2
```

Appendix B

Pump energy distribution and Raman enhancement with optimized and non-optimized wavefronts

B.1 Energy distribution of the pump light

In this Appendix we detail the calculations presented in Section 5.3. When a non-optimized beam impinges on to a scattering slab, it follows a diffusive process described by the one dimensional diffusion equation:

$$\frac{\partial I(z,t)}{\partial t} = D\nabla^2 I(z,t), \tag{B.1}$$

where D is the diffusion constant. Assuming continuous wave light, equation B.1 can be simplified to the steady state equation and it can be written in the complete basis of the Laplacian, which allows to describe the energy density in the medium as a linear combination of the eigenvectors of the Laplacian. The solutions to the steady state diffusion equation in one dimension are:[99]

$$I(z) = \sum_{m=1}^{\infty} I_m(z) = \sum_{m=1}^{\infty} C_m \sin\left(\pi m \frac{z + z_{e1}}{L_{ex}}\right), \tag{B.2}$$

where m is the eigenvector index, C_m is the corresponding coefficient, $L_{ex} = L + z_{e1} + z_{e2}$ is the effective thickness of the sample and z_{e1}, z_{e2} the extrapolation lengths at the front and back surfaces of the sample, respectively, as defined in Section 1.1. The eigenvector's coefficients are derived in the literature[28,99] and given by:

$$C_m = \frac{A_m L_{ex}^2}{\pi^2 m^2 D} \sin\left(\pi m \frac{z_{inj} + z_{e1}}{L_{ex}}\right), \tag{B.3}$$

where z_{inj} is the thickness at which the light becomes diffuse. The elements A_m are given by:

$$A_m = \frac{2I_0\left[\pi m z_{inj}\cos\left(\frac{\pi m z_{e1}}{L_{ex}}\right) - e^{-\frac{L_{ex}}{z_{inj}}}\left(\pi m z_{inj}\cos\left(\pi m\frac{L_{ex}+z_{e1}}{L_{ex}}\right) + L_{ex}\sin\left(\pi m\frac{L_{ex}+z_{e1}}{L_{ex}}\right)\right)\right]}{L_{ex}^2+\pi^2m^2z_{inj}^2} + \frac{2I_0L_{ex}\sin\left(\pi m\frac{z_{e1}}{L_{ex}}\right)}{L_{ex}^2+\pi^2m^2z_{inj}^2}. \tag{B.4}$$

If we sum all the solutions from the steady-state diffusion equation ($I_m(z)$ in eq. 5.2), it results in the energy density distribution for the non-optimized wavefront, described by eq. 1.7 in the limit where $m \to \infty$, represented by the blue curve in Fig. B.1.

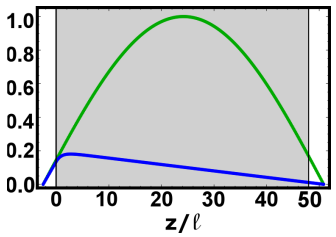

FIGURE B.1: Normalized pump energy densities for a non-optimized (blue) and an optimized (green) beam.

Fig. B.1 represents the energy distribution of the pump (or illumination) beam inside the sample (defined by the grid-lines and with grey background). The horizontal axis is given by the depth normalized by the transport mean free path, accounting for the optical thickness of the element. The vertical axis represents the normalized energy density, that is detailed next.

The normalization of the energy density is done by taking into account the total transmitted (T) and reflected (R) intensities in the medium. In the case of the non-optimized beam, the total transmission is given by Fick's law as a result of flux conservation, leading to:

$$T = -\frac{D}{I_0}\left.\frac{\partial I_d(z)}{\partial z}\right|_{z=L} \tag{B.5}$$

In the same way, total reflection is given by:

$$R = \frac{D}{I_0}\left.\frac{\partial I_d(z)}{\partial z}\right|_{z=0} \tag{B.6}$$

For simplicity, we normalize the intensity distribution of the non-optimized beam so that the total intensity $I_0 = 1$, $I_D = I_d(z)/(R+T)$, which is the blue curve represented in Fig. B.1.

In the case of the optimized beam, the approach for normalization is slightly different. We need to remember that the the diffusive behaviour of light is an approximation and it does not take into account interference. Diffusion theory is widely used because it gives a very good approximation on how the average intensity propagates in a multiply scattering material.

However, when we consider the optimized wavefront, we can couple the incident light to an open channel of the sample. Coupling to open channels can be done by changing the interference happening in the medium, therefore diffusion theory can not describe it properly. However, as mentioned before, it was shown[45] that the energy distribution of a beam coupled to an open channel of the sample has an energy distribution very similar to that of the first solution (m=1) to the diffusion equation[28,69] therefore we use this energy distribution $I_{m=1}(z)$ to describe the energy distribution of the optimized beam. In order to properly normalize the energy distribution, we need to scale it so that the transmission resulting from the first solution is the total transmission[28] (T=1) as a consequence of coupling to an open channel. Using eq. B.2, the transmission corresponding to the first solution is:

$$T_{m=1} = -\frac{D}{I_0}\left.\frac{\partial I_{m=1}(z)}{\partial z}\right|_{z=L} = -\frac{A_1 L_{ex}}{\pi I_0}\sin\left(\pi\frac{z_{inj}+z_{e1}}{L_{ex}}\right)\cos\left(\pi\frac{L+z_{e1}}{L_{ex}}\right) \tag{B.7}$$

The normalized energy distribution of the optimized wavefront, using eq. B.2 is then:

$$I_{OP}(z) = \frac{I_{m=1}(z)}{T_{m=1}} = \frac{1}{T_{m=1}}C_1\sin\left(\pi\frac{z+z_{e1}}{L_{ex}}\right) \tag{B.8}$$

Fig. B.1 represents the two normalized energy distributions of the optimized and non-optimized pump light, both assuming the same initial intensity ($I_0 = 1$).

B.2 Raman intensity output coming from the optimized and non-optimized beams

So far we have looked at the energy distribution of the pump light, however our real interest is to find out what is the effect that the different pumps have over the Raman output light. In order to take this into account, we assume a Raman element as a point source, located at different positions (z_R) within the sample, following eq. 1.6. For each position of the Raman element we evaluate the forward and backwards Raman scattering, given by eq. B.5, and eq. B.6, respectively. The result of this evaluation is represented in Fig. B.2.

As we could expect, when the Raman element is near the end of the sample ($z_R/\ell_t \sim L/\ell_t$), the percentage of collected scattered Raman in the forward direction is maximal and the reflected one, minimal. The opposite happens when the Raman element is close to reflection surface.

Raman intensity output dependent on the pump intensity distribution

The plots presented in Fig. B.2 were calculated assuming the Raman element acting as a source had the same amplitude (or intensity) at any different position z_R, i.e. constant energy distribution with depth, which is of course an idealization. In a real experiment the energy distribution of the

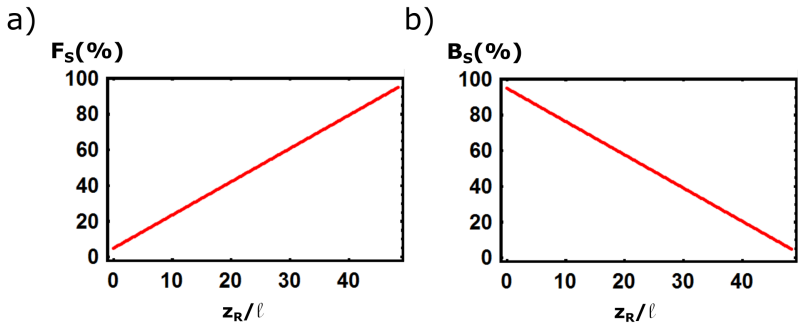

FIGURE B.2: Forward (a) and backwards (b) Raman scattering of an element at position z_R/ℓ, assuming equal intensity of the Raman source at each position.

pump varies with the thickness, as seen in Fig. B.1. The variation of the intensity of the pump with the depth will determine the amplitude of the Raman scattered light at the different positions. In order to take the spatial distribution of the pump into account, we weight the Raman scattered light presented in Fig. B.2 by it. We normalize the pump distributions to a global maximal value of 1 so that the results are easier to interpret. Fig. B.3 shows the result of the weighted Raman forward a) and backwards b) scattering.

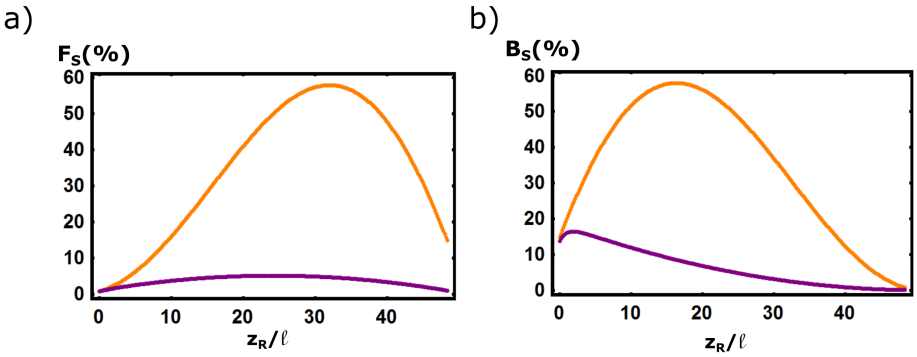

FIGURE B.3: a) Normalized forward collected Raman scattered light of a target at position z_R/ℓ, when the beam is optimized (orange) and when it is not optimized (purple). d) Total backwards collected Raman scattered light of a target at position z_R/ℓ, when the beam is optimized (orange) and when it is not optimized (purple)

Appendix C

Experimental calculation of the correlation function

In order to experimentally measure the correlation function $C^{RT}(\Delta\vec{r})$ defined by eq. 6.3, it is necessary to perform two average processes. In first place we take a spatial average, $\int \delta R(\vec{r})\delta T(\vec{r}+\Delta\ \vec{r})d\vec{r}$, which is the cross correlation of every pair of reflected and transmitted speckle patterns. After the spatial average is done, we perform an ensemble average of the correlation function over the realizations of disorder, which leads to the final correlation function used in eq. 6.3.

It is important to notice that the speckle patterns measured are subject to artefacts from the cameras. In Figs. C.1a) and C.1b) we show two typical speckle patterns measured from the cameras. At a first glance it looks like proper speckle and we don't see any sign of undesired artefact. However after averaging over a large number of realizations of disorder we find an irregular pattern that is present in all the measurements (see Figs. C.1c) and C.1d)). These fringe patterns are due to the interference of the light in the glass window in front of the CCD chip. If we measure the correlation function without subtracting the irregular fringe pattern from the cameras, the correlation function C^{RT} will be hidden by a large inhomogeneous background (see Figs. C.1e)). In order to obtain the proper correlation function (defined in eq. 6.3) it is necessary to substract the fringe pattern present in every measurement of speckle, which allows us to recover the quantities δT and δR appearing in eq. 6.3. When the background intensity of the speckle patterns is properly subtracted, it is possible to recover the real shape of the correlation function C^{RT} (see Figs. C.1f)).

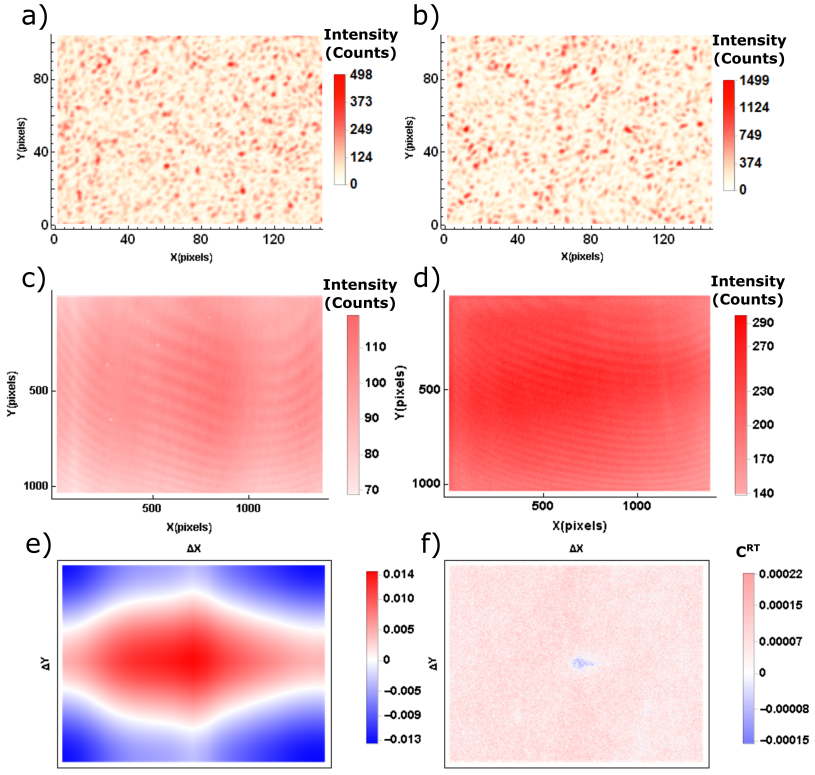

FIGURE C.1: a) Typical raw speckle pattern in reflection and b) in transmission. c) Averaged intensity pattern over 2000 realizations of disorder in reflection and d) in transmission. e) Resulting correlation function when the fringe patterns in (c) and (d) have not been subtracted from the speckle images. f) Cross-correlation between δR and δT as described in the main text.

Bibliography

[1] Euclid. *Optica*. *c.* 300 BC.

[2] E. Hecht. *Optics*. Addison-Wesley, 2002, p. 698.

[3] M. Born and E. Wolf. *Principles of optics : electromagnetic theory of propagation, interference and diffraction of light*. Pergamon Press, 1980, p. 808.

[4] B. E. A. Saleh and M. C. Teich. *Fundamentals of Photonics*. Wiley Series in Pure and Applied Optics. New York, USA: John Wiley & Sons, Inc., 1991.

[5] N. I. Zheludev. "What diffraction limit?" In: *Nature Materials* **7**:6 (2008), pp. 420–422.

[6] A. Ishimaru. "Limitation on image resolution imposed by a random medium". In: *Applied Optics* **17**:3 (1978), pp. 348–352.

[7] Nick Pfeiffer et al. "Optical imaging of structures within highly scattering material using a lens and aperture to form a spatiofrequency filter". In: *Biomedical Optics (BiOS) 2008*. International Society for Optics and Photonics. 2008, pp. 68541D–68541D.

[8] Glenn H Chapman et al. "Angular domain optical imaging of structures within highly scattering material using silicon micromachined collimating arrays". In: International Society for Optics and Photonics. 2003, pp. 462–473.

[9] P. Matousek and N. Stone. "Emerging concepts in deep Raman spectroscopy of biological tissue". In: *Analyst* **134**:6 (2009), pp. 1058–1066.

[10] J. Bertolotti et al. "Non-invasive imaging through opaque scattering layers". In: *Nature* **491**: (2012), p. 232.

[11] O. Katz et al. "Non-invasive single-shot imaging through scattering layers and around corners via speckle correlations". In: *Nature Photon.* **8**: (2014), p. 784.

[12] Isaac Freund, Michael Rosenbluh, and Shechao Feng. "Memory Effects in Propagation of Optical Waves through Disordered Media". In: *Phys. Rev. Lett.* **61**: (20 1988), pp. 2328–2331.

[13] M. Fink. "Time Reversed Acoustics". In: *Phys. Today* **50**: (1997), pp. 34–40.

[14] I. M. Vellekoop and A. P. Mosk. "Focusing coherent light through opaque strongly scattering media". In: *Opt. Lett.* **32**:16 (2007), p. 2309.

[15] D. Akbulut et al. “Focusing light through random photonic media by binary amplitude modulation”. In: *Optics express* **19**:5 (2011), pp. 4017–4029.

[16] A. M. Caravaca-Aguirre et al. “Real-time resilient focusing through a bending multimode fiber”. In: *Optics Express* **21**:10 (2013), p. 12881.

[17] Hyeonseung Yu et al. “Depth-enhanced 2-D optical coherence tomography using complex wavefront shaping”. In: *Optics express* **22**:7 (2014), pp. 7514–7523.

[18] I. N. Papadopoulos et al. “High-resolution, lensless endoscope based on digital scanning through a multimode optical fiber”. In: *Biomedical Optics Express* **4**:260 (2013).

[19] T. Čižmár et al. “Exploiting multimode waveguides for pure fibre-based imaging”. In: *Nature Communications* **3**: (2012), p. 1027.

[20] Y. Choi et al. “Scanner-free and wide-field endoscopic imaging by using a single multimode optical fiber”. In: *Physical Review Letters* **109**:20 (2012), p. 203901.

[21] E. G. Van Putten et al. “Scattering lens resolves sub-100 nm structures with visible light”. In: *Physical Review Letters* **106**:19 (2011), p. 193905.

[22] A. P. Mosk et al. “Controlling waves in space and time for imaging and focusing in complex media”. In: *Nature Photon.* **6**: (2012), p. 283.

[23] Eran Small et al. “Spectral control of broadband light through random media by wavefront shaping”. In: *Optics letters* **37**:16 (2012), pp. 3429–3431.

[24] R Horstmeyer et al. “Secure Storage of Cryptographic Keys within Random Volumetric Materials”. In: *Lasers and Electro-Optics (CLEO), 2013 Conference*. IEEE. 2013, pp. 1–5.

[25] S. A. Goorden et al. “Quantum-secure authentication of a physical unclonable key”. In: *Optica* **1**:6 (2014), p. 421.

[26] W. Choi et al. “Preferential coupling of an incident wave to reflection eigenchannels of disordered media”. In: *Scientific reports* **5**: (2015).

[27] I. M. Vellekoop and A. P. Mosk. “Universal Optimal Transmission of Light Through Disordered Materials”. In: *Physical Review Letters* **101**:12 (2008), p. 120601.

[28] O. S. Ojambati et al. “Coupling of energy into the fundamental diffusion mode of a complex nanophotonic medium”. In: *New Journal of Physics* **18**:4 (2016).

[29] M. C. W. van Rossum and T. M. Nieuwenhuizen. “Multiple scattering of classical waves: microscopy, mesoscopy, and diffusion”. In: *Reviews of Modern Physics* **71**:1 (1999), p. 313.

[30] A. Ishimaru. *Wave Propagation and Scattering in Random Media*. IEES Press, New York, 1997.

[31] H.C. Van de Hulst. *Light scattering by small particles*. Dover Publications, 1981, p. 480.

[32] T. Vo-Dinh. *Biomedical Photonics Handbook: Fundamentals, Devices and Techniques*. Vol. 1. CRC press, 2014.

[33] J. Ripoll et al. “Experimental determination of photon propagation in highly absorbing and scattering media”. In: *Journal of the Optical Society of America A* **22**:3 (2005), p. 546.

[34] S. L Jacques. “Optical properties of biological tissues: a review”. In: *Physics in Medicine and Biology* **58**:11 (2013), R37–R61.

[35] J. Bertolotti. “Light transport beyond diffusion”. PhD thesis. Universita degli Studi di Firenze, 2007.

[36] J. Stam. “Multiple scattering as a diffusion process”. In: *Rendering Techniques 95*. Springer, 1995, pp. 41–50.

[37] J. F. De Boer. “Optical fluctuations on the transmission and reflection of mesoscopic systems”. PhD thesis. Universiteit van Amsterdam, 1995.

[38] D. Akbulut. *Measurements of strong correlations in the transport of light through strongly scattering materials*. Universiteit Twente, 2013.

[39] J. X. Zhu, D. J. Pine, and D. A. Weitz. “Internal reflection of diffusive light in random media”. In: *Physical Review A* **44**:6 (1991), pp. 3948–3959.

[40] J. Gomez Rivas et al. “Optical transmission through strong scattering and highly polydisperse media”. In: *Europhysics Letters (EPL)* **48**:1 (1999), pp. 22–28.

[41] J. Karger. *Diffusion Fundamentals : Leipzig 2005*. Leipziger Universitatsverlag, 2005.

[42] J. W. Goodman. *Speckle phenomena in optics : theory and applications*. Roberts, 2007.

[43] C. W. J. Beenakker. “Random-matrix theory of quantum transport”. In: *Reviews of modern physics* **69**:3 (1997), p. 731.

[44] E. G. Van Putten. “Disorder-Enhanced Imaging with Spatially Controlled Light”. PhD thesis. University of Twente, 2011.

[45] W. Choi et al. “Transmission eigenchannels in a disordered medium”. In: *Physical Review B* **83**:13 (2011), p. 134207.

[46] A Goetschy and A D Stone. “Filtering random matrices: The effect of incomplete channel control in multiple scattering”. In: *Physical Review Letters* **111**:6 (2013).

[47] J. Wishart. In: *Biometrika* **20A**:1/2 (1928), p. 32.

[48] E. P. Wigner and P. A. M. Dirac. “On the statistical distribution of the widths and spacings of nuclear resonance levels”. In: *Mathematical Proceedings of the Cambridge Philosophical Society* **47**:04 (1951), p. 790.

[49] M.L. Mehta. “On the statistical properties of the level-spacings in nuclear spectra”. In: *Nuclear Physics* **18**: (1960), pp. 395–419.

[50] P. J. Forrester, N. C. Snaith, and J. J. M. Verbaarschot. “Developments in random matrix theory”. In: *Journal of Physics A: Mathematical and General* **36**:12 (2003), R1–R10.

[51] T. Guhr, A. Mueller-Groeling, and H. A. Weidenmueller. “Random Matrix Theories in Quantum Physics: Common Concepts”. In: *Phys. Rept.* **299**:189 (1998).

[52] O.N. Dorokhov. “On the coexistence of localized and extended electronic states in the metallic phase”. In: *Solid state communications* **51**:6 (1984), pp. 381–384.

[53] J.B. Pendry, A. MacKinnon, and A.B. Pretre. “Maximal fluctuations — A new phenomenon in disordered systems”. In: *Physica A: Statistical Mechanics and its Applications* **168**:1 (1990), pp. 400–407.

[54] M. Kim et al. “Maximal energy transport through disordered media with the implementation of transmission eigenchannels”. In: *Nature photonics* **6**:9 (2012), pp. 581–585.

[55] B. Gérardin et al. “Full transmission and reflection of waves propagating through a maze of disorder”. In: *Physical review letters* **113**:17 (2014), p. 173901.

[56] S. M. Popoff et al. “Measuring the Transmission Matrix in Optics: An Approach to the Study and Control of Light Propagation in Disordered Media”. In: *Physical Review Letters* **104**:10 (2010), p. 100601.

[57] Rudolf Sprik et al. “Eigenvalue distributions of correlated multichannel transfer matrices in strongly scattering systems”. In: *Physical Review B* **78**:1 (2008), p. 012202.

[58] Alexandre Aubry and Arnaud Derode. “Random Matrix Theory Applied to Acoustic Backscattering and Imaging In Complex Media”. In: *Physical Review Letters* **102**:8 (2009), p. 084301.

[59] V. A. Marcenko and L. A. Pastur. “Distribution of eigenvalues for some sets of random matrices”. In: *Mathematics of the USSR-Sbornik* **1**:4 (1967), pp. 457–483.

[60] I. M. Vellekoop and C. M. Aegerter. “Focusing light through living tissue”. In: *BiOS*. International Society for Optics and Photonics. 2010, p. 755430.

[61] M. Cui, E. J McDowell, and C. Yang. “An in vivo study of turbidity suppression by optical phase conjugation (TSOPC) on rabbit ear”. In: *Optics express* **18**:1 (2010), pp. 25–30.

[62] W. Lee. “Binary computer-generated holograms”. In: *Applied Optics* **18**:21 (1979), pp. 3661–3669.

[63] E. G. Van Putten, I. M. Vellekoop, and A. P. Mosk. “Spatial amplitude and phase modulation using commercial twisted nematic LCDs”. In: *Applied optics* **47**:12 (2008), pp. 2076–2081.

[64] S. A. Goorden, J. Bertolotti, and A. P. Mosk. “Superpixel-based spatial amplitude and phase modulation using a digital micromirror device”. In: *Optics express* **22**:15 (2014), pp. 17999–18009.

[65] J.W. Goodman. *Introduction to Fourier Optics 3ed*. Roberts & Co, 2005, p. 491.

[66] H. Yilmaz. “Advanced optical imaging with scattering lenses”. PhD thesis. University of Twente, 2015.

[67] I. M. Vellekoop and A. P. Mosk. “Phase control algorithms for focusing light through turbid media”. In: *Optics communications* **11**:281 (2008), pp. 3071–3080.

[68] I. M. Vellekoop. “Controlling the propagation of light in disordered scattering media”. PhD thesis. University of Twente, 2008.

[69] M. Davy et al. “Universal structure of transmission eigenchannels inside opaque media”. In: *Nature communications* **6**: (2015), p. 6893.

[70] I. M. Vellekoop. “Feedback-based wavefront shaping”. In: *Optics express* **23**:9 (2015), pp. 12189–12206.

[71] B. A. Remington et al. “A review of astrophysics experiments on intense lasers”. In: *Physics of Plasmas* **7**:5 (2000), pp. 1641–1652.

[72] M. Kuznetsov et al. “High-power (> 0.5-W CW) diode-pumped vertical-external-cavity surface-emitting semiconductor lasers with circular TEM/sub 00/beams”. In: *IEEE Photonics Technology Letters* **9**:8 (1997), pp. 1063–1065.

[73] Y. Izawa et al. “High power lasers and their new applications”. In: *Journal of the Optical Society of Korea* **12**:3 (2008), pp. 178–185.

[74] C. Degen, I. Fischer, and W. Elsäßer. “Transverse modes in oxide confined VCSELs: Influence of pump profile, spatial hole burning, and thermal effects”. In: *Opt. Express* **5**:3 (1999), pp. 38–47.

[75] J. R. Marciante et al. “Near-diffraction-limited operation of step-index large-mode-area fiber lasers via gain filtering”. In: *Optics Letters* **35**:11 (2010), p. 1828.

[76] F. Di Teodoro et al. “Diffraction-limited, 300-kW peak-power pulses from a coiled multimode fiber amplifier.” In: *Optics letters* **27**:7 (2002), pp. 518–520.

[77] R. Di Leonardo and S. Bianchi. “Hologram transmission through multi-mode optical fibers”. In: *Optics Express* **19**:1 (2011), p. 247.

[78] S. Bianchi and R. Di Leonardo. “A multi-mode fiber probe for holographic micromanipulation and microscopy”. In: *Lab Chip* **12**:3 (2012), pp. 635–639.

[79] I. N. Papadopoulos et al. “Focusing and scanning light through a multimode optical fiber using digital phase conjugation”. In: *Optics Express* **20**:10 (2012), pp. 10583–10590.

[80] J. M. Beckers. “Adaptive Optics for Astronomy: Principles, Performance, and Applications”. In: *Annual Review of Astronomy and Astrophysics* **31**:1 (1993), pp. 13–62.

[81] H. Ma et al. “Adaptive conversion of multimode beam to near-diffraction-limited flattop beam based on dual-phase-only liquid-crystal spatial light modulators”. In: *Optics Express* **18**:26 (2010), p. 27723.

[82] R. K. Tyson. *Principles of Adaptive Optics*. Vol. 1. 2010, p. 345.

[83] J. M. Senior and M. Y. Jamro. *Optical fiber communications : principles and practice*. Pearson, 2009.

[84] *ISO 11146:2005 - Lasers and laser-related equipment – Test methods for laser beam widths, divergence angles and beam propagation ratios*. (Visited on 05/19/2017).

[85] D. W. Hahn. “Raman scattering theory”. In: *Department of Mechanical and Aerospace Engineering, University of Florida* (2007).

[86] Max Born and Kun Huang. *Dynamical theory of crystal lattices*. Clarendon press, 1954.

[87] Chen-Show Wang. “Theory of stimulated Raman scattering”. In: *Physical Review* **182**:2 (1969), p. 482.

[88] S. Keren et al. “Noninvasive molecular imaging of small living subjects using Raman spectroscopy.” In: *Proceedings of the National Academy of Sciences of the United States of America* **105**:15 (2008), pp. 5844–9.

[89] R. Salzer and H. W. Siesler. *Infrared and Raman spectroscopic imaging*. John Wiley & Sons, 2009.

[90] J. Cheng and X. S. Xie. *Coherent Raman scattering microscopy*, p. 590.

[91] R. R. Alfano, C. H. Liu, and W. S. Glassman. *Method for determining if a tissue is a malignant tumor tissue, a benign tumor tissue, or a normal or benign tissue using Raman spectroscopy*. 1993.

[92] A. Mahadevan-Jansen and R. R. Richards-Kortum. “Raman spectroscopy for the detection of cancers and precancers”. In: *Journal of Biomedical Optics* **1**:1 (1996), pp. 31–70.

[93] L. G. Cancado et al. “Quantifying Defects in Graphene via Raman Spectroscopy at Different Excitation Energies”. In: *Nano Letters* **11**:8 (2011), pp. 3190–3196.

[94] K. Kong et al. “Raman spectroscopy for medical diagnostics — From in-vitro biofluid assays to in-vivo cancer detection”. In: *Advanced Drug Delivery Reviews* **89**: (2015), pp. 121–134.

[95] P. S. Yarmolenko et al. “Thresholds for thermal damage to normal tissues: an update”. In: *International Journal of Hyperthermia* **27**:4 (2011), pp. 320–343.

[96] M. W. Dewhirst et al. “Basic principles of thermal dosimetry and thermal thresholds for tissue damage from hyperthermia.” In: *International journal of hyperthermia : the official journal of European Society for Hyperthermic Oncology, North American Hyperthermia Group* **19**:3 (2003), pp. 267–94.

[97] L. O. Svaasand, T. Boerslid, and M. Oeveraasen. “Thermal and optical properties of living tissue: application to laser-induced hyperthermia.” In: *Lasers in surgery and medicine* **5**:6 (1985), pp. 589–602.

[98] A. Ghita, P.I Matousek, and N. Stone. “Exploring the effect of laser excitation wavelength on signal recovery with deep tissue transmission Raman spectroscopy”. In: *The Analyst* **141**:20 (2016), pp. 5738–5746.

[99] H. S. Carslaw and J. C. Jaeger. *Conduction of heat in solids*. Clarendon Press, 1959, p. 510.

[100] J. V. Thompson et al. “Wavefront shaping enhanced Raman scattering in a turbid medium”. In: *Optics Letters* **41**:8 (2016), p. 1769.

[101] M. Mucalo. Elsevier.

[102] I. Starshynov et al. “Non-Gaussian Correlations between Reflected and Transmitted Intensity Patterns Emerging from Opaque Disordered Media”. In: *Phys. Rev. X* **8**: (2 2018), p. 021041.

[103] Nikos Fayard. “Joint-statistics between refl ected and transmitted speckle patterns: from mesoscopic correlations to information theory”. PhD thesis. ESPCI Paris, Institute Langevin, 2017.

[104] E. Akkermans and G. Montambeaux. *Mesoscopic physics of electrons and photons*. Cambridge University Press, 2007.

[105] B. Shapiro. “Large Intensity Fluctuations for Wave Propagation in Random Media”. In: *Phys. Rev. Lett.* **57**: (1986), p. 2168.

[106] R. Berkovits and S. Feng. “Correlations in coherent multiple scattering”. In: *Phys. Rep.* **238**:3 (1994), pp. 135 –172.

[107] N. Fayard et al. “Intensity correlations between reflected and transmitted speckle patterns”. In: *Phys. Rev. A* **92**: (2015), p. 033827.

[108] N. Fayard et al. “Mutual Information between Reflected and Transmitted Speckle Images”. In: *Physical Review Letters* **120**:7 (2018), p. 073901.

[109] D. B. Rogozkin and M. Y. Cherkasov. In: *Phys. Rev. B* **51**: (1995), p. 12256.

[110] L.S. Froufe-Pérez et al. “Fluctuations and correlations in wave transport through complex media”. In: *Physica A* **386**:2 (2007), pp. 625 –632.

[111] J. F. de Boer, M. P. van Albada, and A. Lagendijk. “Transmission and intensity correlations in wave propagation through random media”. In: *Phys. Rev. B* **45**: (2 1992), pp. 658–666.

[112] A. Z. Genack, N. Garcia, and W. Polkosnik. “Long-range intensity correlation in random media”. In: *Phys. Rev. Lett.* **65**: (17 1990), pp. 2129–2132.

[113] F. Scheffold and G. Maret. “Universal Conductance Fluctuations of Light”. In: *Phys. Rev. Lett.* **81**: (26 1998), pp. 5800–5803.

[114] S. Feng et al. “Correlations and Fluctuations of Coherent Wave Transmission through Disordered Media”. In: *Phys. Rev. Lett.* **61**:7 (1988), pp. 834–837.

[115] A. A. Chabanov et al. “Mesoscopic Correlation with Polarization Rotation of Electromagnetic Waves”. In: *Physical Review Letters* **92**:17 (2004), p. 173901.

[116] A. Bharucha-Reid. *Probabilistic methods in applied mathematics. Vol. 1*. New York London: Academic Press, 1968.

[117] B. Shapiro. “New Type of Intensity Correlation in Random Media”. In: *Phys. Rev. Lett.* **83**: (1999), pp. 4733–4735.

[118] P. Sebbah, R. Pnini, and A. Z. Genack. “Field and intensity correlation in random media”. In: *Phys. Rev. E* **62**: (2000), pp. 7348–7352.

[119] T. Strudley et al. “Mesoscopic light transport by very strong collective multiple scattering in nanowire mats”. In: *Nature Photon.* **7**: (2013), p. 413.

[120] W. K. Hildebrand et al. “Observation of Infinite-Range Intensity Correlations above, at, and below the Mobility Edges of the 3D Anderson Localization Transition”. In: *Phys. Rev. Lett.* **112**: (7 2014), p. 073902.

[121] K. Vynck, R. Pierrat, and R. Carminati. “Polarization and spatial coherence of electromagnetic waves in uncorrelated disordered media”. In: *Physics Review A* **89**: (2014), p. 013842.

[122] M. Lax. “Multiple Scattering of Waves. II. The Effective Field in Dense Systems”. In: *Phys. Rev.* **85**: (1952), p. 621.

[123] J.J. Sáenz, L.S. Froufe-Pérez, and A. García-Martín. “Intensity Correlations and Fluctuations of Waves Transmitted through Random Media”. In: *Wave Scattering in Complex Media: From Theory to Applications* **107**: (2003), p. 175.

[124] C. W. Hsu et al. “Correlation-enhanced control of wave focusing in disordered media”. In: *Nature Phys.* **13**: (2017), p. 497.

[125] O. S. Ojambati et al. “Controlling the intensity of light in large areas at the interfaces of a scattering medium”. In: *Phys. Rev. A* **94**: (4 2016), p. 043834.

[126] V. Ntziachristos. “Going deeper than microscopy: the optical imaging frontier in biology”. In: *Nat. Methods* **7**: (2010), p. 603.

[127] R. Y. Tsien. “Building and breeding molecules to spy on cells and tumors”. In: *FEBS Letters*. Vol. 579. 4 SPEC. ISS. 2005, pp. 927–932.

[128] Pittman et al. “Optical imaging by means of two-photon quantum entanglement.” In: *Physical review. A, Atomic, molecular, and optical physics* **52**:5 (1995), R3429–R3432.

[129] R. S. Bennink, Sean J. Bentley, and Robert W. Boyd. ““Two-Photon” Coincidence Imaging with a Classical Source”. In: *Physical Review Letters* **89**:11 (2002), p. 113601.

[130] A. Gatti et al. “Ghost Imaging with Thermal Light: Comparing Entanglement and Classical Correlation”. In: *Physical Review Letters* **93**:9 (2004), p. 093602.

[131] F. Ferri et al. “High-Resolution Ghost Image and Ghost Diffraction Experiments with Thermal Light”. In: *Physical Review Letters* **94**:18 (2005), p. 183602.

[132] B. I. Erkmen and Jeffrey H. Shapiro. “Ghost imaging: from quantum to classical to computational”. In: *Advances in Optics and Photonics* **2**:4 (2010), p. 405.

[133] M. J. Padgett and R. W. Boyd. “An introduction to ghost imaging: quantum and classical”. In: *Philosophical Transactions of the Royal Society A: Mathematical, Physical and Engineering Sciences* **375**:2099 (2017), p. 20160233.

[134] Y. Bromberg, O. Katz, and Y. Silberberg. “Ghost imaging with a single detector”. In: *Physical Review A* **79**:5 (2009), p. 53840.

[135] W. Gong and S. Han. “Correlated imaging in scattering media”. In: *Optics Letters* **36**:3 (2011), p. 394.

[136] J. H. Shapiro. “Computational ghost imaging”. In: *Physical Review A* **78**:6 (2008), p. 061802.

[137] M. Bina et al. “Backscattering differential ghost imaging in turbid media”. In: *Physical Review Letters* **110**:8 (2013).

[138] N. D. Hardy and J. H. Shapiro. “Reflective ghost imaging through turbulence”. In: *Physical Review A - Atomic, Molecular, and Optical Physics* **84**:6 (2011).

Acknowledgements

In this last part of this thesis I would like to acknowledge to all the people who made it possible.

First I would like to thank my supervisors, Jacopo Bertolotti and Bill Barnes for their guidance, discussions and all the support and advices during this time, that allowed me not only to grow as independent researcher, but also extra-professionally. Bill, I would like to thank you for all the useful and enjoyable discussions, your patience and ability to show me the big picture of things, where in the multiple discussions we have had I just started to discuss the problems I faced... It was great to see how you showed me the solutions by just leading me to see the big picture. It has been a pleasure to have the opportunity to work and hold discussions with you!

Jacopo, probably nothing I can say here will be enough to properly thank you for all the support, advices and all I have learned from you. I would like to thank you for all your support and encouragement during the hard and frustrating beginnings of the setting up of the experiments. Thank you as well for being a model of "never give up", it has been of great help when going through periods of doubt and frustration. Finally, to keep it short, I would like to thank you for all the scientific discussions we have had, your patience and being always ready to hold a discussion or offer help. It has been a pleasure to work with you, learning so much in this time.

Another person I would also like to thank is my colleague Ilya Starshynov with whom I worked for the experiments on speckle correlations. I want to thank you for all the extra work you did to make these experiments work and all you have helped me in different areas, from understanding technical things to build the cage for the optical table!. It has been really fun and amazing to work with you!

I also want to acknowledge Tom Vettenburg for all his help with the Raman experiment, all the useful scientific discussions and his readiness to help at any time.

I also thank our collaborators at ESPCI in Paris, Remi Carminati and his group for all the theoretical discussions regarding the correlations experiment. Acknowledge also our collaborators in the biophysics group in the University of Exeter, Adrian Ghita and Nick Stone, for their help, patience and support to finally make the project work.

I acknowledge financial support from the Engineering and Physical Sciences Research Council (EPSRC) of the United Kingdom, via the EPSRC Centre for Doctoral Training in Metamaterials (Grant No. EP/L015331/1) being of great support during the PhD, creating new opportunities and allowing for the development of a whole bunch of useful soft skills.

I would also like to thank the optics group in the University of Salamanca, Isabel Arias and Ana Garcia who inspired me from the very beginning and motivated me to pursue this fulfilling career in optics, and of course Julio San Roman and Iñigo Sola, who not only pushed me forward into loving optics, but also introduced me into the research world and the beauty of it.

And of course all of these professional features could not be fully enjoyed without friends and family around you, so here I would like to thank some of these people that stayed with me in hard times making them feel good.

I would like to thank Sathya, Nithya, Peter, Kimberly, Rayko, Pramod and of course the Spanish people, Erick and Gloria, Henry and Coni, Santi, Janire, Joaquin, David,... amazing and crazy people capable of making you laugh and enjoy the moment at any time, making you even forget you are in the rainy UK!

Of course here there should be a space for my family, I would like to thank my parents and my brother for their unconditional support, capable of transmitting all the love and understanding even thousands of miles away.

And last and most importantly, I thank my partner Sergio. No words to really express how thankful I am for his infinite understanding, patience, love and support. Going by my side through everything all these years, making the hardest times enjoyable and the good ones, unforgettable.

Thank you all!